Computational Fluid Dynamics Modelling of Blood Flow in Venous Stents and Endovascular Neural Interfaces

Weijie Qi

ORCID: 0000-0002-0686-4948

Submitted in total fulfilment for the degree of

Doctor of Philosophy

August 2024

Faculty of Engineering and Information Technology

Department of Biomedical Engineering

The University of Melbourne

Declaration

In accordance with the Doctor of Philosophy and Research Master's regulations at the University of Melbourne, I declare that the thesis comprises only my original work towards the Doctor of Philosophy, except as acknowledged in the preface. Acknowledgement and reference have been made in the text regarding all other material used. I declare that the thesis is fewer than the maximum word limit in length, exclusive of tables, maps, bibliographies, and appendices.

Abstract

The endovascular neural interface (stent-electrode array) leverages commercial venous stents, traditionally used to treat blood vessel diseases, to address neurological disorders. By integrating electrodes onto the stent struts, this endovascular neural interface can be delivered through the healthy jugular vein. More importantly, the device is capable of recording brain signals, offering a novel and minimally invasive method to interface with the human brain. Despite the growing interest in this technology for research and commercialization, there is limited knowledge about its impact on vascular health. Specifically, it is crucial to understand how this new type of stent interacts with human veins and the potential complications, such as neointimal hyperplasia.

Neointimal hyperplasia, characterized by excessive tissue growth, can impact stenting outcomes by narrowing the blood vessel lumen and restricting blood flow, thereby increasing the risk of stroke. Evidence from arterial stents, which are more extensively studied, indicates that the presence of stent struts disturbs arterial flow and tissue growth. However, the tissue response following the implantation of an endovascular neural interface appears more complex and non-uniform, suggesting a different mechanism compared to arterial narrowing in diseased arteries.

To comprehend the impact of the device on blood flow and explain tissue growth patterns in healthy veins after placing the stent-electrode array, the thesis aims to **1) visualize blood flow in the stented blood vessel to assess the device impact on blood flow, 2) determine critical factors affecting blood flow for stent design optimization, and 3) elucidate in-vivo tissue growth patterns in conjunction with blood flow patterns**. To study blood flow and novel stent designs, Computational Fluid Dynamics (CFD) modelling was used to simulate blood flow in idealized and anatomically accurate stents and blood vessels. Animal experiments were conducted to validate the computational method and elucidate the tissue growth patterns in venous stents.

Computational models have been developed throughout this PhD thesis, incrementally incorporating various features of stented blood vessels to refine the model and understand their blood flow impact. Different experimental methods, such as Doppler Ultrasound and contrast enhanced X-ray (venography), were used to validate the computational model, revealing a negative power-law correlation between blood flow and tissue growth. It was observed that the impact of device placement on blood flow, indicated by low Wall Shear Stress patterns, was due to the shape of the blood vessels deformed by the stent strut and the presence of the stent struts. In addition, the thesis reported that the complex geometry and material properties of veins, distinct from coronary and carotid arteries, have made veins more susceptible to stent expansion and flow alterations. The differences between veins and arteries, particularly in blood flow conditions, material properties, and shape, have rendered blood vessels more sensitive to changes in blood flow and wall shear stress. The model developed in this thesis fills the literature gap in venous stents and serves as a reliable research tool for testing and evaluating new stent designs. The work presented in this thesis provides researchers and engineers with critical insights into the blood flow through endovascular neural interfaces, which lays a foundation for the development of future venous implants.

Preface

In preparing this thesis, I affirm the following: (1) The work presented is solely my own original contribution, without collaboration with others. (2) None of the material in this thesis has been submitted for any other qualifications. (3) All work included in this thesis was conducted after my enrolment in the degree program. (4) No third-party editorial assistance was utilized in preparing this thesis. (5) The contributions of all individuals involved in any multi-authored publications or articles included in this thesis are duly acknowledged.

The publication status of all chapters presented in article format using the descriptors below:

- **Chapter 1 and 2** have not been submitted for publication.
- **Chapter 3.1.2** has been published on 2023/7/24:
    - Qi, W., Ooi, A., Grayden, D., & John, S. (2023). Computational fluid dynamics of stent-mounted neural interfaces in an idealized cerebral venous sinus. *Proceedings of the Annual International Conference of the IEEE Engineering in Medicine and Biology Society, 2023*, 1-4. https://doi.org/10.1109/EMBC40787.2023.10341099
- **Chapter 4** has been published:
    - **Chapter 4.2-4.5** have been published on 2023/7/24:
        - Qi, W., Ooi, A., Grayden, D., & John, S. (2023). Computational fluid dynamics of stent-mounted neural interfaces in an idealized cerebral venous sinus. *Proceedings of the Annual International Conference of the IEEE Engineering in Medicine and Biology Society, 2023*, 1-4. https://doi.org/10.1109/EMBC40787.2023.10341099
    - **Chapter 4.6-4.8** were the original work where the computational works contributed to section 3.4 and 4.4 of a journal paper published by *Journal of Neural Engineering* on 2022/10/28. The remaining sections were not incorporated into this thesis. The author undertook the majority of the work in those two sections of the paper:
        - John, S. E., Donegan, S., Scordas, T. C., Qi, W., Sharma, P., Liyanage, K., Wilson, S., Birchall, I., Ooi, A., Oxley, T. J., May, C. N., Grayden, D. B., & Opie, N. L. (2022). Vascular remodeling in sheep implanted with endovascular neural interface. *Journal of neural engineering*, *19*(5), 10.1088/1741-2552/ac9a77.
- **Chapter 5** has been published by *Scientific Reports* on 2024/3/27:
    - Qi, W., Ooi, A., Grayden, D. B., Opie, N. L., & John, S. E. (2024). Haemodynamics of stent-mounted neural interfaces in tapered and deformed blood vessels. *Scientific reports*, *14*(1), 7212. https://doi.org/10.1038/s41598-024-57460-w
- **Chapter 6 and 7** have not been submitted for publication.

The candidate is funded by China Scholarship Council - University of Melbourne PhD Scholarship provided by both the University of Melbourne and China Scholarship Council (CSC) from the Ministry of Education of P.R. China, CSC NO. 202008240002. The research was supported by research grants from the USA Department of Defence Office of the Congressionally Directed Medical Research Programs (CDMRP), EP170058 and National Health and Medical Research Council of Australia (NHMRC) Grant 1158912. The CFD modelling was supported by The University of Melbourne Research Computing Services and the Petascale Campus Initiative.

Acknowledgements

I would like to express my sincere gratitude to my supervisors, Prof. Sam John, Prof. David Grayden, and Prof. Andrew Ooi. Their wisdom and guidance are invaluable to my PhD journey. They have taught me critical thinking and effective communication. Special thanks to Sam for teaching me how to perform sophisticated surgical procedures, which was a fantastic experience. The PhD journey has been a pivotal and memorable stage of my life, and I am grateful for their presence.

I am thankful to my colleagues and friends, especially to Jingyang Liu, Huakun Xin, Tim Mahoney, Joel Villalobos, Luka de Groot, Frank Weissenborn, Tom Vale, Anthony Dornum, Quan Nguyen, and Ruslan Pustovit for assisting with the experiments, which is a cornerstone chapter of my thesis.

Finally, I would like to thank my family for their encouragement and great support. My parents have provided a nurturing and stress-free environment which enabled me to focus on my research.

I would like to extend a special thanks to my partner, Yiqing Shen, for always staying by my side. Her company was the oasis during challenging times. Her presence motivated me and has been the source of my diligence.

Contents

List of tables, figures & illustrations

List of Abbreviations

Abbreviation	Definition
2D	Two dimensional
3D	Three dimensional
BCI	Brain machine interface
CAD	Computer-aided design
CFD	Computational fluid dynamics
CT	Computer tomography
CVS	Cerebral venous sinus
DBS	Deep brain stimulation
DVT	Deep vein thrombosis
ECoG	Electrocorticography
ECM	Extracellular matrix
EEG	Electroencephalogram
ENI	Endovascular neural interface
FEA	Finite element analysis
FEM	Finite element method
MRI	Magnetic resonance imaging
N-S	Navier-Stokes equation
OSI	Oscillatory shear index
PC-MRI	Phase-contrast magnetic resonance imaging
PIV	Particle imaging velocimetry
RRT	Relative residence time
SS	Sigmoid sinus
SSS	Superior sagittal sinus
TAWSS	Time-averaged wall shear stress
TS	Transverse sinus
WSS	Wall shear stress
WSSG	Wall shear stress gradient

Chapter 1 – Introduction

Epilepsy affects more than 50 million people globally (Chen, Brodie, Ding, & Kwan, 2023). Among them, at least 30% of patients have drug-resistant epilepsy (Mohammadzadeh & Nazarbaghi, 2022) and may require the placement of electrodes, which deliver electrical impulses to suppress abnormal brain signal that causes seizure. However, placing electrode in the brain poses risks of infection and internal bleeding in the brain, which limits treatment efficacy. The endovascular stent-electrode array, which delivers electrode without opening the skull or damaging the brain tissue, has emerged as a minimally invasive alternative to detect and stop an epileptic seizure.

The stent-electrode array is a smart endovascular mesh-like expandable device. Unlike commercially available stents, the device is mounted by disc electrodes, which allow brain signal recording and brain stimulation from a healthy blood vessel adjacent to the target brain region. During implantation, the device is delivered to the brain via a catheter from a small surgical incision in the jugular vein. Subsequently, the catheter and the device manoeuvres along the cerebral venous blood vessels until it is close to the brain region of interest without damaging the brain tissue (Oxley et al., 2016). Owing to the endovascular approach of implantation, the stent-electrode array offers much lower risk compared to the conventional cortical electrode implantation, which requires open-brain surgery and direct contact with the brain tissue. Therefore, the stent-electrode technology has paved a promising way to treat neurological disorders, including epilepsy. In addition, the technology has enabled interfacing with the human brain for controlling assistive device, such as the Stentrode^{TM} device that has helped paralysed patients to send emails with imagination (Oxley et al., 2021). With emerging research on repurposing stents for brain recording and stimulation, a deeper understanding of device complications, especially neointimal hyperplasia, becomes paramount for the development of this novel technology.

Neointimal hyperplasia is characterized by an excessive tissue growth around the stent after implanted in the blood vessels, which can cause severe narrowing (greater than 50% reduction in diameter) of the blood vessel lumen with a prevalence between 5% and 10% in stented arteries (Collins et al., 2012). While clinical data is limited for venous stents, venous tissue growth patterns post-stenting have been reported to be non-uniform and inexplicable (John et al., 2022; Opie et al., 2017). The increasing application of stent in the cerebral venous sinuses has necessitated the demand for deciphering such complex venous neointimal growth patterns.

Insights from arterial stents suggest that haemodynamics (i.e. blood flow) has a profound influence on vascular tissue remodelling post-stenting. For instance, stent deployment will expand and alter the shape of the blood vessels. The blood vessel wall deformation and the presence of stent strut in the bloodstream will disrupt normal blood flow and the force exerted by the flowing blood on the inner lining of the blood vessel. The force per unit area exerted on the endothelial linings is referred to as the Wall Shear Stress (WSS). A WSS lower than 0.5 Pa promotes endothelial growth, which can elevate the risks of neointimal overgrowth (Gijsen et al., 2019). Therefore, examining the blood flow and WSS post-stenting are crucial for venous stents.

To visualize blood flow and WSS, Computational Fluid Dynamics (CFD) has been extensively used for research in arterial stents. Studies have revealed that tissue overgrowth, which is usually in the form of focal narrowing, is regulated by the WSS patterns post-stenting (He et al., 2020). However, venous neointimal hyperplasia remains unexplored due to a lack of clinical data. There have been only

reports of non-uniform tissue growth patterns but no clue about the underlying mechanism (Opie et al., 2017). Furthermore, knowledge from the current literature is insufficient to understand venous hyperplasia. The venous environment, characterized by a more compliant venous blood vessel wall and a less pulsatile flow, is distinctive from arteries. There has been no literature that considers those factors. Therefore, to better understand tissue growth in healthy venous stents for future development of stent-electrode device, and to fill the research gap in venous haemodynamics and venous neointimal growth, this PhD thesis will study the haemodynamics of venous stents in cerebral venous sinuses and investigate the correlation between the hemodynamic metric – WSS, and venous tissue growth patterns.

Chapter 2 – Literature review

2.1 Stent-mounted neural interface

2.1.1 Application of neural interface and endovascular neural interface

Neural prostheses are medical devices that restore lost motor or sensory functions that have been lost due to injury or disease. They have enhanced quality of life for many people worldwide (Prochazka, Mushahwar, & McCreery, 2001). Most prostheses are devices that perform electrical signal recording from the nerves of interest through electrodes. One example of neural signal recording is the brain-computer interface (BCI). The BCI collects signals from the neural structures in the brain and converts them to commands for controlling external devices, such as a computer or a wheelchair (Shih, Krusienski, & Wolpaw, 2012).

BCIs can be classified as non-invasive or invasive. The non-invasive BCI uses surface electrodes to record an electroencephalogram (EEG). EEG electrodes are placed on the scalp to measure the electric fields generated by activities of the brain. Although surface electrodes are non-invasive and safe, they suffer from poor spatial resolution due to the high impedance of the skull. The bone material attenuates signal transmission from the brain tissue to the electrodes (Yang, Gong, & Li, 2021). Implantable electrodes provide better resolution and signal quality for brain monitoring but are more invasive. Implantable electrodes are widely used in electrocorticography (ECoG) and deep brain stimulation (DBS). DBS is a neuro-surgical procedure that involves the placement of electrodes to stimulate specific targets in the brain. For deep brain stimulation, electrode arrays are implanted by drilling a hole on the skull to access the brain. It also requires penetration through the brain tissue to access the deep brain regions such as the thalamus (Fluri, Bieber, Volkmann, & Kleinschnitz, 2015). Similarly, subdural grid electrodes also require craniotomy to access the surface of the brain for seizure detection. During ECoG recording and DBS, a portion of the skull needs to be removed by craniotomy to implant the electrode onto the surface of the cerebral cortex. The procedure increases the risks of brain tissue injury and surgical complications, including inflammation and infection (Kozai, Jaquins-Gerstl, Vazquez, Michael, & Cui, 2015).

The endovascular electrode array provides hope to mitigate the complications associated with open brain surgery. The endovascular electrode array is an emerging technology that builds upon existing commercially available intracranial stents. It comprises a stent-like metallic mesh body with electrodes mounted on it (Figure 2.1). By mounting electrodes on intracranial stent struts, brain signal recording and brain stimulation become feasible without craniotomy. One great merit of stent-electrode technology is its minimal invasiveness compared to conventional brain electrode arrays. However, for a stent-based electrode array, it is delivered percutaneously (Oxley et al., 2016). An incision is made in the neck to access the arterial or venous blood vessels that either supply or drain the brain, respectively. With the help of a guide catheter, the stent can access different regions of the brain by implanting it on certain blood vessels. In this way, the electrode array is implanted near the brain tissue without open-brain surgery.

One successful example is the Stentrode™ (Oxley et al., 2020). A clinical trial of the Stentrode™ has obtained intracranial EEG in patients with motor neuron disease in Australia (Kozai, Jaquins-Gerstl, Vazquez, Michael, & Cui, 2015). In this study, patients were implanted with the Stentrode™ in their superior sagittal sinus. The device decodes brain signals of patients and acts as a brain-machine

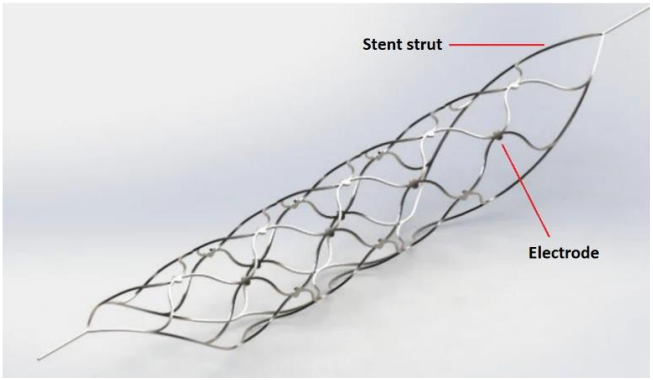

Figure 2.1 The device of the Stentrode^{TM} taken from the Neuroscience News (Oxley et al., 2020)

interface, helping them control a computer. The study has demonstrated the feasibility of brain signal recording to increase volitional control for disabled patients.

Electrical stimulation of the brain is also achievable using a stent-electrode device. In an experiment conducted by Opie et al. (Opie et al., 2018), the stent could stimulate the motor cortex of sheep and generate facial responses and limb movements. The device has the potential to treat neurological disorders, including epilepsy and Parkinson's disease.

2.1.2 Safety of Endovascular neural interface

Due to a lack of long-term clinical data, the question on how the device influences the intracranial blood vessels remain unanswered. In Opie et al. (2017), neointimal growth was observed on the device for 190 days inside the blood vessel, leading to a small reduction of the blood vessel lumen due to local blood vessel wall thickening in sheep models (Figure 2.2). The tissue growth and its associated impact on the cerebral venous system are important for the device and need further investigation to better understand the impact of the endovascular stent-electrode device on the blood vessel. To date, stent-electrode technology is still undergoing clinical trials to prove its long-term efficacy and safety (John, Grayden, & Yanagisawa, 2019). Short-term clinical data on human participants has reported stent patency without any adverse events (Oxley et al., 2020). Further

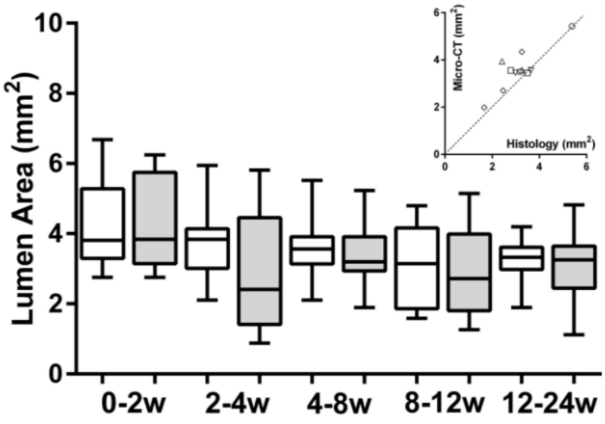

Figure 2.2 The histological study from Opie et al. (2017) has shown that the lumen area decreased by a small amount after 24 weeks of implantation.

study of the interactions between the stent and blood vessels will provide detail about the safety of stent-electrode device.

Undesired responses to stent implantation occur in traditional stent devices. For example, stent-induced stenosis, the narrowing of the blood vessel, is prevalent in arterial stents and is present in around 10% of percutaneous coronary stenting cases (Shlofmitz, Iantorno, & Waksman, 2019). Stenosis is influential to blood flow when the lumen is reduced by more than 50% (degree of stenosis > 50%). Thrombosis, the formation of a blood clot, is a less common complication (1-3%) but leads to severe outcomes, including blood vessel infarction and strokes with high mortality rates (Kolandaivelu et al., 2011). Stenosis and thrombosis with stenting are caused by adverse interactions between the stent struts and the blood vessel wall, which have been studied for decades and will be discussed in the following section. Given that cerebral venous stenting is relatively new compared to arterial stenting, a research gap exists in venous sinus stenting and cerebral vascular responses. Therefore, it becomes crucial to investigate the causes of vascular responses such as stenosis, which will generate critical insights into the long-term safety of intracranial stenting.

Overall, the implantation of endovascular electrodes in the cerebral venous sinus has enabled a potential approach for cortical signal recordings. For this method to be further developed into a reliable platform for research in neurological disorders, it is critical to understand the effect of stenting on the veins around the brain.

2.1.3 Common sites of implantation for neural interface

Endovascular recording has been developed since 1972 when Penn, Hilal, Michelsen, Goldensohn, & Driller (1973) placed EEG electrodes in the carotid artery of baboons to record their brain signals. Other blood vessels, such as the middle and anterior cerebral arteries, have also been implanted to detect seizures in epilepsy patients (Stoeter, Dieterle, Meyer, & Prey, 1995). They have shown that the endovascular recordings obtained a higher amplitude than the extracranial EEG recordings. However, endovascular recording in arteries was limited by the complex geometry of the cerebral artery (Fan, Lopez-Rivera, & Sheth, 2020). Artefacts due to misplacement of electrodes could result in a different signal, making the original brain signal unpredictable.

Intra-venous EEG has allowed electrical recordings for a longer time than recordings in arteries. Kunieda et al. (Kunieda et al., 2000) used cavernous sinus and superior petrosal sinus, the dural venous sinuses beneath the brain, to record EEG signals from patients with epilepsy. The recording could be performed for up to 75 hours. However, brain signals could be significantly disturbed by the motion artefact of the patient.

Another way to evaluate human brain activity is to record signals from the surface of the brain tissue. Bower et al. (2013) used a venous catheter device with micro-electrodes to record cortical activities. The endovascular electrodes could detect epileptic responses to antibiotics in pigs, with similar waveforms compared to ECoG measurement using the subdural electrodes. Thus, endovascular recordings from the SSS have created the potential for seizure prediction. This research will focus on endovascular stent that is implanted inside the SSS.

The Stentrode™ is usually implanted into the Superior Sagittal Sinus (SSS), a cerebral venous sinus that resides in the middle groove between the left and right cerebral hemispheres (Figure 2.3) (Bernard, Newell, & Tubbs, 2020). In humans, the SSS has a triangular cross-section, with its apex

pointing inferiorly (Bernard, Newell, & Tubbs, 2020). The average diameter of a human SSS is around 7 to 9 mm, and the blood vessel tapers anteriorly (Larson, Lanzino, & Brinjikji, 2020). The anterior part of the SSS originates from the foramen cecum of the frontal bone, receiving blood from the emissary veins from the nasal cavity (Egemen & Solaroglu, 2017). The SSS then runs along the groove and spans the cerebral cortices, draining the cerebral hemispheres from cortical veins (Egemen & Solaroglu, 2017). The posterior part of the SSS curves to the back of the head and empties into the confluence of sinuses in the occipital region, where the blood vessel branches to left and right transverse sinuses (Egemen & Solaroglu, 2017). Subsequently, the venous blood flows through the sigmoid sinus and internal jugular veins, leaving the head and sent to the right atrium of the heart (Figure 2.3).

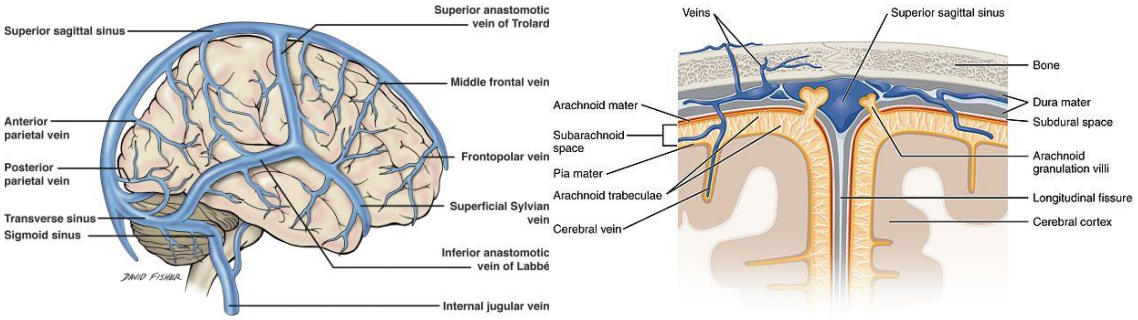

Figure 2.3 The anatomy of the human superior sagittal sinus in sagittal view (left) and in coronal view (right), taken from Anatomy, Imaging and Surgery of the Intracranial Dural Venous Sinuses (Bernard, Newell, & Tubbs, 2020).

On either side of the SSS are lateral venous lacunae, which drains the meningeal and diploic veins. The SSS and venous lacunae reside in the dura mater, a protective layer of connective tissue (Figure 2.3 right) surrounding the brain and spinal cord. Within the blood vessel are the arachnoid granulations, which are protrusions of the arachnoid membrane that enable the drainage of cerebrospinal fluid from the subarachnoid space to the venous sinuses.

The SSS was selected to be implanted by the Stentrode^{TM} due to its close distance to the motor cortex of the brain, which generates neural signals related to muscle activation intentions (Daggubati & Liu, 2019). The middle part of the SSS is near the sensorimotor cortex (Opie et al., 2018). The small gap between the SSS and the cortex allowed the endovascular electrodes to obtain high-fidelity neural signals (Oxley et al., 2016).

2.1.4 Literature in stenting the Superior Sagittal Sinus

Stent placement in the SSS commonly exists for treating Idiopathic intracranial hypertension (Daggubati & Liu, 2019), a disorder related to obesity but with unknown cause. Intracranial hypertension has a detrimental impact on cerebral tissue and its blood vessels. It causes an elevation of the intracranial pressure, which results in headaches and even vision impairment (Daggubati & Liu, 2019). Furthermore, the high intracranial pressure also acts upon the cerebral venous system, adding extra load to the blood vessel wall of the cerebral venous sinus (Entezami, Gooch, & Dalfino, 2019). Since venous walls have soft material properties, they are generally collapsible with increased extraluminal pressure. Under high intracranial pressure, the venous sinus becomes narrowed due

to external compression. The reduced venous drainage is likely to increase the intracranial pressure further, forming a vicious cycle and elevate the risk of stroke (Adderley et al., 2019).

Surgeons have used commercially available intracranial stents to treat the narrowing of the superior sagittal sinus and other affected cerebral venous sinuses in IHH patients, including the transverse sinus and sigmoid sinus (Adderley et al., 2019). In the literature, there are approximately 4 in 100,000 people that have intracranial hypertension (Larson, Lanzino, & Brinjikji, 2020), with stenosis developed in 94% of the IIH patient population (Egemen & Solaroglu, 2017). From retrospective studies, around 14% of the patients receiving a venous stent (395 patients across 24 studies) developed stent-adjacent stenosis (Saber, Lewis, Sadeghi, Rajah, & Narayanan, 2018), a condition where a new narrowing blood vessel region was observed in the vicinity of the stent implantation. The narrowing leads to a return of the high intracranial pressure and the recurrence of hypertension, which required additional stent placement to treat the restenosis (Kumpe et al., 2012). The potential cause of restenosis is hypothesized to be associated with hypertension, but it is still under research.

Currently, research in venous sinus stenting is based on the retrospective review of the patient data to assess the efficacy and long-term safety of venous sinus stents. The efficacy was assessed by the percentage of patients who experienced the relief of symptoms, which includes headache, papilledema, visual changes, and pulsatile tinnitus (Puffer, Mustafa, & Lanzino, 2012). In terms of safety, numerous studies have reviewed the complication rates of venous sinus stenting from long-term follow-up in their institutions. Shields L. et al. (2019) reviewed 42 patients with 1 patient experienced in-stent thrombosis. Saber H. et al. (2018) systematically reviewed 473 patients from 24 studies, with a stent survival rate of 84% and a stenosis rate of 14%. Thus, in the cerebral venous sinus, stenosis, and thrombosis could happen post-stenting for the treatment of intracranial hypertension.

The determinant of stent-adjacent stenosis has also been studied. Raper et al. (2017) suggested that the change in the venous pressure before and after stenting might be used to predict stent-adjacent stenosis. In their retrospective study, stenosis occurred in more than 20% of patients who experienced a rise in the venous pressure downstream to the stent post-stenting. The study was limited by the small size of the patient cohort, and the mechanism of pressure change was not examined. More research could be done to reveal factors that contribute to stent adjacent stenosis.

Currently, stent complications and failure have not been observed in Stentrode^{TM} implantation in the human superior sagittal sinus. Complications, especially restenosis, were reported for patients with hypertension and were hypothesized to result from intracranial hypertension. The hypothesis did not apply to stent implantation in people without hypertension, and thus could not provide insights into the safety of venous sinus stenting for endovascular recording. The effect of stenting on the cerebral venous sinus was still not well understood due to limited literature. This suggests a research gap in venous sinus stenting. To better understand the effect of stenting on the implanted blood vessel, stenting in the coronary artery was also review, which will be discussed later.

2.2 Stenting-related complications

Stenting-related complications have been reported for both arterial and venous stents. For instance, vascular tissue overgrowth and blood clot formation were usually observed after stent implantation, reducing the long-term stability of stents inside the human body (Shlofmitz, Iantorno, & Waksman,

2019). Among the various types of stents, coronary stenting is a well-developed field with a large body of literature. Studies in coronary stenting have revealed the prevalence of in-stent restenosis, with a rate of 16-44% after coronary stent implantation (Alraies, Darmoch, Tummala, & Waksman, 2017). The gradual re-narrowing of the stented coronary artery, where substance accumulates with tissues build up around the stent strut, causes blood vessel narrowing (Alraies, Darmoch, Tummala, & Waksman, 2017). Thrombosis is another devastating complication that is associated with stenting. It is more frequently observed in the venous stent and leads to blood vessel occlusion (Esmon, 2009). This chapter will introduce the two most common stent-related complications, namely stenosis and thrombosis, and how those diseases develop post-implantation. It will review the literature in both arterial and venous stents to reveal the underlying mechanisms of stenosis and thrombosis, as well as the hemodynamic factors that contribute to stenosis and thrombosis.

2.2.1 Arterial neointimal hyperplasia

Stenosis can occur in arteries and veins post-stenting. In arteries, stenosis post-stenting is called "in-stent restenosis". Restenosis narrows the artery after stent implantation for treatment of atherosclerosis. Atherosclerosis is a disease where a plaque, consisting of lipid, cholesterol, calcium, fibrin, and other substances found in the blood, builds up in the artery. An arterial balloon-expandable stent is usually deployed to the atherosclerotic lesion site to open and support the narrowed lumen. Restenosis usually develops after 6 to 12 months of implantation. The rate of restenosis is dependent on multiple factors. The rate appears to be higher when the patient has multiple stenosis. The rate is also higher for bare metal stents than drug-eluting stents, which has a coat of medication on its strut to prevent blood clotting. During restenosis, cells migrate and proliferate on the luminal surface of the stent (Alraies, Darmoch, Tummala, & Waksman, 2017). The tissue formation is called neointimal hyperplasia. It reduces the lumen diameter of the artery.

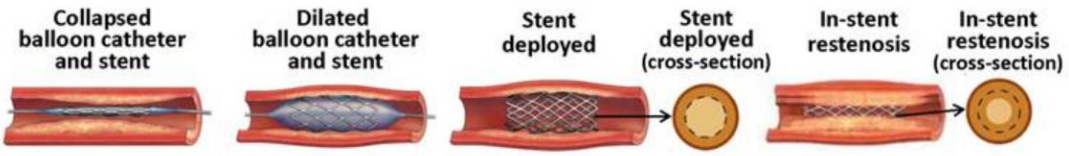

Figure 2.4 The formation of restenosis after balloon angioplasty, taken from Yin et al. (2014).

The development of stenosis is a complicated process. It involves several stages, including endothelium injury, inflammatory response, granulation tissue formation, and tissue remodelling (Chaabane, Otsuka, Virmani, & Bochaton-Piallat, 2013).

First, during stent implantation, the innermost layer of the blood vessel wall, called the endothelium (i.e. tunica intima), may be destroyed or partially damaged by the delivery and the expansion of the stent (Chaabane, Otsuka, Virmani, & Bochaton-Piallat, 2013). The denudation of the endothelial cells is covered by a thrombus after the injury. Anti-platelet drugs are always used to reduce thrombosis in the early stage of implantation. After several weeks, the endothelium will enter a repairing stage where the endothelial cells regrow and fully cover the damaged region and the stent surface. The repair is called reendothelialization, and it is also facilitated by other substances to accelerate healing of the artery, such as the bone-marrow-derived endothelial progenitor cells.

Meanwhile, endothelial injury and stent placement trigger a series of inflammatory responses at the injury site (Chaabane, Otsuka, Virmani, & Bochaton-Piallat, 2013). The stent is a foreign body to the blood vessel, which leads to platelet activation and platelet deposition at the lesion site. Leucocytes also play a role in tissue inflammation by interacting with the platelets. The interactions between leukocytes and platelets initiate and facilitate the progression of neointimal formation. Studies have demonstrated that inflammation was correlated with neointimal thickening in coronary arteries.

The middle layer (tunica media) of the artery contains smooth muscle cells, which contribute to the formation of granulation tissue and tissue remodelling around the implantation site (Chaabane, Otsuka, Virmani, & Bochaton-Piallat, 2013). Around the location of the injury, macrophages were observed around the stent strut, functioning by ingesting cell debris called phagocytosis and secreting growth factors. Platelets and endothelial cells are also involved in releasing growth factors and chemicals. Substances such as chemokines and cytokines promote the proliferation of smooth muscle cells. In addition, the presence of stent struts in the blood vessel also poses a mechanical stimulus to the endothelial wall, inducing cell migration (Chaabane, Otsuka, Virmani, & Bochaton-Piallat, 2013).

2.2.2 Venous neointimal hyperplasia

In veins, stenosis post-stenting is less common, with few cases reported across several blood vessels, including cerebral venous sinus (Kunieda et al., 2000) and veins in the lower limb (Saber, Lewis, Sadeghi, Rajah, & Narayanan, 2018). Stent restenosis could occur after stenting for deep vein thrombosis (DVT) from the lower limb. Target blood vessels typically include the iliac vein, the iliofemoral vein, and the iliocaval vein (Sharifi & Mehdipour, 2010). However, little is known about the pathology of venous stent stenosis. The literature presents little evidence on the long-term performance of venous stents, with only case studies of a small set of patients who underwent venous stenting, where only one in thirteen patients developed blood vessel occlusion (Matsuda et al., 2014).

In-stent restenosis in veins develops differently from arterial stenosis. In-stent restenosis in veins is rarely observed. There is little literature discussing the pathology and mechanism of restenosis in veins. One suggestion is that neointimal proliferation is less active in veins due to different anatomy from arteries. The venous media and adventitia are thinner, containing less smooth muscle cells responsible for tissue growth. Blood flow inside the veins is generally slow and less pressurized. The mild blood flow environment would pose less stimulus to the blood vessel wall than the flow in arteries (Buccheri, Piraino, Andolina, & Cortese, 2016).

Thrombosis has been found as the major complication causing blood vessel occlusion. In a study of 163 stent samples obtained at different times after stent implantation in humans, fresh and old thrombus were identified and found to have evolved into diffuse intimal thickening (Gordon, Williams, & Nicklas, 2021). Venous stent thrombosis is thus more related to coagulation, which will be discussed later.

2.2.3 Stent thrombosis

Stent thrombosis is the major complication associated with stent implantation (Modi, Soos, & Mahajan, 2021). Despite its low occurrence rate from 0.5-2%, thrombosis results in a high risk of myocardial infarction and death, which were reported as high as 45% in the literature (Kristensen & Grove, 2007). Thrombosis could be categorized into early (0-30 days), late (>30 days), and very late (>12 months) thrombosis, depending on the elapsed time after stent implantation. In addition, early thrombosis is the most prevalent type and can be further divided into acute (<24 hours) and subacute (1-30 days).

The behaviour and physiology of platelets are critical for stent thrombosis. Thrombosis, in general, is caused by tissue injury followed by platelet activation and aggregation (Watts, Chatterjee, & Leesar, 2018). The platelets and fibrous protein, called fibrin, join, and form a blood clot, which may grow sufficiently large to occlude the blood vessel. Thrombosis typically occurs instantly after an injury to the endothelium lining. When the endothelium is injured, the collagen and tissue factors beneath become exposed to the bloodstream. The exposed collagen induces the adhesion, accumulation, and activation of platelets around itself. The exposed tissue factor converts fibrinogen to fibrin and activates the platelets (Jerjes-Sánchez, 2015).

Commonly, thrombosis post-stenting is managed by introducing anti-platelet drugs, which reduce the aggregation of platelets to form a clot. This method modifies the property of the platelet and interferes with the physiological process of healing in the early stage. However, thrombosis could still happen in a very late stage due to stent placement (Lee & Hong, 2016).

Incomplete stent apposition may contribute to stent thrombosis (Holmes et al., 2010). The stent may be under-expanded during implantation, meaning that the stent struts are not well-apposed onto the blood vessel wall. Thus, the stent strut may not join the newly formed endothelium through re-endothelialisation. The stent strut exposed to the bloodstream may attract platelets on its surface and trigger platelet activation. Furthermore, stent mal-apposition is also associated with delayed healing of endothelium, which may cause prolonged inflammation and thrombus formation in the late stage (Casa, Deaton, & Ku, 2015). In addition, certain blood flow condition may also lead to thrombosis, which will be discussed later in 1.3.3.

Thrombosis in veins has a different mechanism. Unlike arterial thrombosis, which is accompanied by injury and shear-induced platelets aggregation, venous thrombosis is more often observed without any evidence of tissue injury. Autopsy studies have observed thrombosis in venous valves. It was possibly the result of flow stagnation and vortices of blood (Jerjes-Sánchez, 2015), unlike the high flow conditions in arteries. The flow stasis prevents the clearance of clotting factors from the sinus. This may promote the coagulation process and initiate thrombus formation (Esmon, 2009). Venous thrombosis exists in the lower limbs, which is called deep vein thrombosis. Especially in venous valves, the elastic flaps of tissue forming the valve had a pocket geometry, and blood flow around the pocket is slow. Small thrombi formed from blood coagulation can grow slowly in the valve pocket over weeks and extend along the venous wall, blocking the vein eventually (Mackman, 2012).

Venous stent thrombosis is prevalent. Re-occlusion of a venous stent occurs in 20-30% of patients with stents in their deep veins (Strijkers et al., 2015). Allowing adequate inflow and outflow for the venous stents would be critical to prevent the second occlusion to the vein. They believed that the impeded blood flow contributes to thrombus formation in the deep veins. Patients with distorted

venous anatomy suffered from stent under expansion, which reduces the diameter of the blood vessel and hence the flow. In addition, minor injuries to the endothelial layer of the venous blood vessel wall can increase the risk of blood clot formation. Minor injuries could be caused by vascular surgical procedures, such as catheter and stent delivery. However, the risk of blood clot formation is usually mitigated by administration of anticoagulants for up to 6 months (Hingorani et al., 2018).

2.3 Haemodynamics and stent complications

The change in blood flow plays a crucial role in the prognosis of stenosis and thrombosis in both stented arteries and veins. From the literature in coronary stenting, local blood flow has been well recognized to influence restenosis and thrombosis (Ng et al., 2017).

A stent may alter blood flow in several ways. First, stent implantation may change the geometry of blood vessels, which induces modification to blood flow pattern (LaDisa et al., 2005). Geometric features, such as curvature, tapering, and cross-section shape, could be altered by the stent implantation since the blood vessel is more compliant than metal material. Consequently, the blood vessel tends to deform after implantation, leading to different blood flow patterns, which may lead to tissue growth. Second, the metal structure of the strut just after implantation may not be fully embedded into the endothelium, leaving a portion of the stent strut protruding from the blood vessel wall. The protrusion of the stent strut may create zones where blood flow is circulating or stagnated, leaving platelets and other substances in the bloodstream to accumulate at the stented region (Beier, Ormiston, Webster, & Muller, 2016). Campolo et al. (2014) suggested that, when blood flow is disturbed, endothelial functions will change by gene activation and suppression, making the implanted blood vessel more vulnerable to atherosclerosis and tissue hyperplasia. Stent implantation contributes to the hemodynamic change inside the implanted blood vessel, which may be associated with unwanted vascular responses. Several hemodynamic variables, including wall shear stress (WSS), oscillatory shear index (OSI), relative residence time (RRT), and shear rate, are usually utilized to quantify and assess the hemodynamic environment of the stented blood vessel. The variables can provide insights into the development of stenosis and thrombosis.

2.3.1 Wall shear stress

Wall shear stress is critical in regulating the normal functions of the endothelium (Gijsen et al., 2019). The WSS is the tangential force per unit area. Blood flow exerts WSS on the blood vessel wall, with around 1-2 Pa in coronary arteries and 0.1-0.6 Pa on the venous wall (Roux et al., 2020). Generally, the WSS deforms the endothelial cells on the blood vessel wall to align with blood flow direction, facilitating the endothelial cells to maintain a quiescent state under normal WSS (Gijsen et al., 2019). However, if the endothelial cells are exposed to low or oscillating WSS, gene expressions of adhesive protein and chemokines will be activated, enabling a pro-inflammatory response (Gijsen et al., 2019). Cytokines and growth factors will stimulate endothelial growth, resulting in excessive tissue growth if the WSS is persistently lower than the normal range. The WSS post-stenting will alter the behaviours of endothelial cells and platelets, which can lead to restenosis and repeat interventions.

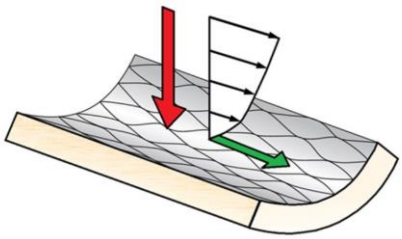

Figure 2.5 The forces that the blood vessel wall is exposed to. Red arrow is the normal force from blood pressure. Green arrow represents the tangential component force, which is the WSS, taken from Gijsen et al., (2019)

The WSS was evaluated at the wall boundary as:

$$\tau_w = \mu \frac{\partial u}{\partial r} \mid r = R \tag{1}$$

where μ is the dynamic viscosity, *u* is the flow velocity along the pipe, and *r* is the radial distance to the centre of the pipe with a radius of R.

The WSS varies during the cardiac cycle. The time-averaged wall shear stress (TAWSS) is also commonly used and computed by averaging the WSS over one cardiac cycle. The TAWSS is defined as:

$$TAWSS = \frac{1}{T}\int_0^T \tau_w \, dt \tag{2}$$

where T is the period of one cardiac cycle, dt is the time derivative, and τ_w represents the shear stress at wall. The TAWSS provides a mean WSS value at the blood vessel wall while the WSS is typically computed at a certain time point.

2.3.2 Oscillatory shear index

Variables derived from the WSS are also frequently used to assess the hemodynamic behaviour of blood vessels. The oscillatory shear index (OSI) identifies regions where the WSS changes direction from the predominant blood flow direction. Locations with a higher OSI usually have a low oscillatory WSS, which incur a greater risk of blood vessel narrowing (Zarins et al., 1983). OSI is calculated as:

$$\mathrm{OSI} = \frac{1}{2}\left(1 - \frac{\left|\int_0^T \vec{\tau}_w \, dt\right|}{\int_0^T |\vec{\tau}_w| \, dt}\right) \tag{3}$$

and ranges from 0 to 0.5, where 0 indicates the WSS aligns with blood flow without any oscillation. High OSI suggests low and oscillatory WSS. For example, an OSI of 0.5 represents a reversed direction to blood flow during the cardiac cycle. A high OSI is associated with neointimal hyperplasia. The oscillating WSS may increase the permeability of the endothelial membrane (Cunningham & Gotlieb, 2004). The membrane will allow more substance to travel into the damaged endothelium and smooth muscle cells to cause cell proliferation and migration. Therefore, OSI would be another indicator of intimal thickening.

2.3.3 Residence time

Particle residence time or relative residence time describes how long a fluid parcel spends in a region of interest and may help identify locations where the flow becomes stagnant. Residence time could also be used to highlight areas with high concentrations of platelets and growth factors to predict the risk of thrombosis (Reza & Arzani, 2019). In stagnant flow, there will be a higher possibility that the platelets will attach to the surface of the blood vessel wall, which favours platelet accumulation between the stent and the vessel wall. A long residence time is linked to a low WSS and a high OSI. Residence time is often calculated as (Soulis et al., 2011):

$$RRT = [(1 - 2 * OSI) * TAWSS]^{-1} \quad (4)$$

where RRT is the residence time. From the equation, a large residence time could result from a highly oscillatory flow and a low WSS.

2.3.4 Shear rate

In coronary stenting, a high flow condition promotes thrombus formation. Shear-induced platelet aggregation is a common pathway for thrombosis in arteries (Casa, Deaton, & Ku, 2015). Shear rate is defined as the rate of change in velocity at which one layer of fluid passes over an adjacent layer. In short, the shear rate is the velocity gradient over the radial distance to the blood vessel wall. A high shear rate of blood flow generates an explosion of thrombus growth, with rapid platelet aggregation and accumulation (Kolandaivelu et al., 2011). Although platelets contribute to only a tiny portion of the blood volume (1%~2%), the high shear rate enhances the movement and collision of platelet towards regions next to the blood vessel wall. The platelets tend to adhere to thrombogenic surfaces, including sub-endothelial collagen and artificial materials like metal. A shear rate greater than 10,000 s^{-1} could result in significant platelet activation (Holme et al., 1997).

2.4 Research gap in the hemodynamic of venous stents

In the previous section, the literature on stent restenosis and stent thrombosis was reviewed for arterial and venous stents. There exists a large body of literature for arterial stents, especially coronary artery stents. The mechanisms of stent restenosis and thrombosis are well defined. The key hemodynamic variables are studied extensively. **On the contrary, studies of venous stents were rare, with less clinical research than arterial stents**. This is due to the fact that venous blood vessels diseases that require a venous stent are less prevalent than arterial blood vessel disease, such as coronary artery disease. It was the high rate of restenosis (~30%) that induced extensive research in coronary stents. Venous stents, especially those implanted to treat cerebral blood vessel diseases, are much less prevalent. Therefore, clinical data on venous stent stenosis and thrombosis is limited. Without the knowledge about venous stent stenosis and thrombosis, it remains challenging to understand the impact of implanting a venous stent in the brain.

One thing in common between the development of arterial and venous stent complications is that **blood flow plays an essential role in promoting vascular health**. Blood flow regulates the normal functions of the endothelium in both arteries and veins. After stenting, a change in blood flow might induce stent complications with abnormal endothelial functions and platelet-related thrombosis. The clinical data and research from arterial and venous stent studies suggest that studying blood flow post-stenting is critical for stent complication predictions and preventions. The literature in

computational modelling can help understand how the stent alters blood flow inside the blood vessel, such as the cerebral venous sinus, to mitigate the risks of potential stent complications.

2.5 Computational Fluid Dynamics

Computational Fluid Dynamics (CFD) is a commonly used approach to study blood flow in stented blood vessels. CFD software solves the Navier-Stokes equations of fluid flow. It generates flow velocity, mechanical forces, and streamline results, which can be used to analyse the biomechanical behaviour of stented blood vessels. CFD provides a detailed visualization of blood flow. The WSS can be computed on the blood vessel wall, which could not be measured by other methods, including *in-vivo* experiments and imaging measurements. In the literature, numerous studies on arterial stents have demonstrated the feasibility of CFD in predicting stenosis and thrombosis (Morris et al., 2015). Venous stents, however, became of interest only in recent years (Ying et al., 2020).

2.5.1 Numerical simulation

Modelling of the stented blood vessel was initially constructed in two dimensions by Berry et al. (Berry et al., 2000). In their model, the blood vessel wall was represented by a flat plate and the stent struts were modelled as protruding objects with the distance between them, as shown in Figure 2.6.

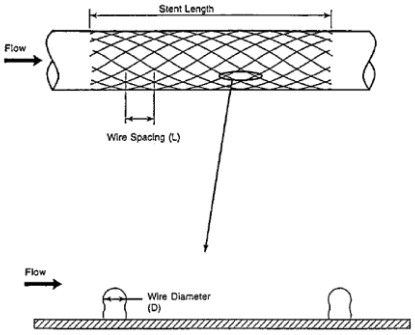

Figure 2.6 The 2D model from Berry et al. (2000), where only the near-wall region was modelled.

Figure 2.7 shows the resulting shear rate contour and flow streamline. This early work highlighted flow stagnation zones between the stent struts, where the velocity is almost zero. Simulation in two dimensions is computationally inexpensive. However, a 2D model might not capture the full view of the flow through the stent due to geometry simplification.

Figure 2.7 Simulation result of an early study: Shear rate contour (color) and streamline (white line) (Berry et al., 2000).

Three-dimensional models provide a comprehensive visualization of the flow distribution and mechanical forces on the blood vessel wall. Typically, an idealized blood vessel is constructed by computer-aided design (CAD) software (Gundert et al., 2011). The blood vessel is usually simplified as a cylinder. The stent model is virtually implanted into a simple cylindrical model using Boolean subtraction (Gundert et al., 2011).

The use of a 3D model enables the prediction of abnormal hemodynamic behaviour of a stented blood vessel. Ladisa et al. (2003) compared the unstented model and stented model, showing that the WSS was reduced significantly in the stented model, as shown in Figure 2.8. The reduction may play a role in subsequent intimal thickening around the stent cells. They also demonstrated that the alteration in WSS may help predict the sites of intimal thickening supported by the vascular histology (LaDisa et al., 2003). During their experiment, a stented iliac artery was sliced after 21 days of implantation and examined under a microscope to measure the extent of tissue hyperplasia. They observed cell proliferation around the stent strut. There was little or no tissue growth at locations where the WSS was normal. These findings have suggested that an idealized model could be used to assess the risk of stenosis and provides a feasible approach to study haemodynamics.

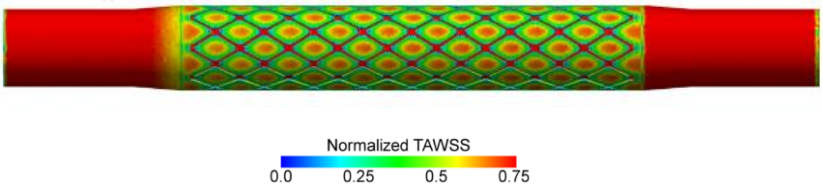

Figure 2.8 Time-averaged wall shear stress result computed from a 3D cylindrical model taken from LaDisa et al. (2003).

Idealized models allow the parameterization of the stent. Numerous research has investigated the optimal stent design, which usually poses minimum interference to the hemodynamic environment. Researchers construct models with various strut thickness, strut angle, diameter, and length of the stent to study the impact of stent designs on blood flow. Several works have investigated the optimal stent strut profile and strut angle (LaDisa et al., 2005).

However, an idealized model usually simplifies the blood vessel geometry, ignoring complicated anatomical features of a blood vessel. Those anatomical features may include geometric asymmetry, blood vessel tapering, irregular cross-sections, and curvature. The geometric simplification might hinder the accuracy of flow prediction inside a human blood vessel. However, idealized models provide a fundamental idea of the hemodynamic change induced by various stent designs. For a novel stent like the stent-electrode device, an idealized model could be suitable to explore the hemodynamic change caused by stent-electrode. Currently, there was no CFD modelling of a stent-electrode device in the literature yet. It implies that the CFD of stent-electrode will be novel and beneficial to future CFD modelling of stents.

An anatomical CFD blood vessel model enables the study of blood flow for a specific subject. He et al. (2020) associated the CFD results with an animal experiment. Rabbits were implanted with wingspan stents in their carotid arteries with tissue injury intentionally made by stent over-expansion. The stent was implanted for five weeks for stenosis to develop. Then, angiography was used to construct the anatomical model. Ultrasound was utilized to obtain flow velocity as the

boundary conditions of the CFD model. CFD results, such as the oscillatory shear index distribution at the wall of the blood vessel lumen, are shown in Figure 2.9. The OSI was the highest proximal to blood flow due to stent expansion in the blood vessel lumen. Their results indicated that this region was more likely to show in-stent restenosis.

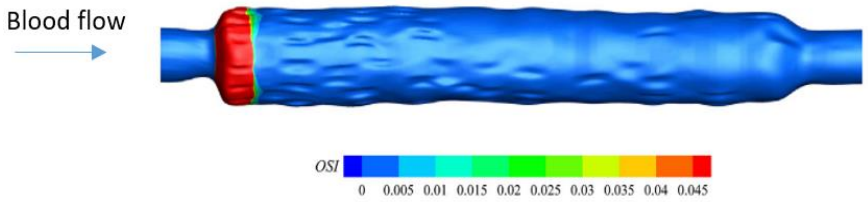

Figure 2.9 Oscillatory Shear Index (OSI) distribution in a rabbit carotid artery model (He et al., 2020).

Neointima refers to the newly deposited tissue around the stent implant. The tissue consists of smooth muscle cells, macrophages, fibroblast, and collagen, which encapsulate an extracellular matrix (ECM) around the stent implant. Figure 2.10 shows the Haematoxylin and Eosin staining of the blood vessel cross section. He et al. (2020) reported more thickening in regions proximal to the flow than middle and distal regions. Neointima thickening was found inferior to the stent struts, as shown in Figure 2.10. On the left, the white circular area surrounded by the stained cells (pink colour) was occupied by the stent strut before the stent strut was removed from the blood vessel. From the right, the endothelium was visible and packed in a dense pattern below the stent strut above the smooth muscle cells. More importantly, cell necrosis (reddish colour) was found near the stent. For those blood vessel slices, the thickness of tissue necrosis was the highest at the proximal region of the stented artery. It was evident that there was a strong correlation between the hemodynamic patterns and intimal thickening.

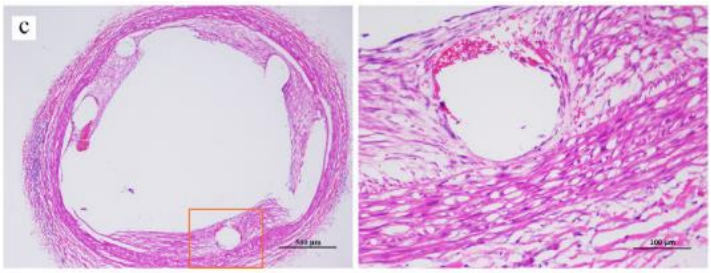

Figure 2.10 Cell staining of a cross-section slice in the proximal region of the stented artery taken from He et al. (2020). The right figure is a zoomed view of the left.

Anatomical models have also been used to study blood flow in the cerebral venous sinus. Liu et al. (2019) investigated the haemodynamics of transverse sinus stenosis. Flow results, including pressure, acceleration, and velocity, were used to examine the effect of stenosis on blood flow. Their results also identified the effect of different body positions on stenotic flow. Levitt et al. presented a patient-specific model to quantify the haemodynamics of venous sinus stenosis (Levitt et al., 2016). They found a higher blood flow and WSS associated with pathologic pressure gradient

compared with regular pressure gradient. In most of the venous sinus modelling works, a Newtonian blood flow property, which assumes blood to flow like water, was implemented for computation.

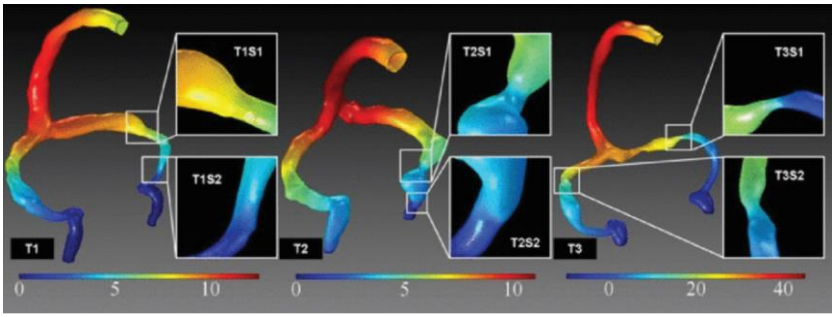

Figure 2.11 Pressure results in the superior sagittal sinus and transverse sinuses taken from Liu et al (2019).

Overall, a 3D anatomical model may deliver a more realistic description of the hemodynamic inside the stented blood vessel compared with an idealized 3D model. With Computer Tomography (CT) and Magnetic Resonance Imaging (MRI), a patient-specific model could be generated for CFD simulation, which may enhance the accuracy of the CFD results. Constructing an anatomical CFD model requires extra efforts in model construction and additional measurements. This approach is still ubiquitous to study the hemodynamic behaviour of blood vessels because of its potential in explaining the pathology of stenting-related complications.

2.5.2 Research gap in CFD modelling of venous stents in the brain

There are research gaps in modelling the blood flow in the venous blood vessels in the brain, which hinder the development of stent-electrode arrays. Without the literature and clinical data, it remains a challenge to evaluate the impact of placing a stent-electrode array into the venous blood vessels. There can be unfavoured tissue response if the design of the device is not tailored to the specific biomechanical environment where the stent resides in. The stent can disturb the normal blood flow and vascular health. This section highlights the research gaps in the literature and identify the modelling work require to develop the stent-electrode array.

Cerebral venous stent is always ignored when modelling venous sinuses. There should be a computational model of the stent-electrode array to evaluate its impact on blood flow. Anatomical models of venous sinuses were used. This is because the cerebral venous sinuses have complex shapes, especially the superior sagittal sinus, which has a triangular lumen shape. To study venous flow in the brain, a large portion of the cerebral venous system was generated, including the superior sagittal sinus, straight sinus, a pair of transverse sinuses, and a pair of jugular veins. However, the presence of a venous stent was always ignored in the studies due to the miniature size of stent and large size of the cerebral venous network (Fillingham et al., 2023). This suggests that the blood flow patterns near the stent becomes unavailable. As a result, the subsequent tissue growth patterns are unknown for venous sinus stents.

There is currently no modelling works studying venous stent designs. Design parameters of a stent are crucial to its long-term safety. In the literature, idealized models with various stents have covered generic and commercially available stents mainly for arteries. However, designs that are specific to stent-electrode have not been attempted in CFD modelling. A research gap presents in the study of the stent-electrode design, such as the size and number of electrodes. This means that

the blood flow impact of stent-electrode arrays is unknown. It is necessary to determine the optimal design parameters to minimize the risk of tissue overgrowth.

The current literature lacks examination of local blood flow and tissue growth near the stent struts. Local change in blood flow was found to promote excessive tissue growth in the blood vessels. However, there has not been studies that focus on blood flow and venous tissue overgrowth. Recent studies focus on the efficacy of venous stenting in restoring blood flow than the impact of stenting. Most of the literature compares blood flow and blood pressure before and after venous stenting to demonstrate the efficacy of stenting. Currently, there has been no modelling work addressing the impact of stenting on re-endothelialisation and tissue overgrowth. The tissue growth happened in stent-electrode arrays remains unexplained. To understand the mechanism of venous tissue growth, a close examination of local blood flow and tissue growth will be required.

Anatomical models of narrowed blood vessels are always used to study blood flow in the cerebral blood vessels (Liu et al., 2019). From the literature, there was a strong interest in the study of venous flow in the cerebral venous sinus with stenosis and intracranial hypertension (Levitt et al., 2016). Those studies focused more on the impact of a pre-existing venous sinus stenosis. Computational models of venous sinuses usually focus on understanding the impact of disease, including narrowed blood vessel geometry and abnormal blood flow conditions. As a result, little is known about implanting a stent into a healthy blood vessel. Referring to data from a model with hypertension may not be appropriate for studying stent-electrode arrays. The diseased condition introduces abnormal blood pressure and geometries, which can produce different blood flow and wall shear stress results compared to a healthy vein model. Therefore, a computational model of a healthy cerebral venous blood vessel should be constructed to evaluate the impact of stent-electrode arrays.

A triangular CFD model could be established and studied. Since the human SSS has a triangular cross-section, a cylindrical model might not be appropriate to construct an idealized model. There was a limited number of studies related to the triangular cross-section in blood vessel CFD modelling. Lorenzini and Casalena (Lorenzini & Casalena, 2008) studied blood flow in stenotic arteries with various shapes of atherosclerotic plaque. In their model, the geometry of the blood vessel transformed from a circular lumen into a triangular cross-section at the stenotic region, which generated disturbance to blood flow. Another studied the triangular prism model simulated fluid flow and heat transfer through a triangular duct for industrial applications (Kumar et al., 2016). The geometry size and flow conditions were different from pulsatile blood flow in the human blood vessel.

2.5.3 Model validation

A validation study ensures that the CFD simulation estimates the realistic blood dynamics in a blood vessel. However, CFD validation remained challenging due to the difficulty of taking measurements directly inside a small blood vessel in the body. As alternatives, *In-vitro* flow experiments and medical imaging techniques have always been utilized to validate the CFD model of blood vessels.

Particle image velocimetry was a technique to validate blood vessel models. Tomaszewski et al. (2020) fixed a stent in a silicon tube. Fluid flow was measured by illuminating particles whose movement was captured by a camera. A pump was used to drive pulsatile flows in the experiment. As shown in Figure 2.12, the experiment measured a parabolic flow profile with a similar average

velocity to the simulation results. In addition, it could also visualize the flow speed over the entire flow domain (Figure 2.12. Right). However, the asymmetric flow was observed by the camera in the experiment (red curve). With a low spatial resolution, the WSS could not be accurately computed from the velocimetry. The fluid flow was obscured near the blood vessel wall due to its low speed. Nevertheless, particle image velocimetry still provided a feasible approach to validate CFD models.

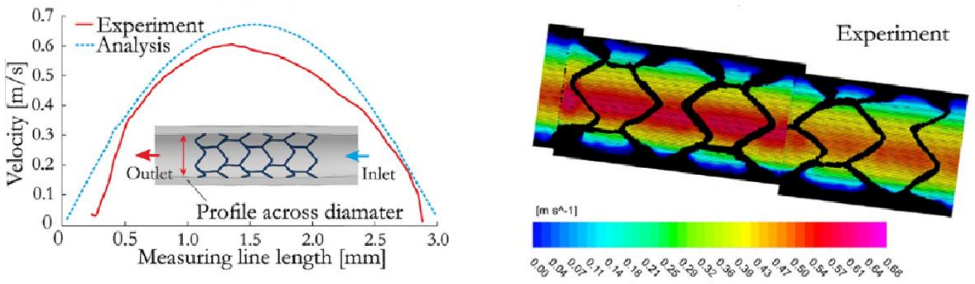

Figure 2.12 Left: Flow profile across the outlet diameter for the experiment and CFD analysis. Right: Maps of time average velocity generated from experiment

Medical imaging techniques, such as phase-contrast magnetic resonance imaging, could measure the cross-sectional velocity field to validate the CFD model of the blood vessel. Sindeev et al. (2018) validated their patient specific CFD model against 4D flow MRI. In their study, the flow velocity magnitude and distribution were similar to data measured from 4D MRI (Figure 2.13). In addition, doppler ultrasound can also be used to measure blood flow. However, using ultrasound requires an acoustic window for signal transduction. The bones between the ultrasound transducer and the target blood vessel may block the velocity-encoded signals (Göbl et al., 2017). Thus, velocity measurement using ultrasound is not always feasible.

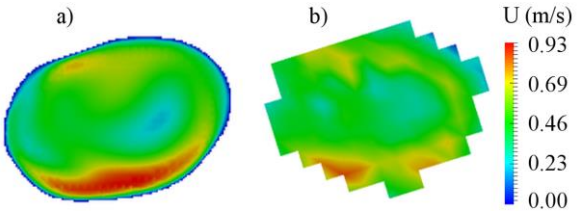

Figure 2.13 Velocity distribution for central cross-section of aneurysms from a) CFD model and b) 4D MRI, taken from Sindeev et al. (2018).

2.6 Critical Summary

Stent-electrode technology has been developed for endovascular electrical recording and stimulation, which holds promise to treat patients with neurological disorders. The stent-electrode is usually implanted in the superior sagittal sinus, which is located above the motor cortex. Due to a lack of long-term clinical data on humans, the impact of implanting a stent-electrode device into the SSS and other blood vessels in the cerebral venous system remains unanswered.

From experiences in stenting, the long-term effect of a stent device on the implanted blood vessel is strongly influenced by blood flow or the haemodynamics of the implanted blood vessel. In this chapter, major stent complications, including stenosis and thrombosis, were reviewed across

arterial and venous stents. The development of tissue hyperplasia, as well as the formation of occlusive thrombus, were closely associated with the hemodynamic variables of the blood vessel post-stenting. Key variables, including the flow velocity, wall shear stress, and shear rate, were critical to the physiology of endothelium and platelets in the blood vessel. However, the literature also indicates research gaps in the study of venous sinus stenting, where the effect of stenting on the cerebral venous sinus requires further investigation.

It is usually challenging to obtain blood flow patterns around the stents to analyse the haemodynamics. Computational Fluid Dynamics (CFD) is a widely accepted numerical simulation approach to visualize the fine details of blood flow. CFD has the level of accuracy that other methods, such as *in-vivo* measurements and medical imaging, cannot easily achieve. In CFD modelling, three-dimensional idealized models and anatomical models of blood vessels are the current state of the art, with numerous simulations performed on arterial stents. CFD modelling of the cerebral venous sinus was limited to a small patient group with intracranial hypertension. There were few CFD models that involves the presence of venous sinus stents inside the cerebral venous sinus. Furthermore, the triangular cross-section of the human SSS has not been studied in any of the current models, which raises a question on how the triangular configuration will influence the haemodynamics of SSS and stent-electrode. Therefore, constructing a computational model of the human superior sagittal sinus will be novel in this field. The proposed work will benefit the research of the stent-electrode device by predicting the hemodynamic behaviour post-stenting.

To unveil the hemodynamic effect of a stent-electrode device on the human superior sagittal sinus, this PhD research will utilize CFD modelling as the research tool. An idealized model will be implemented to examine the hemodynamic impact of various stent-electrode designs. The model will also be further developed to depict the anatomical features of a human SSS and their effect on blood flow. The insights generated from the proposed computational models are expected to fill in the research gaps in cerebral venous stenting and CFD modelling.

Chapter 3 – Methods

Chapter 3.1.2 has been published on 2023/7/24. Other sections have not been published.

> Qi, W., Ooi, A., Grayden, D., & John, S. (2023). Computational fluid dynamics of stent-mounted neural interfaces in an idealized cerebral venous sinus. *Proceedings of the Annual International Conference of the IEEE Engineering in Medicine and Biology Society, 2023*, 1-4. https://doi.org/10.1109/EMBC40787.2023.10341099

Computational Fluid Dynamics (CFD) modelling was used to evaluate the blood flow impact of and its relationship with in-vivo tissue responses in venous stents and endovascular neural interfaces. This chapter discusses the methodologies for **pre-processing, solving, post-processing, and validation** of the computational models used in subsequent chapters (4-6). In addition, this chapter provides an overview of animal experiments. The animal experiments were conducted to provide realistic input data for CFD models. The experimental results, such as blood flow, validated the CFD models. The tissue growth data collected from the experiments was compared with the simulated blood flow results to study the correlation between blood flow and tissue growth.

The first project in Chapter 4 used a simplified Computational Fluid Dynamics model to identify the key factors influencing blood flow. Then, the model was further developed in Chapter 5 by adding more complex geometric features, such as varying lumen diameter and deformation due to stent expansion. Finally, an animal-specific computational model was constructed in Chapter 6 using realistic blood vessel geometry obtained from medical imaging and venous flow obtained from experimental measurements.

3.1 Computational Modelling

CFD models were built using COMSOL (COMSOL Multiphysics, Burlington, MA), a finite element method software. The generic workflow is described here (Figure 3.1). A COMSOL model requires geometry, material property, and boundary conditions as model inputs. The model then underwent meshing and passed to the solver in the software to calculate the blood flow results. Animal experiments were conducted to provide realistic input and validation.

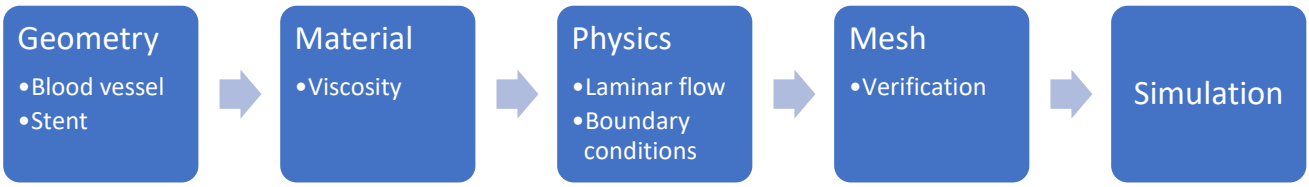

Figure 3.1 The workflow of constructing a CFD model in COMSOL.

3.1.1 Geometry

A CFD model of stented blood vessel requires a flow domain where blood flow is simulated. The geometries of the blood vessels and stents of interest were the necessary geometries to construct the flow domain. The geometries were usually represented by idealized geometries constructed by CAD software or anatomical geometries obtained from medical imaging techniques. In Chapters 4

and 5, blood vessels were constructed using idealized geometries, such as cylinder and cones. The design module of COMSOL Multiphysics was used to generate blood vessel geometry for sheep and humans.

Stent-mounted neural interfaces were constructed for CFD models. First, a 2D drawing of the stent-electrode pattern (.DXF file) was delineated on a 2D plane using COMSOL, approximating the dimensions of the stent-electrode array as described in the literature (Opie et al., 2018; Oxley et al., 2016). Subsequently, a thickness of 50 µm was applied to the stent pattern by extruding the 2D plane, thereby transforming the design into a metallic sheet. This sheet was then contoured into a tubular mesh structure using CAD software, ensuring its compatibility with the dimensions of typical blood vessels. This fundamental geometric model serves as the basis for the models presented in Chapter 4 and Chapter 5. In Chapter 6, a commercial venous stent was used. The stent geometry was reconstructed from micro-CT scans.

3.1.2 Three-dimensional model of the stented venous sinus

The human SSS geometry was approximated as a cylinder with the Design Module of COMSOL Multiphysics (COMSOL Multiphysics, 2021). The venous sinus was a rigid and non-stretchable pipe with a fixed diameter of 6 mm and a centreline length of 60 mm. The CAD module of COMSOL Multiphysics was used to create the stent cell pattern for the stent-mounted neural interface (Oxley et al., 2016). To achieve virtual implantation of the stent into the blood vessel, the stent volume was subtracted from the flow domain using the Boolean operation, with a strut thickness of 50 µm. Finally, the stented blood vessel model, shown in Figure 4.1, was meshed for computation of fluid flow in ANSYS Fluent software (ANSYS, 2021). To investigate the effect of stent designs on blood flow, several stented blood vessel models were constructed with different design characteristics, including electrode size, arrangement, and number of electrodes (quantity), listed in Table I.

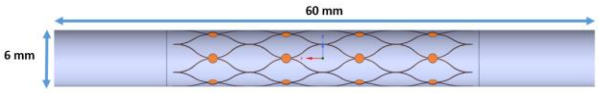

Figure 4.1 The geometry of stented venous sinus with length and diameter labelled. The electrodes (orange) were in a parallel pattern.

Simulations were conducted by solving the transient incompressible viscous flow. The density (ρ) was set to be 1060 (kg/m^3) and the dynamic viscosity (μ) was taken to be 0.0035 (kg/m·s) (Hajati et al., 2020). A pulsatile venous flow waveform from healthy volunteers from Rivera et al. (2017) was applied. The model inlet was extended for the flow to develop. The CFD model neglected any blood vessel movements within the cardiac cycle.

TABLE I. Summary of all numerical cases

Case	Design Characteristics of Stent		
	Electrode Size (μm)	***Arrangement***	***Quantity***
1	0 (no electrode)	Parallel	24
2	500	Parallel	24
3	750	Parallel	24
4	1000	Parallel	12
5	1000	Alternating	12
6	1000	Parallel	18
7	1000	Parallel	24
8	2000	Parallel	24

3.1.3 non-Newtonian fluid property

Blood is a shear-thinning fluid, meaning its fluid viscosity (resistance to flow) decreases as the shear rate (rate of flow) increases. Thus, a non-Newtonian flow model was used to describe the viscosity of CFD models. For a non-Newtonian fluid, the viscosity of the blood (μ) depended on the shear rate of the flow which could be described by the Carreau model:

$$\mu = \mu_\infty + (\mu_0 - \mu_\infty)[1 + (\lambda\dot{\gamma})^2]^{\frac{n-1}{2}}$$

The terms μ_0 and μ_∞ were viscosities at zero and infinite shear rate $\dot{\gamma}$. The values are 0.056 and 0.00345 pascal seconds respectively. The relaxation time λ and power index n were $3.313\ s$ and 0.3568, which were commonly used in the literature (Shibeshi & Collins, 2005). Despite of its better accuracy against the Newtonian model, most of the CFD stented blood vessel models still used a Newtonian model with the justification that blood followed the Newtonian nature for a shear rate greater than $100\ s^{-1}$. In this project, a non-Newtonian fluid was used since venous flow are generally slower and less pulsatile, meaning the shear rate will be lower and the viscosity will be higher than reported values in arterial stents.

3.1.4 Physics – Laminar flow

For all CFD models, a laminar flow model was employed, assuming incompressible, transient, and single-phase flow. The Reynolds number in veins, typically less than 300, indicated laminar flow behaviour. Transient simulation was selected due to the periodic nature of blood flow over cardiac cycles. The laminar model utilized the Navier-Stokes equation to solve the motion of the viscous fluid, maintaining conservation of momentum.

$$\frac{\partial}{\partial t}(\rho \boldsymbol{v}) + \nabla \cdot \rho \boldsymbol{v}\boldsymbol{v}^T = -\nabla p - \nabla \cdot \boldsymbol{\tau} + \rho \boldsymbol{g} \qquad (1)$$

Where ρ was the density of the fluid, $\boldsymbol{v}$ was the velocity vector and $\boldsymbol{v}^T$ was the transposed matrix of velocity, $\boldsymbol{\nabla}$ was the divergence, p was the pressure, $\boldsymbol{\tau}$ was the stress tensor, and g was the gravitational acceleration.

The N-S equation also included the continuity equation (conservation of mass):

$$\frac{\partial \rho}{\partial t} + \boldsymbol{\nabla} \cdot \rho \boldsymbol{v} = 0 \qquad (2)$$

Several simplifications were made. Gravitational acceleration was omitted because it has little effect on blood flow. The density (ρ) was assumed constant for an incompressible fluid. Consequently, Equations (1) and (2) were simplified to:

$$\rho\left(\frac{\partial \boldsymbol{v}}{\partial t} + \boldsymbol{\nabla} \cdot \boldsymbol{v}\boldsymbol{v}^T\right) = -\boldsymbol{\nabla} p - \boldsymbol{\nabla} \cdot \boldsymbol{\tau} \qquad (3)$$

$$\boldsymbol{\nabla} \cdot \boldsymbol{v} = 0 \qquad (4)$$

where the stress term $\boldsymbol{\tau}$ was defined as:

$$\boldsymbol{\tau} = -\mu(\boldsymbol{\nabla v} + (\boldsymbol{\nabla v})^{\mathrm{T}}) + \frac{2}{3}(\mu - \kappa)(\boldsymbol{\nabla} \cdot \boldsymbol{v})\boldsymbol{\delta} \qquad (5)$$

For incompressible flow, the bulk viscosity term (κ) was irrelevant. Also, the $\boldsymbol{\nabla} \cdot \boldsymbol{v}$ term became zero due to continuity. μ is the fluid viscosity. Equation (5) became:

$$\boldsymbol{\tau} = -\mu(\boldsymbol{\nabla v} + (\boldsymbol{\nabla v})^{\mathrm{T}}) \qquad (6)$$

Substitute back into the N-S equation (3), the finalized form became:

$$\rho\left(\frac{\partial \boldsymbol{v}}{\partial t} + \boldsymbol{\nabla} \cdot \boldsymbol{v}\boldsymbol{v}^T\right) = -\boldsymbol{\nabla} p + \boldsymbol{\nabla} \cdot [\mu(\boldsymbol{\nabla v} + (\boldsymbol{\nabla v})^{\mathrm{T}})] \qquad (7)$$

After simplifying Equation (7), the N-S equation for laminar flow became:

$$\rho\left[\frac{\partial \boldsymbol{v}}{\partial t} + (\boldsymbol{v} \cdot \boldsymbol{\nabla})\boldsymbol{v}\right] = -\boldsymbol{\nabla} p + \mu \boldsymbol{\nabla^2 v} \qquad (8)$$

$$\boldsymbol{\nabla} \cdot \boldsymbol{v} = 0 \qquad (9)$$

The set of N-S equations solved the velocity vector $\boldsymbol{v}$ and pressure p for each finite volume element inside the flow domain over one cardiac cycle. The N-S equations contained 4 equations, the momentum conservation in x, y, and z direction (Cartesian coordinates), as well as the continuity equation. There were also four dependent variables including the x, y, and z component of velocity (u, v, and w, respectively) with units in m/s and the pressure in Pascal which were the unknowns.

3.1.5 Boundary conditions

Boundary conditions are essential for solving the Navier-Stokes (N-S) equations. In this study, a time-dependent velocity profile was applied at the inlet boundary. This velocity profile shown in Figure 3.2 was derived from the digitized waveform presented by Rivera-Rivera et al. (2017), which was obtained from the flow rate (mL/min) of the superior sagittal sinus in 26 healthy individuals aged 66 to 85 years, measured using Phase-Contrast Magnetic Resonance Imaging. The waveform in their publication represented the pulsatile flow averaged over one cardiac cycle for the 26 individuals.

Variations in blood flow velocity due to respiratory effect was not present in Rivera-Rivera et al. (2017). After digitization, the waveform was fitted with a Fourier series to approximate its shape. Since blood flow is periodic, the Fourier series ensured the waveform's periodicity by utilizing sine and cosine functions.

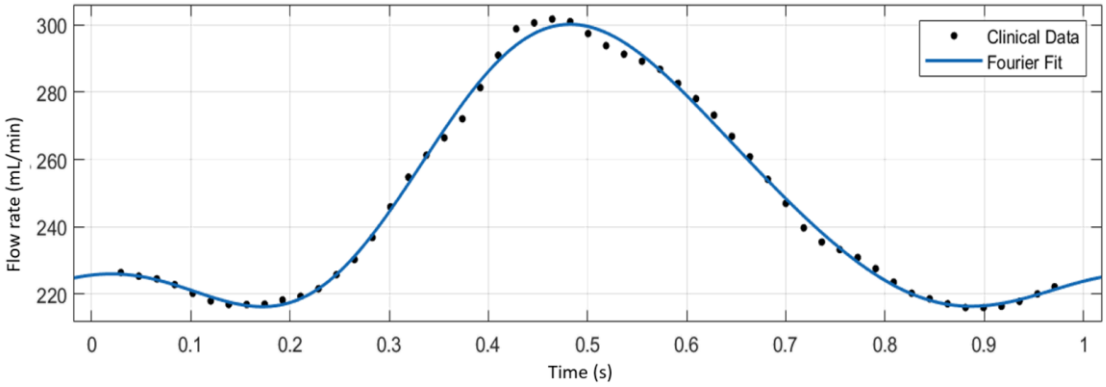

Figure 3.2 The average velocity of blood flow in the superior sagittal sinus over time. A fitting curve using Fourier series was applied to the data point generated from digitization.

A sum of three sine functions, three cosine functions, and a constant were used to capture the shape of the waveform. The Fourier Fit had an equation:

$$v_o(t) = a_0 + \sum_{n=1}^{3} a_n \cos(n\omega t) + b_n \sin(n\omega t) \qquad (10)$$

The series of coefficients a, b, and ω in the velocity waveform were recorded in the ***Appendix***. A total of six trigonometry functions were considered sufficient to capture the shape of the waveform. Although a higher number of terms could be used for better alignment of the fitting curve with the clinical data point, it may overfit the clinical data and became unsuitable for a generalized and idealized model.

The velocity also varied with the spatial x, y, and z coordinates on the inlet boundary. Different from the parabolic flow profile in laminar flow, the pulsatile behaviour of flow was described by the Bessel function. The profile was given by a complex equation [equation 11]:

$$v(r,t) = v_0(t) \cdot Re\left\{\left[1 - 2\eta \cdot i^{-\frac{3}{2}} \cdot \frac{J_1\left(\eta^{-1} \cdot i^{\frac{3}{2}}\right)}{J_0\left(\eta^{-1} \cdot i^{\frac{3}{2}}\right)}\right]^{-1} \cdot \left[1 - \frac{J_0\left(\eta^{-1} \cdot i^{\frac{3}{2}} \cdot \frac{2r}{D}\right)}{J_0\left(\eta^{-1} i^{\frac{3}{2}}\right)}\right]\right\} \qquad (11)$$

The term $v_0(t)$ was the time-dependent waveform from the Fourier fit discussed above. $Re\{\}$ represented the operation that taking the real part of the expression inside. The term η was the inverse of Womersley number. i was the imaginary number. $J_n()$ was the Bessel function of the first kind in n^{th} order. r was the radial position and D was the diameter of the pipe. Although the equation was complex, in COMSOL, the fully developed flow option was selected to implement the Womersley flow profile. This option involved extending the inlet region so that the flow could

develop into a fully developed flow profile beyond this extended region. By doing so, the need for complex equations and Bessel functions was circumvented, resulting in a simpler and faster setup process. To ensure the flow achieved full development, the velocity at the actual inlet was compared with the analytical solution generated by MATLAB code (MATLAB. (2022a). Natick, Massachusetts: The MathWorks Inc.). This comparison confirmed that the flow profile was independent of further extension of the inlet (Figure 3.3).

The outlet boundary was set to a pressure of 0 Pa because venous outflow, unlike arterial flow, faces minimal resistance from capillaries. Cerebral vein blood flow typically has low pressure gradient, which ranged from 1 to 3 mmHg in healthy individuals (Boddu et al., 2018) compared to arterial flow, exerting little effect on the blood flow. Therefore, a 0 Pa outlet condition was implemented in the model. For blood vessel wall boundaries, including the strut surface and blood vessel wall, a non-slip condition was applied, indicating zero velocity at these boundaries. The model was symmetric about the sagittal plane, where a symmetric boundary condition was used. This assumption allowed for zero fluxes of all quantities across the symmetric boundary, reducing the number of mesh elements and lowering the computational cost.

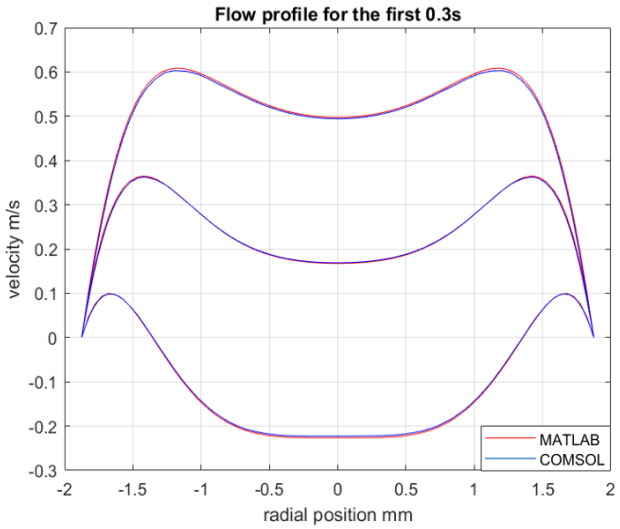

Figure 3.3 A Womersley flow profile was implemented in COMSOL by using the fully developed flow option in COMSOL. The flow profile matched between the simulation (blue) and analytical flow profile (red).

3.1.6 Mesh

The region encompassed by the blood vessels and the stent geometry defines the area where blood flows. To analyse blood flow, this region is divided into infinitesimal parts called finite elements by the computational domain. This division enables the solution of differential equations and the tracking of physical quantities such as blood flow velocity and blood pressure throughout the domain. Simulation was carried out on the same model but with different mesh sizes to determine the optimal mesh size that produces stable and accurate results while saving computational time. Mesh convergence analysis was conducted to determine the optimal mesh size and parameters that produce fast and accurate results. From the mesh convergence plot below (Figure 3.4), Case 2 in table 1 was set up. COMSOL offers different mesh sizes (coarser, coarse, normal, fine, and finer). A time-dependent flow profile was compared to determine the optimal size to mesh the blood vessel.

Figure 3.4 shows little difference in the flow velocity for those COMSOL built-in mesh sizes. Various mesh sizes were tested for the mesh of stent, of which the metal struts are much smaller than the blood vessel. In this case, a self-defined mesh size was implemented for the stent. The total number of mesh elements was then used as a metric for mesh size for simplicity. Models that contained 0.5, 0.75, 1, 1.5, 2.5, 3, and 4.5 million mesh elements were generated from different mesh size around stent and the WSS was calculated. The area with a low WSS (WSS < 0.5 Pa), which was critical in assessing blood flow impact, was used to indicate model accuracy. The plot shows convergence of result at 2.5 million mesh elements, which were used as the default mesh size for all the remaining simulation (Figure 3.4B). The time-dependent flow velocity profile generated from simulation was compared with analytical results for verification (Figure 3.3). The minimum mesh size (finest mesh) of stent region in the flow domain was set to be 0.02 mm (20 µm) to capture the fine details near the stent struts and corners (Figure 3.4C).

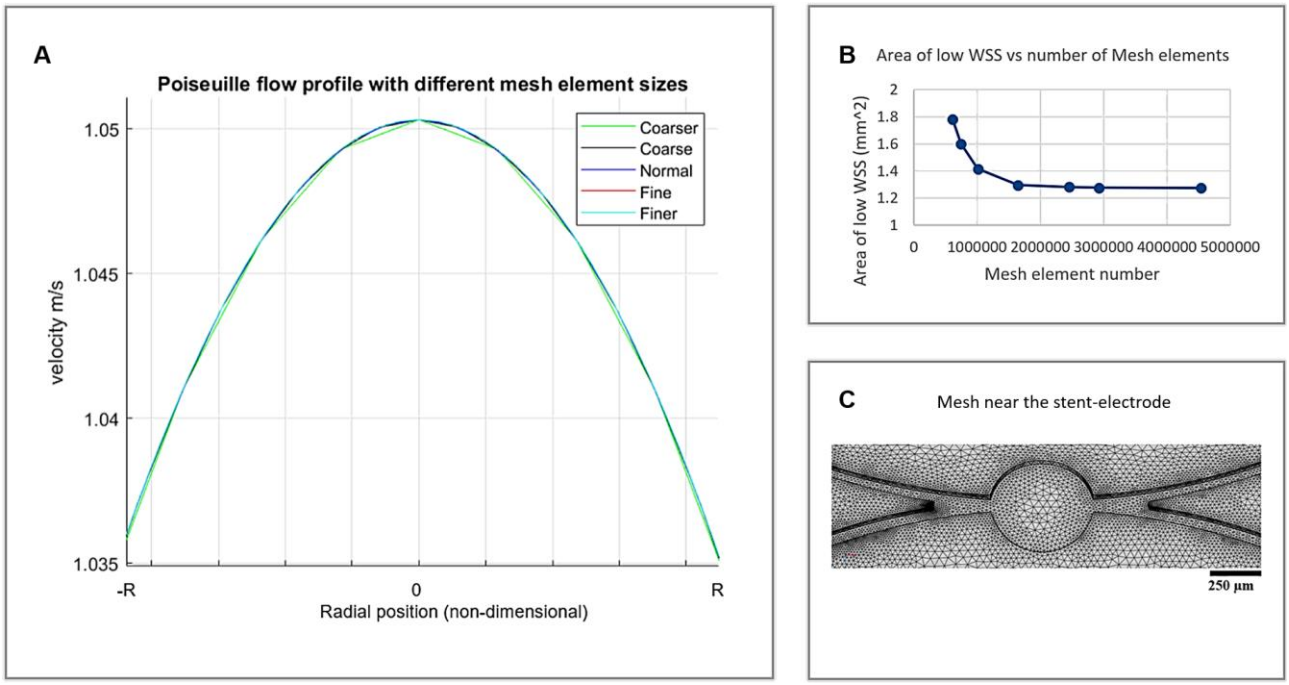

Figure 3.4 Time-averaged flow profile with different mesh sizes for the blood vessel (A). The area of wall shear < 0.1 Pa plotted against the number of mesh element used (B). The final mesh near the stent-electrode (C).

3.1.7 Simulation results – haemodynamic metrics

Surface streamline was generated near the blood vessel lumen wall boundaries to visualize how the stent modified the flow. The Wall Shear Stress (WSS) was evaluated at the wall boundary as

$$\tau_w = \mu \frac{\partial u}{\partial r} \mid r = R \qquad (1)$$

where μ is the dynamic viscosity, u is the flow velocity along the pipe, and r is the radial distance to the centre of the pipe with a radius R.

The time averaged WSS (TAWSS) was computed by averaging the WSS over cardiac cycle,

$$TAWSS = \frac{1}{T}\int_0^T \tau_w \, dt \qquad (2)$$

where *T* is the duration of the cardiac cycle.

3.2 Animal Experiments

This method only contributed to the work presented in Chapter 6. The animal experiment mainly involved stent implantation, venography, and sonography on a cohort of eight sheep. An animal research framework was shown in Figure 3.5. Venography measured the change in the shape of the blood vessel lumen after 0, 7, 14, 21, and 28 days of stent implantation. The venograms were analysed and compared to the numerical simulations of the sheep blood vessels.

Venograms were taken from various viewing angles during each experiment for each animal. The 3D blood vessel geometry was reconstructed based on those 2D images, which were projections from different angle. The venograms enabled comparing the shape of the blood vessel lumen after stent implantation and to simulate blood flow using CFD. In addition, the change in blood flow was measured after 0, 7, 14, 21, and 28 days of implantation using an ultrasound system for clinical use. The blood flow measurements served as the boundary conditions for the CFD model. The CFD model will estimate the blood flow in the actual sheep blood vessel. The ultrasound measurements were used to validate the CFD model by comparing the flow rate at different blood vessel cross-sections.

Overall, the goal of the experiment was to analyse the blood flow pattern from the numerical simulation and change in the blood vessel lumen to observe how blood flow and tissue growth influence each other inside the stented venous blood vessel.

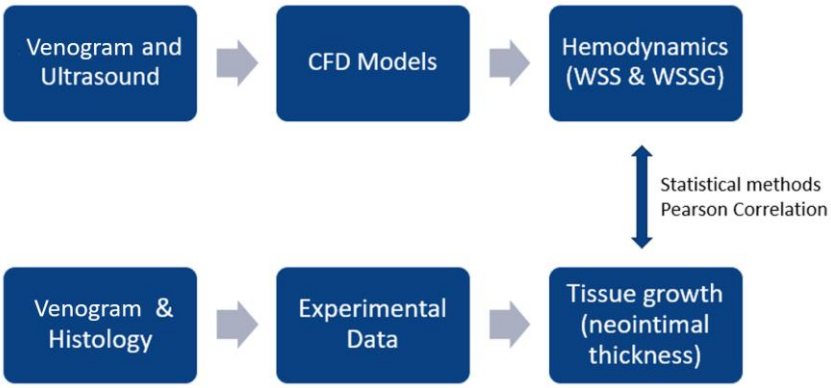

Figure 3.5 Structure of the sheep experiment

3.2.1 Experimental procedures

Blood vessels were reconstructed from venograms, which involves injecting contrast agent into the blood vessel whiles scanning. A C-arm X-ray machine was used to capture the blood vessel wall and lumen boundaries. To keep track of the change in shape of the blood vessel and evaluate lumen narrowing, venography was performed before stent implantation as control, immediately after implantation, then once a week until Day 28 (Day 0 before stent, Day 0 after stent, Day 7, Day 14, Day 21, and Day 28). Blood pressure was not measured during the venography.

Local anaesthesia was administered to alleviate procedure-related pain, while general anaesthesia was used to induce unconsciousness and unawareness of procedures. Various imaging modalities were employed to visualize jugular vein anatomy for surgical planning and assessment of blood flow through implanted vessels. A mobile x-ray C-arm was used to capture images of the blood vessel lumen boundaries and stent device integrity, which could be done with the animal under

anaesthesia. The venography, conducted under anaesthesia, involved placing catheters into blood vessels and administering a radio-opaque marker for x-ray imaging. It provided a clear picture of jugular blood vessels and their changes. To place the endovascular stent, using the venography map, concentric catheters were guided to the target region, where the venous stent was deployed through the catheter into the blood vessel. This procedure was performed on anaesthetized animals, with device fixation and wound closure in animals recovering from anaesthesia. In addition, Ultrasound was also performed on the jugular vein using an ultrasound probe, with conductive gel applied to the skin. This procedure was performed with the animal under anaesthesia. At the experiment's end, animals were euthanized, and tissue was harvested for further evaluation of tissue growth in the stented veins.

3.2.2 Geometry reconstruction

The workflow for geometry reconstruction is illustrated in Figure 3.6. Venograms were collected with the C-arm X-ray machine operating from different angles. MATLAB was then used to extract the centreline and blood vessel wall from the venograms. Using venograms from multiple views, the blood vessel centrelines were back-projected to the 3D space. After generating the 3D centreline, the blood vessel wall boundaries were mapped around the 3D blood vessel centrelines to form the actual shape of the blood vessel. The 3D points of the blood vessel were imported to COMSOL to generate the surface and volume of the actual blood vessel. Geometry validation was performed using the blood vessels extracted on Day 28 after the experiment.

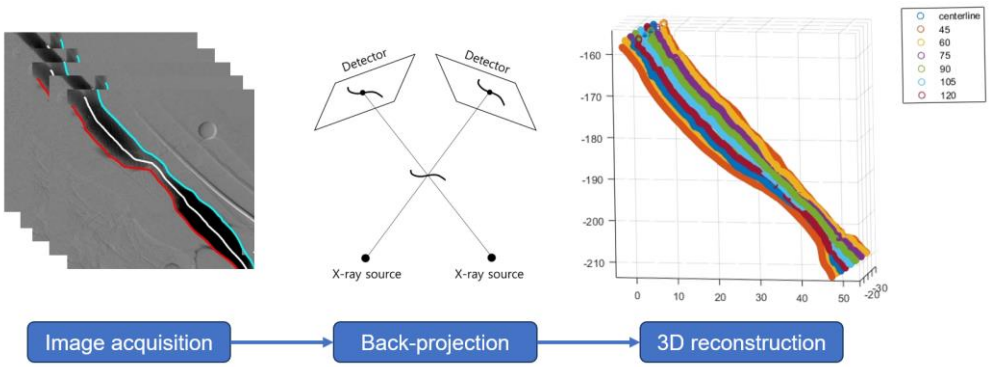

Figure 3.6 The workflow of blood vessel 3D reconstruction. The same blood vessel was scanned at multiple angles and a back-projection algorithm was performed to generate a 3D blood vessel.

3.2.3 Validation

Validation is the assessment of the accuracy of a computational model and demonstrate the creditability of simulation. Validation of a computational model consists of geometry validation and result validation. The geometry validation ensures that the simulated blood vessel is a close estimate of the actual blood vessel. In Chapter 6, the geometries reconstructed from the venograms were compared with the geometries reconstructed from micro-CT scanning. The shape and the cross-sectional area were compared. Results were described in Chapter 6. Figure 3.7 shows one example that quantitatively compares lumen areas between a computational model from COMSOL and actual area from micro-CT scans of the actual blood vessel. Results show that the area along the length of the blood vessel has been captured and errors were within 5% for most of the cross-sections. A Pearson correlation analysis was conducted to demonstrate the similarities between

COMSOL and micro-CT geometries. Besides, the shape of the blood vessels was compared between the two methods. Sheep No.2 was used as an example due to its distinctive tissue growth pattern. The shape comparison at different views shows that the COMSOL geometry is a close estimate of the actual shape of the blood vessel. In addition, validation of results was achieved through comparison between the simulated blood flow velocity and the actual blood flow velocity measured using Doppler ultrasound. The time-dependent average velocity waveform was collected from the outlet of the stent using Doppler Ultrasound, which measures blood flow over multiple cardiac cycles on different days of experiment. The velocity data was exported from the Ultrasound system and compared to the simulation, where average velocity was computed over one cardiac cycle. The results were reported in Chapter 6.

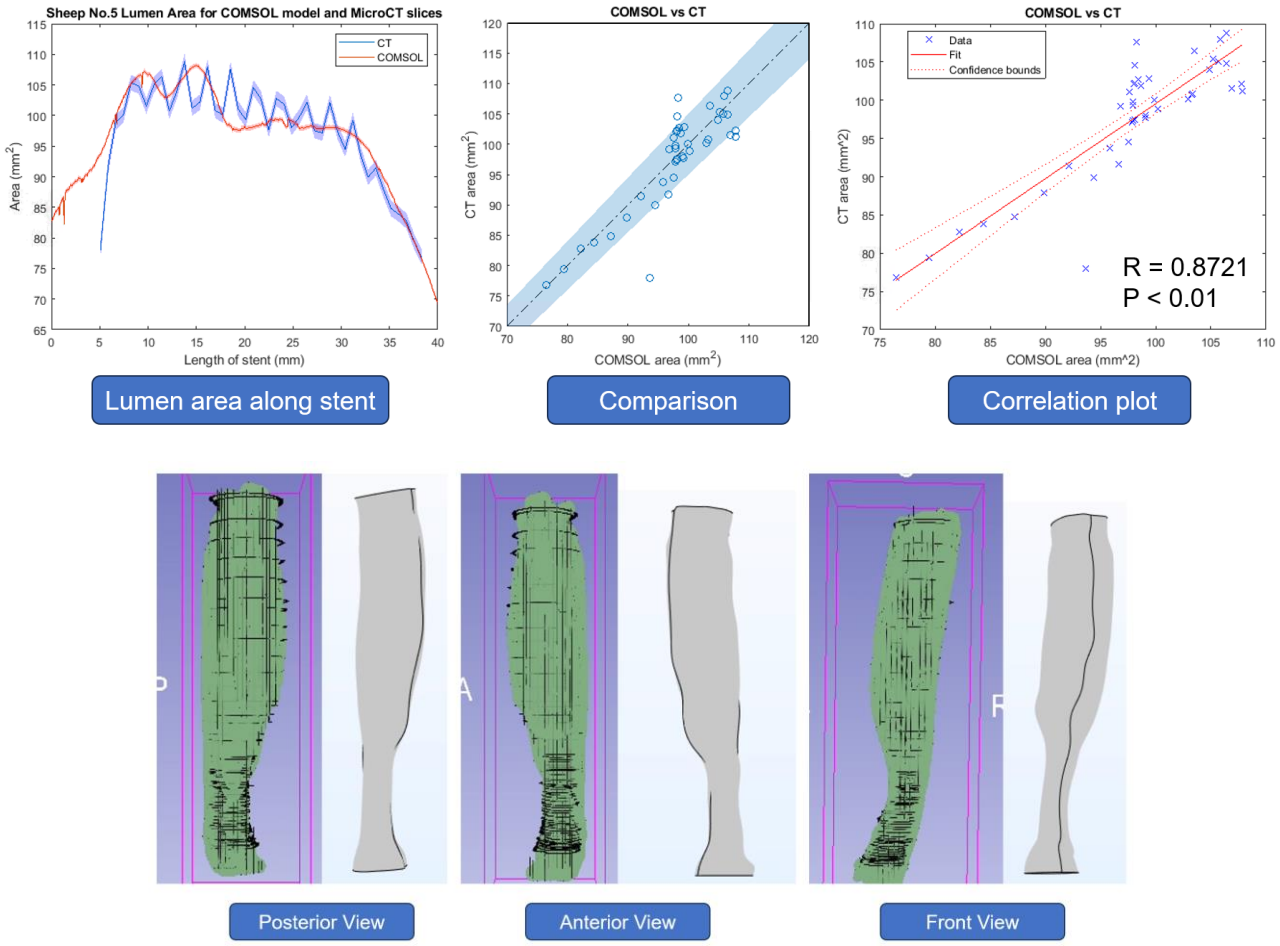

Figure 3.7 Geometry validation. Top row shows the lumen area comparisons between COMSOL and micro-CT. The bottom row shows the shape comparisons between the two methods.

Chapter 4 – Haemodynamics of Stent-Mounted Neural Interfaces in Human and Sheep Venous Sinuses

Chapter 4.2-4.5 have been published on 2023/7/24:

Qi, W., Ooi, A., Grayden, D., & John, S. (2023). Computational fluid dynamics of stent-mounted neural interfaces in an idealized cerebral venous sinus. *Proceedings of the Annual International Conference of the IEEE Engineering in Medicine and Biology Society, 2023*, 1-4. https://doi.org/10.1109/EMBC40787.2023.10341099

4.1 Aims of study and novelty.

Hemodynamic changes in stented blood vessels play a critical role in stent-associated complications. Most of the work on the haemodynamics of stented blood vessels has focused on coronary arteries but not cerebral venous sinuses. With the emergence of endovascular electrophysiology, there is a growing interest in stenting cerebral blood vessels. This chapter aims to investigate the key design characteristics of a stent-electrode array impacting blood flow in human and sheep veins. The first half explores critical stent-electrode design aspects (electrode sizes, quantity, positions) and their effects on blood flow patterns, assessing limitations and trade-offs between device performance and blood flow impact. The latter half examines blood flow in an idealized sheep vein, drawing on past experiments to understand tissue growth patterns using blood flow simulation results. These studies address crucial gaps in venous stenting literature, particularly in fluid dynamics modelling for endovascular neural interfaces because the impact of adding multiple electrodes to a stent on blood flow and tissue growth remains unknown with no supporting simulation and clinical data. Results suggest that blood flow is more influenced by the anatomy than by the presence of stent struts and electrodes, given the device's miniaturized size. The study also suggests a correlation between tissue growth in sheep and blood flow patterns. This is an early exploration of the haemodynamics of a stent-mounted neural interface. Future work will shed light on the key factors that influence blood flow and stenting outcomes.

4.2 Haemodynamics of Stent-Mounted Neural Interfaces in Human Sinuses

The stent-mounted neural interface is a device that can be deployed into cerebral blood vessels, such as the superior sagittal sinus (SSS), to acquire neuronal signals with minimally invasive surgery (Opie et al., 2018). The captured signals can be transformed into commands for controlling assistive devices, which hold promise to facilitate volitional control for patients with paralysis. However, the influence of placing a stent-mounted neural interface on the cerebral blood vessel required further study. Neointimal growth was observed on the device after 190 days of implantation, leading to a reduction of the blood vessel lumen in their sheep models (Opie et al., 2017). Although there was no report of vessel occlusion with the device, the pattern of blood vessel narrowing could not be explained. Due to limited clinical data, the impact of stent placement in the cerebral blood vessel is not clear and requires further investigation.

Literature in coronary stenting suggests that blood flow, or haemodynamics, plays a critical role in vascular tissue growth and blood vessel narrowing (Chen et al., 2017). Normally, blood flow exerts

shear stress to the blood vessel wall, maintaining an inactive state of the endothelial cells (Rajendran et al., 2013). With a stent implanted, the blood flow and mechanical environment are altered, causing lower Wall Shear Stress (WSS) around the stent strut, which disturbs the endothelial functions chronically (Campolo et al., 2014). Abnormal flow conditions will make the implanted blood vessel more vulnerable to neointimal overgrowth, which has been associated with stent-related complications, such as stenosis and thrombosis. Therefore, studying the blood flow through the stent has become vital to understand device impact and complications.

Computational Fluid Dynamics (CFD) is one of the most common approaches to study blood flow (Acuna et al., 2018). Extensive studies have demonstrated the versatility of CFD in describing blood flow and predicting stenosis for coronary artery stents (He et al., 2020) and venous stents (Liu et al., 2019). However, there is only a limited number of CFD models on stented cerebral venous sinus, which has motivated the present CFD study and discussions on the potential hemodynamic impact of stent on the venous sinus. This paper utilized CFD modelling to examine the blood flow through several stent models with various electrode designs.

4.3 Results

4.3.1 Flow streamline

Figure 4.2 illustrates the streamline near the surface of the blood vessel lumen (left). The flow streamlines are similar for all the cases. The flow was smooth and straight on the blood vessel wall. However, around the edges of the stent, the flow direction was altered to follow the shape of the stent strut and the electrode. In addition, a velocity vector plot was also generated at the corner of the strut and the blood vessel wall (right), where a circulation zone was found proximal to the strut. Although not shown, a recirculation zone was also found distal to the strut. Streamline patterns were similar for all cases with electrodes.

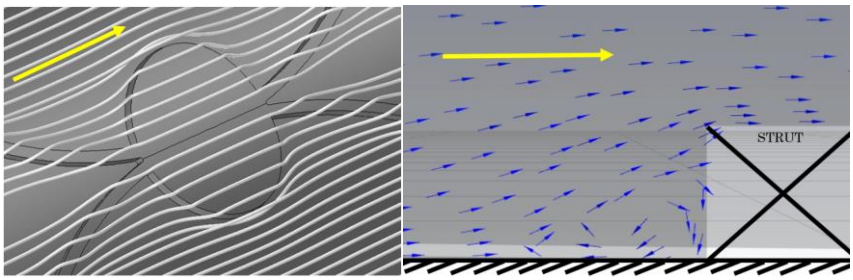

Figure 4.2 Left: Surface streamline near the electrode with a diameter of 1000 µm and a thickness of 50µm. Right: Vector plot around the stent strut showing recirculation zones before the forward-facing step. Yellow arrows indicate the blood flow direction. (More figures available in the Appendix of the thesis)

The maximum shear rate was computed at the highest flow velocity. As shown in Figure 4.3, the regions with high shear rate were identified on both symmetric (sagittal) and cross-sectional planes. A maximum shear rate of 700 s^{-1} was found in regions near the stent strut (Left) and around the edges of the electrode (Right), implying that under venous flow, the stent might not induce a high shear rate to activate clot formation in the blood vessel (Boghosian et al., 2018).

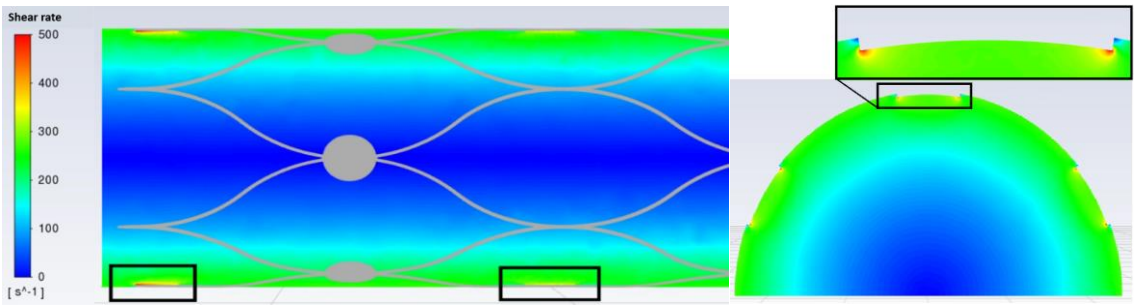

Figure 4.3 Left: Shear rate contour on a symmetric plane with stent mesh. Right: Shear rate contour on a cross-sectional plane. High shear rate regions are highlighted by black boxes.

4.3.2 Wall shear stress

The time averaged WSS over one cardiac cycle was examined. The time averaged WSS (TAWSS) was a critical indicator of normal cell function on the blood vessel wall. It was calculated by averaging the tangential WSS over the cardiac cycle. The left panel in Fig 4.4 shows the overall distribution of TAWSS. Most of the regions shown in orange had TAWSS between 0.5-0.7 Pa. In the right panel in Figure 4.4, the TAWSS was reduced as the flow approached stent strut and electrode, with a TAWSS between 0.1-0.5 Pa, shown in green. A significantly low TAWSS was observed at the corner of the stent struts and regions to the left and right of the electrode, with a value below 0.1 Pa. The values 0.1 Pa and 0.5 Pa are typical values to indicate abnormal WSS for vein and artery, respectively (Boghosian et al., 2018; Gijsen et al., 2019)

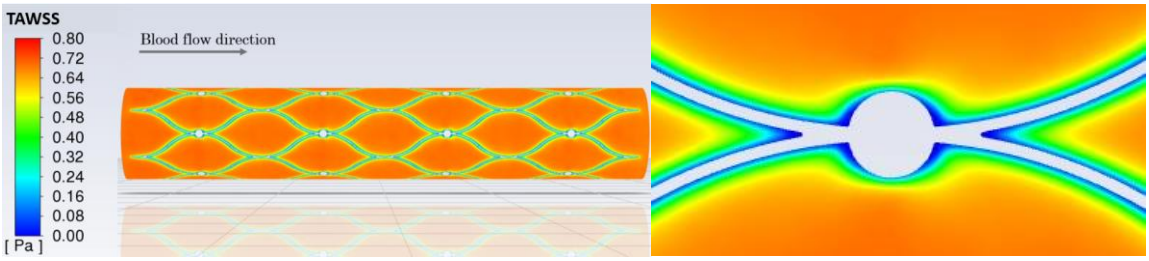

Figure 4.4 Left: Contour plot of TAWSS at the blood vessel wall boundary for the case D = 500µm. Right: Zoomed in contour plot showing the detailed TAWSS distribution around the electrode.

4.3.3 Electrode designs and wall shear stress

Cases 1, 2, 3, 7, and 8 had 24 electrodes with different electrode sizes to investigate the relationship between electrode sizes and extremely low TAWSS. In Figure 4.5 Left, there was a linear relationship between the affected area and electrode size. However, the difference between case 1 and case 8 was small (<1.5 mm^2) compared to the total stented area, which was approximately 300 mm^2 in the model. This indicated that using 24 electrodes with 2000 µm would not elevate the area subject to low WSS for the model. The extremely low WSS was primarily induced by the stent strut instead of the 24-disc electrodes.

In Figure 4.5 Right, results from cases 4, 6, and 7 showed a linear relationship between the number of electrodes used in stent and the area of extremely low TAWSS observed on the wall boundary.

For every 10 electrodes added to the stent, the AELWSS increased by approximately 0.1%, which was negligible compared to the percentage of AELWSS observed from the stent without any electrode.

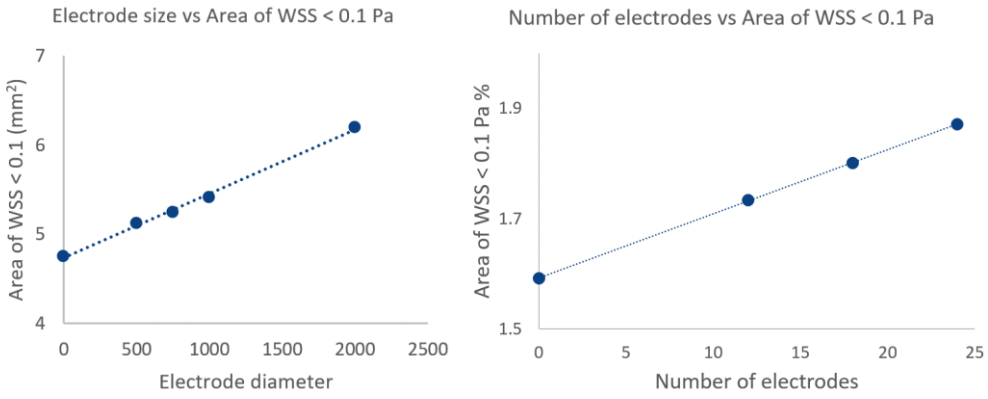

Figure 4.5 Left: The area of low WSS plotted against the diameter of electrode in the model. Right: The area of low WSS for different number of electrodes.

The models in cases 4 and 5 had different electrode patterns. The area subject to a WSS less than 0.1 Pa was measured every 0.1 s during the cardiac cycle to compare the difference between parallel and alternating electrode arrangements. The AELWSS versus time was plotted on the same graph shown in Figure 4.6, where the two sets of data points overlapped and showed no difference. This suggested that the alternating arrangement of electrodes on the stent device did not affect the WSS.

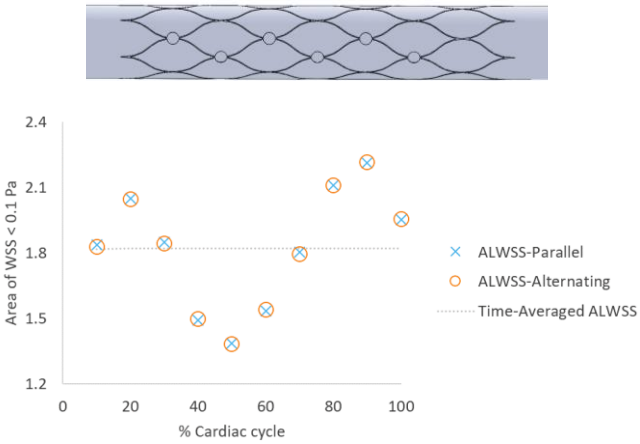

Figure 4.6 Top: The stented sinus model where the electrodes in the stent were in an alternating pattern. Bottom: The area of very low WSS collected every 0.1 s during the cardiac cycle.

4.4 Discussions

In this study, a CFD model of the stent in an idealized cerebral venous sinus was constructed and blood flow was simulated. Hemodynamic variables, including the flow streamlines, shear rate, and WSS were visualized to evaluate the effects of stent strut and electrodes on the venous flow. In addition, the hemodynamic effect of stent was analysed by varying the size, quantity, and arrangement of electrodes on the stent. Compared with CFD modelling of a traditional stent, the

stent introduced a new design feature to the stent by adding disc electrodes, which has not been studied previously. Hence, this early study aims to generate insights for future CFD modelling of stent-mounted electrode arrays.

4.4.1 Blood flow altered at the stent strut edges and corners.

The blood flow was altered by the stent, causing recirculation zones (Figure 4.2) and low shear rate zones (Figure 4.3) around the stent strut and electrode. Those results suggested the potential locations for particle accumulation. Recirculation zones tend to trap substances, including platelets and coagulation factors in the bloodstream, and foster platelet accumulation over time, elevating the risk of delayed vascular repair and thrombosis (Jiménez & Davies, 2009). The risk of thrombosis was higher along the struts and electrodes. This implies that the stent strut design needs improvement, such as a smooth or flat strut shape that can reduce circulation pattern or material coatings that minimizes thrombus formation. Future studies that involve stents with different strut cross-sections and material coatings, are necessary to determine the optimal stent design to reduce flow recirculation and thrombogenicity.

In addition, the stent strut and electrodes also induced a low WSS region due to the flow recirculation (Figure 4.4). A WSS lower than the minimum WSS found in veins (Boghosian et al., 2018) was observed near the struts and electrodes (Figure 4.4). The low shear stress on the blood vessel wall can result in endothelial dysfunctions and induces blood vessel tissue overgrowth over time (Roux et al., 2020). For the stent, there might be more tissue growth in the low WSS regions than regions with a normal WSS. However, animal experiments that examine *in-vivo* endothelial tissue growth post-implantation, are required to draw any conclusion about endothelial growth.

4.4.2 Disc electrodes have minimal effect on blood flow.

The design characteristics of electrodes are critical since they determine the performance of stent-mounted neural interface. For instance, the number of electrodes influences the signal quality of the recorded brain signal, and the size of the electrode determines the maximum current injection during brain stimulation (Wodlinger et al., 2011). With an increased number and size of electrodes, the device performance improves, yet more neointimal growth may occur. Thus, the effect of electrode size on the hemodynamic variables became an important research question. In this study, the area subject to a low WSS increased linearly with the electrode size and number of electrodes (Figure 4.5). Nevertheless, only a slight difference was observed between cases without any electrodes and the cases with the largest electrode, implying that the abnormal WSS induced by the electrodes were negligible compared to the WSS affected by the stent strut. A larger electrode would not impose a larger area of abnormal WSS compared with the small electrodes. This may suggest that adding electrodes does not influence the blood flow in the stented segment. However, in this study electrode size was limited to 1000 microns otherwise there might be an elevated risk of electrode detaching from the stent. However, other factors, such as foreign response to electrode material, could be considered in future testing to understand the impact of adding electrodes to a stent on tissue growth.

4.5 Future perspectives

The stent-mounted neural interface has opened a less invasive alternative for accessing deep brain regions that were inaccessible previously. This may enable novel methods for the diagnosis and treatments of neurological diseases, such as Parkinson's disease and epilepsy (John et al., 2019). In addition, the device can be used as a neural prosthesis to control digital devices, which will improve the quality of life for disabled patients (Oxley et al., 2020). However, further study is required to fully understand the impact of the device on the implanted cerebral blood vessels. The CFD model suggested that stent-mounted neural interfaces can disturb blood flow and induce low-shear regions in the stented blood vessels. There is a potential that tissue proliferation will occur around the stent struts and influence the blood flow even more. The tissue growth can gradually develop, which was observed in sheep models (Opie et al., 2017). Despite tissue growth, endovascular neuromodulation still has a lower risk of complication than conventional cortical electrode arrays and has great potential to dramatically improve patient outcomes. For the further development of stent electrode, it is essential to ensure that the potential stent complications are mitigated by using optimal stent designs. Hence, more research, including modelling, experimental work, and clinical research, should be conducted to determine the key design characteristics for intracranial stents. The current study has provided a basic framework and workflow for a CFD model of the stent-mounted neural interface, which can be expanded to study other potential target blood vessels for neuromodulation, including the human cerebral arteries and internal cerebral veins (Neudorfer et al., 2020). Any realistic features of a cerebral blood vessel, including curvature, vessel tapering, and material properties of the blood vessel wall, should be considered in future works.

Chapter 4.6-4.8 were the original work where the computational results contributed to a journal paper published by *Journal of Neural Engineering* on 2022/10/28:

> John, S. E., Donegan, S., Scordas, T. C., Qi, W., Sharma, P., Liyanage, K., Wilson, S., Birchall, I., Ooi, A., Oxley, T. J., May, C. N., Grayden, D. B., & Opie, N. L. (2022). Vascular remodeling in sheep implanted with endovascular neural interface. *Journal of neural engineering*, *19*(5), 10.1088/1741-2552/ac9a77

4.6 – Haemodynamics of Stent-Mounted Neural Interfaces in Sheep Sinuses

4.6.1 Three-dimensional sinus and stent models

The ovine superior sagittal sinus (SSS) is based on data from previous studies (Opie et al., 2018; Oxley et al., 2018). Anatomical features of the ovine SSS, including lumen diameters and the radius of curvature, were extracted from digitized animal data (Figure 4.7). The SSS was idealized as a curved circular pipe with a diameter of 2 mm at the flow outlet (**). It tapers towards the inlet (*) with a diameter of 1.3 mm. The tapering was assumed to be linear. The curvature of the SSS was estimated to be 30 mm using centreline data from the cerebral venography. The blood vessel wall of the SSS was assumed to be smooth and rigid.

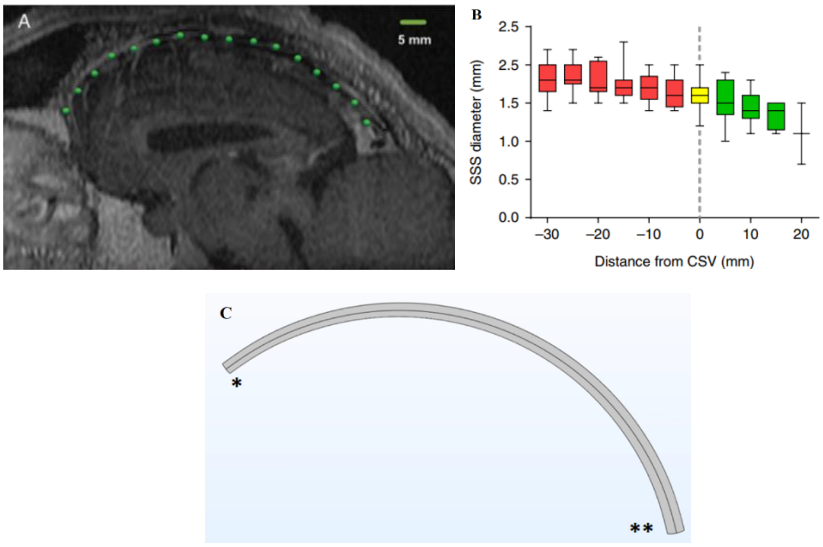

Figure 4.7 A) The SSS venography with fiducial points (green dots) along the course of the superior sagittal sinus. The radius of curvature was computed using the fiducial points. B) Boxplot of the diameter of superior sagittal sinus. C) The idealized sheep blood vessel with * indicating inlet and ** indicating outlet. Figure A and B were adapted from Oxley et al., 2018.

The computational modelling software COMSOL Multiphysics™ was used to create the stent model (Figure 4.8). The size of the device was adopted from the actual device used in the experiment. The stent has an oversizing parameter of 4 mm to facilitate stent apposition onto the blood vessel wall and to prevent device migration. Since the cerebral venous sinus is deformable with a lumen diameter of 1-2 mm, the expansion of the stent after implantation could have slightly increased the lumen diameter in the local stented region after implantation. The resulting stent expansion ratio was around 1.1, which agrees with general stenting practices (Yamaguchi et al., 2006; Zhao et al., 2009).

Virtual implantation was used to create the stented segment of the ovine SSS model. The diameter of the stented region was assumed to be constant 2 mm to approximate the increased blood vessel lumen due to stent expansion. The flow domain was created by subtracting the volume of the stent model from the blood vessel model using Boolean operation (Figure 4.8). The position of the stent model implantation site was close to the actual location of stent in the sheep brain.

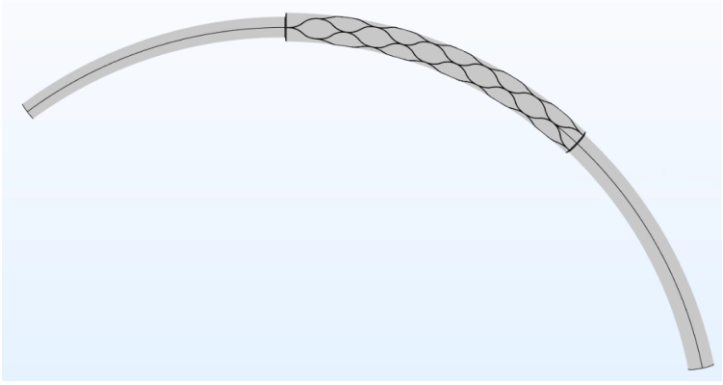

Figure 4.8 An idealized model of the ovine SSS implanted with the stent-electrode array.

The finalized stented blood vessel model was then meshed in COMSOL. The average number of tetrahedral elements used in the flow domain was 1 million tetrahedral elements with 6 boundary layers. The geometry was smoothed at sharp corners with a fillet size of 10 microns to achieve a better mesh quality. The elements around the stent strut were divided into finer mesh with a minimal size of 10 microns to depict the stent strut details. A mesh convergence analysis was done to ensure that the simulation results did not vary with increasing the number of mesh cells.

4.6.2 Computational fluid dynamics

Simulations were conducted in COMSOL by solving the Navier-Stokes equations for incompressible viscous flow, where the venous blood flow was assumed to be laminar. Blood was assumed to have a density (ρ) of 1060 (kg/m^3) with a shear-thinning dynamic viscosity (μ) based on the non-Newtonian Carreau model in the literature (Tabakova et al., 2014). A steady venous flow rate of the ovine SSS from the literature was applied as the boundary condition for the computational model (Upton et al., 1994). The mean flow velocity was set to be 0.52m/s. The model inlet was extended for the flow to be fully developed.

4.6.3 Hemodynamic metrics (WSS and WSSG)

This study implemented several fundamental metrics to study the blood flow pattern with the stent. Surface streamline was generated near the blood vessel lumen wall boundaries to visualize how the stent-electrode modified the flow. Wall shear stress (WSS), which describes the tangential force per unit area acting on the blood vessel wall, is an important parameter associating the haemodynamics with endothelial growth (Gijsen et al., 2019). The shear stress was evaluated at the wall boundary as

$$\tau_w = \mu \frac{\partial u}{\partial r} \mid r = R, \qquad (3)$$

where μ is the dynamic viscosity, u is the flow velocity along the pipe, and r is the radial distance to the centre of the pipe with a radius of R.

The wall shear stress gradient (WSSG) was the magnitude of the spatially varying wall shear stress and was defined as

$$WSSG = \sqrt{\left(\frac{\partial \tau_w}{\partial x}\right)^2 + \left(\frac{\partial \tau_w}{\partial y}\right)^2 + \left(\frac{\partial \tau_w}{\partial z}\right)^2}. \qquad (4)$$

The WSSG measured the spatial change of WSS along the blood vessel, where a high WSSG indicated a rapid change of the WSS. A high WSSG has been associated with endothelial cell migration, increased vessel wall permeability, and profound cell division (DePaola et al., 1992; Phelps & DePaola, 2000; Tardy et al., 1997).

4.6.4 Data correlation analysis

The WSS and WSSG were processed and compared against the mean tissue growth data from the sheep experiment. WSS and WSSG were averaged first to compare with the average tissue thickness calculated from the histological image slices. In the computational model, a series of cross-sections were defined along the centreline of the blood vessel. The WSS and WSSG values on the

circumference were summed and normalized to obtain the average circumferential WSS and WSSG at different locations or lengths of the blood vessel. The tissue growth data was collected from four animals using high-resolution micro-CT imaging. Stent-associated tissue thickness was measured based on CT image slices. Pearson's correlation was used to quantify the association between the mean tissue thickness and hemodynamic variables. Correlation was classified as weak (0.1 – 0.3), moderate (0.31 – 0.6), and strong (0.61 – 1.0).

4.7 Result

Figure 4.9 shows the wall shear stress contour (middle) and the streamline results. The WSS was non-uniform in the stented region compared to the uniform WSS in the unstented segments. A low WSS (less than 1.5 Pa) was found near the proximal end of the stented segment (blue). Along the outer bend, a high WSS (greater than 4 Pa) was observed along the curve, while along the inner curve, the WSS gradually recovered from 0.5 Pa to 3 Pa downstream. The unstented region had a uniform WSS distribution. Streamlines were plotted near both ends of the stented regions, where blood entered and left the expansion zone. The streamline on the left indicated uneven circulations near the proximal end (identified by the two red circles). The circulation zone at the inner bending is longer than the outer bend, which corresponds to regions with low WSS. No circulation was observed from streamlines near the exit of the stented region (right).

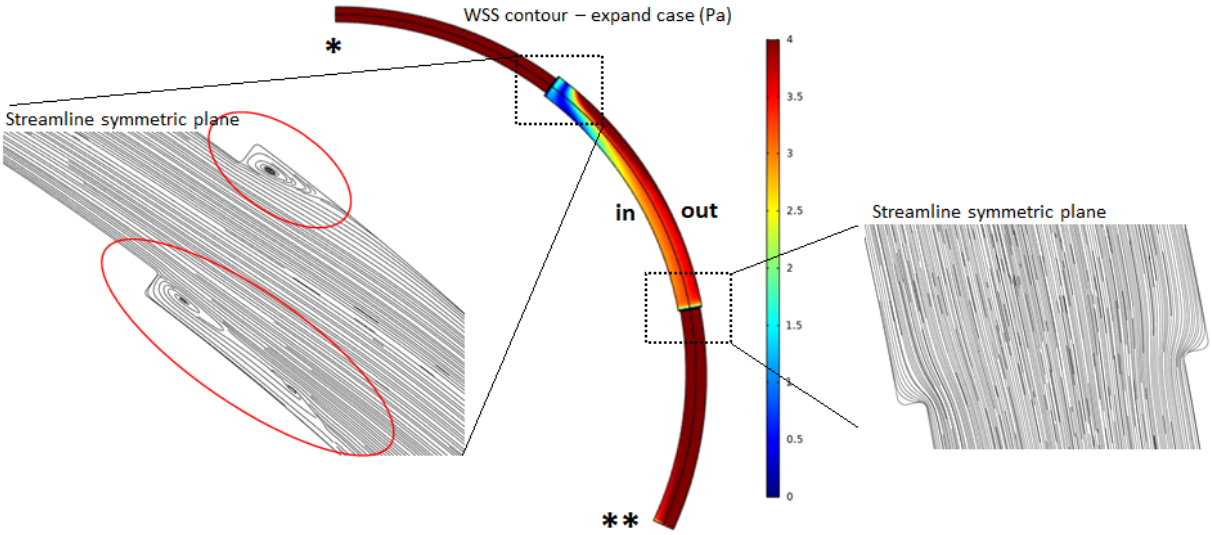

Figure 4.9 Wall shear stress contour of the sheep's superior sagittal sinus (middle) accompanied by streamlines of both ends of the stented region. Uneven circulation zones were observed at inner and outer curves (circled).

Figure 4.10 shows the hemodynamic variables and the amount of stent-associated tissue thickness (extracellular matrix) along the length of stent-electrode array in the SSS. The key hemodynamic variables include the WSS and WSSG, which were extracted from a series of cut slices in the computational model and averaged over the circumference.

Figure 4.10 A1 shows the mean WSS and tissue thickness along the length of the stent-electrode array plotted separately. The WSS shows a rapidly decreasing trend near the distal end (30 mm).

Figure 4.10 A2 shows the correlation scatter plot between the WSS and tissue thickness. The Pearson's coefficient of -0.63 shows a strong negative correlation.

Figure 4.10 B1-B2 shows the mean WSSG and tissue thickness along the length and their correlation. The WSSG rises as the length increases, which follows a similar trend as the tissue thickness along the length of stent-electrode array. Pearson's correlation was 0.77, indicating a strong positive correlation between WSSG and tissue thickness.

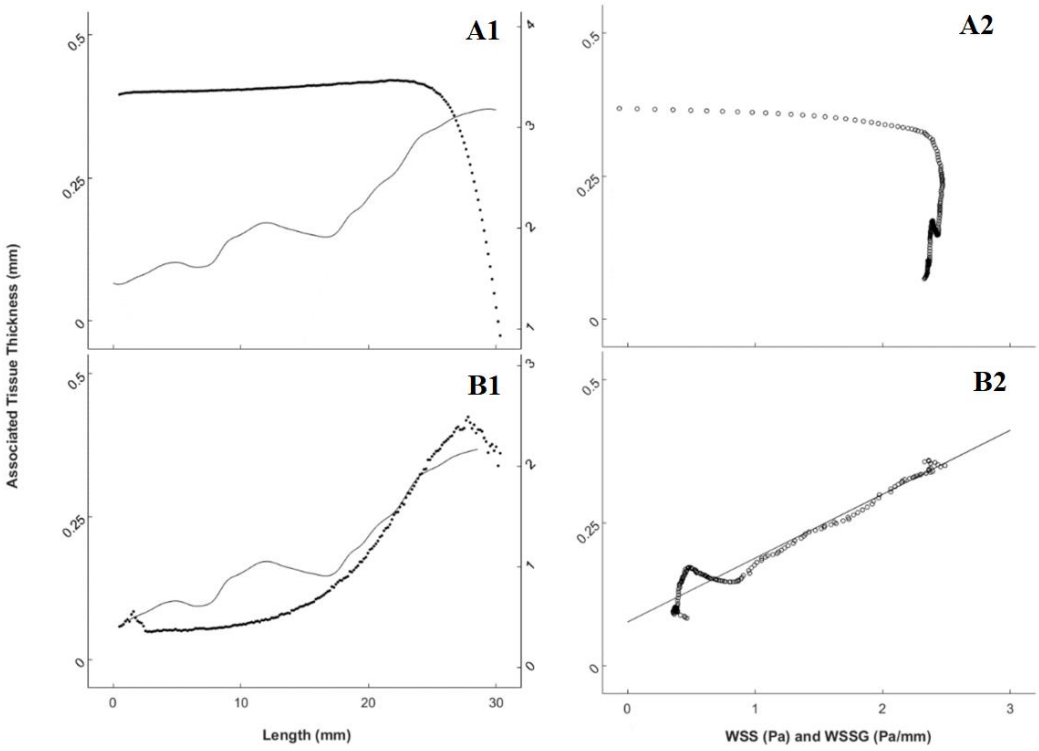

Figure 4.10 A1&B1: Line plot of the mean wall shear stress and tissue thickness along the length of the stented blood vessel. The WSS is expressed in Pa, and the tissue thickness is expressed in mm. A2&B2: Scatter plot of the tissue thickness (mm) versus the wall shear stress (Pa).

4.8 Discussion

Previous studies have reported the roles of WSS in coronary arteries (Gijsen et al., 2019; LaDisa et al., 2005). The WSS modulates the gene expression and function of the endothelial cells (Passerini et al., 2003), and a low WSS has been associated with tissue thickening and inflammation following vessel injury due to stent implantation (Kwak et al., 2014). However, the correlations between the WSS, WSSG, and neointimal growth in a venous sinus stent have not been explored previously. The current computational model provides preliminary findings of the hemodynamic influence in the stented SSS. The simulation result indicates that the caudal end of the stented SSS will experience a low WSS and a high WSSG after the deployment of the stent, implying that more neointimal thickening will occur at the caudal end (inlet). The prediction agrees with the tissue thickness data from the experiment.

Data analysis suggests that the WSS pattern after implantation did not match the chronic tissue thickness. In Figure 4.10 A1, neointimal tissue was present at the rostral end of the SSS, where the WSS was constant. The mismatch between WSS and tissue growth may result from the current CFD

model only estimating the WSS pattern in an acute stage after implantation. Neointimal growth is a time-dependent process that will gradually alter the geometry and haemodynamics of SSS, which may change the ongoing neointimal growth pattern (Donadoni et al., 2017). The change was observed in a study where the tissue growth gradually restored the WSS to the physiological level (Roux et al., 2020). To better predict the tissue response of stent-electrode array, which is relevant to its clinical outcome, the CFD model should be further developed to capture the development of haemodynamics over time.

Data analysis also revealed a strong correlation between WSSG and stent-associated tissue thickness, which has not been shown before. An animal study of the rabbit iliac artery has not found any strong association between tissue growth and the WSSG between 14 and 21 days (LaDisa et al., 2005). In-vitro studies of cellular response to WSSG have shown that endothelial cells tend to migrate away from the high WSSG region and colonize downstream (DePaola et al., 1992). Interestingly, the result suggests that tissue thickness increases with the WSSG. The WSSG has played a role in tissue response in the blood vessel, but further study will be required to validate the observed correlation with a more rigorous examination and investigate the influence of WSSG in the cerebral venous system.

4.9 Chapter summary

In this chapter, the impact of stent-mounted neural interfaces was examined in idealized human and sheep blood vessels. This study is the first attempt to evaluate the hemodynamic impact of endovascular neural interfaces, a topic previously absent from the literature. Simulations were conducted for various neural interface designs across different blood vessels and flow conditions. Despite differences in blood vessel geometry, regions of flow recirculation and low wall shear stress (WSS) were identified around the edges of the stent, with the affected area increasing linearly with the number and size of electrodes. Additionally, an alternating arrangement of electrodes did not change the total affected area compared to a parallel arrangement. Using previous experimental data on tissue growth in sheep, it was found that low WSS may promote tissue growth in the venous wall, whereas a rapid increase in WSS (high WSS gradient) may have a strongly positive impact on tissue growth. The computational models established in this study, along with the key findings, address a significant gap in the literature on venous stents and endovascular neural interfaces. However, the current study is limited by the availability of relevant experimental data and the use of simplified blood vessel geometries. Further research, including the development of more realistic models, is required to evaluate the chronic effects of stent-based devices.

Chapter 5 – Haemodynamics of Stent-Mounted Neural Interfaces in Tapered and Deformed Blood Vessels

Chapter 5 has been published by *Scientific Reports* on 2024/3/27:

Qi, W., Ooi, A., Grayden, D. B., Opie, N. L., & John, S. E. (2024). Haemodynamics of stent-mounted neural interfaces in tapered and deformed blood vessels. *Scientific reports*, *14*(1), 7212. https://doi.org/10.1038/s41598-024-57460-w

5.1 Aims of study and novelty.

The stent-mounted neural interface enables minimally invasive alternative to invasively record and stimulate the brain. Yet, vascular stents influence the flow of blood (haemodynamics), resulting in neointimal overgrowth within the blood vessel lumen. The stent elements, including electrodes and stent struts, and blood vessel wall geometry, can impact the biomechanics of the blood vessel. This could potentially cause undesired vascular remodelling post-stenting. While there is an increasing application of stents and stent-like neural interfaces in venous blood vessels in the brain, it becomes essential to comprehend how those venous stents influence blood flow and subsequent tissue growth in veins.

This chapter aims to investigate the relationship between blood vessel wall biomechanics and tissue growth following implantation of a neural interface in the brain. This is crucial and novel as the factors contributing to tissue growth in venous stents are not well understood. Veins differ from arteries in terms of anatomical structures, blood flow characteristics, and optimal stent designs. The literature on venous stenting lacks computational simulations addressing venous blood flow and venous neointimal tissue growth in venous sinus stents. The interaction between venous stents and the venous blood vessel wall, as well as the factors influencing venous haemodynamics, remains unclear. The expanding use of stent technology highlights the need for a better understanding of stent-related complications, such as neointimal hyperplasia, to enhance treatment outcomes for patients receiving neural interfaces.

Additionally, the chapter examines the impact of stent size selection on blood vessel deformation and blood flow post-implantation. The results suggest that venous wall deformation may significantly contribute to changes in venous blood flow. This highlights the importance of considering venous deformation in mechanical simulations, which can provide more accurate estimates than computational fluid dynamics (CFD) analyses on rigid cylindrical blood vessels.

The chapter also aims to provide simulations and tissue response profiles in cortical veins. The chapter shows key differences between venous and arterial stent haemodynamics. Arteries, due to their greater stiffness, experience minimal lumen deformation and are highly influenced by the presence of stent struts. In contrast, veins, being more compliant, undergo significant lumen deformation and are less affected by the presence of the thin stent struts of the venous sinus stent.

The research is novel and different from literature in arterial stent hemodynamics. The different targeted blood vessels result in different boundary conditions. The ranges of Wall Shear Stress and Wall Shear Stress gradient on the venous wall are much lower due to over-expansion and slow non-pulsatile blood flow conditions. Furthermore, the complex tissue growth patterns observed in veins

were distinct from those seen in diseased arteries affected by atherosclerosis. Overall, the chapter creates impact by providing valuable insights, guidance, and simulation tools for future research in evaluating stent-electrode designs under normal venous flow conditions in healthy veins. To date, there are no studies showing tissue growth patterns and CFD of healthy veins.

5.2 Introduction

Venous sinus stenting is a conventional intervention that aims to improve hypertension-related narrowing of blood vessels within the cranial cavity. Elevated intracranial pressure exerts substantial amounts of compression on the cerebral venous system, leading to constriction of venous sinuses, including the superior sagittal sinus (SSS), transverse sinus (TS), or sigmoid sinus (SS), resulting in symptoms such as headaches and tinnitus (Daggubati & Liu, 2019). The deployment of one or multiple venous stents serves to restore blood flow and alleviate these symptoms. More recently, venous sinus stenting has gained renewed attention with the emergence of stent-electrode devices. While traditionally stenting is applied to treat stenosis, the stent-electrode array in this study functions as a neural implant. These implants are currently being considered as brain computer interfaces and for recording from and stimulating the brain and peripheral nervous system (Raza et al., 2020). The device records brain signals of paralysed patients within healthy venous sinuses near the active brain regions (Mitchell et al., 2023; Oxley et al., 2020). The utilization of venous sinus stents as conduits is increasingly favoured due to their minimally invasive nature and reduced risk compared to conventional implanted electrode arrays that have direct contact with brain tissue. With the growing interest in venous sinus stenting, there is an increasing need to understand venous stent complications, particularly neointimal hyperplasia, a facet currently absent in the literature and clinical data.

Neointimal Hyperplasia is characterised by excessive neointimal tissue growth on the innermost layer of the blood vessel wall after vascular interventions which can occur following stent implantation (Collins et al., 2012). Hyperplasia is the major cause of in-stent stenosis, characterised by a severe narrowing (greater than 50%) of the blood vessel lumen after stenting, occurring in approximately 10% of patients receiving a stent (Buccheri et al., 2016). With the rapid expansion of stent technologies, including neural interfaces using a stent scaffold, there is a compelling need to better understand venous neointimal hyperplasia within implanted blood vessels.

Haemodynamics (blood flow) plays an essential role in the development of neointimal hyperplasia (Roux, Bougaran, Dufourcq, & Couffinhal, 2020; Wang et al., 2018). Blood flow exerts mechanical stimuli, including pressure force and Wall Shear Stress (WSS), to the inner vessel wall covered by a thin layer of endothelial cells. The WSS is sensed by the endothelial cells that, in turn, react to variations in shear conditions (Roux, Bougaran, Dufourcq, & Couffinhal, 2020). A disturbance of the mechanical environment can transfer cells from an inactive (quiescent) to an active (pro-inflammatory) state, initiating and accelerating endothelial growth (Wang et al., 2018). A low shear environment (WSS < 0.5 Pa) can induce cell proliferation, while a high wall shear stress gradient (WSSG > 200 Pa/m) can induce cell accumulation downstream (Beier et al., 2016). When a stent is introduced into the blood vessel, the presence of stent struts will abruptly modify the blood flow pattern and the shear stress. There is a potential that a stent will elevate the risks of neointimal overgrowth after implantation. Therefore, studying haemodynamics in stented blood vessels is crucial to predict the risk of neointimal hyperplasia to enhance stent design and safety.

To study blood flow dynamics, extensive research (Antoniadis et al., 2015; Beier et al., 2016; Wang et al., 2018) has been conducted using Computational Fluid Dynamics (CFD). Studies have revealed that stents created stagnant or circulated flow patterns characterised by low shear stress on nearby

blood vessel walls, where greater amounts of neointimal thickening were observed (LaDisa et al., 2005). However, many CFD studies have assumed a cylindrical blood vessel lumen with minimal vessel wall deformation and tapering after stent implantation, which was found to provide inaccurate results (Martin, Murphy, & Boyle, 2014). Studies that have used deformed models found that the stent deployment ratio (stent-to-artery ratio) had a great influence on the blood flow in stented arteries, although the optimal stent deployment ratio and haemodynamics have not yet been well quantified, especially for tapered blood vessels (Shen et al., 2020).

Compared to the arterial stent literature, there have been fewer studies on venous sinus stents. Neointimal growth in venous stenting has not been previously reported in clinical studies with supporting patient data. However, in recent years, Opie et al. (2017) identified neointimal growth in sheep Superior Sagittal Sinus (SSS) over 190 days after implantation of a neural interface based on a stent-mounted electrode array with a growth pattern that varied along the length of the stented segment. Furthermore, factors that may contribute to the variable tissue growth in the venous sinus were not quantified in the previous work. Therefore, there is a need to better understand tissue growth in stented venous sinus due to growing interest in using endovascular stents in the cerebral venous sinus (John, Grayden, & Yanagisawa, 2019).

The present study used CFD to evaluate the haemodynamic impacts of a stent and an endovascular neural interface on idealised human and sheep venous sinus models. The haemodynamic impacts of deformation and blood vessel tapering were quantified using various stent-to-vein ratios for the stented blood vessel. Simulation results were compared with tissue growth data from sheep. The current work sheds light on neointimal growth after stenting in venous blood vessels in the brain. It takes the first steps towards realising customisable endovascular neural interfaces and stents to minimise vascular remodelling and the degree of blood vessel narrowing after implantation.

5.3 Methods

5.3.1 Geometry constructions

All human venous sinus and stent-based neural interface models were generated using the design module of COMSOL Multiphysics® (v. 5.6, Stockholm, Sweden). The stent model was composed of electrodes mounted on a nitinol scaffold where disc electrodes were fused, as depicted in Figure 5.1. The stent was then placed inside an idealised human venous sinus, which was represented as either a hollowed cylinder or a hollowed cone with parameters from the Superior Sagittal Sinus (Boddu et al., 2018; Oxley et al., 2016). Hollowed cones were used to represent the tapering feature of the blood vessel, which was the ratio between the diameters of the flow inlet and outlet. Five numerical cases were included in this study. Cylindrical blood vessels were constructed for Cases 1, 2, and 3, whereas conical blood vessels with various tapering ratios (b = 1:1.1 and 1:1.2) were used in Cases 4 and 5 (as summarised in Table 1).

In addition to these computational models, three idealised sheep models (Cases 6-8) were constructed as curved cones with the curvature and diameters obtained from the CT scans (John et al., 2022). The shape of the original sheep blood vessels could not be obtained from the CT scans due to uneven tissue growth and strong metal artefact. The geometries of the three stent-based neural interfaces were successfully segmented from CT scans using 3D Slicer (Fedorov et al., 2012). The 3D geometries were then smoothed with Autodesk Meshmixer (Autodesk Inc., San Rafael, CA, USA).

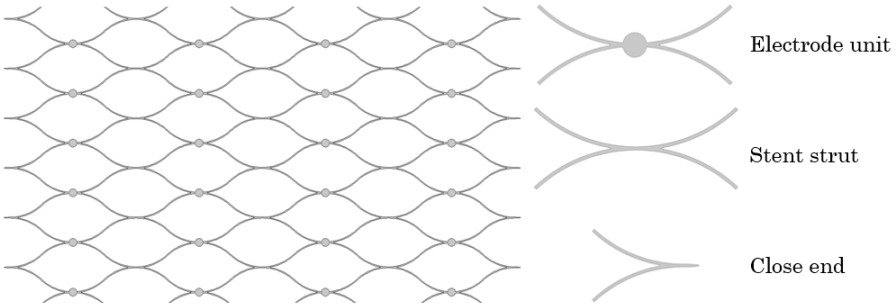

Figure 5.1 The design pattern of the stent-based neural interface. The stent had a rectangular strut profile (70 µm width and 50 µm thickness). Twenty-four electrodes (D = 500 µm) were attached to the stent struts.

Case No.	Features	Stent deployment ratio (a)	Vessel tapering ratio (b)
1	Control	1	1:1
2	Slightly deformed	1.05	1:1
3	Deformed	1.1	1:1
4	Slightly tapered	1.1	1:1.1
5	Tapered	1.1	1:1.2
6	Sheep-specific	-	-
7	Sheep-specific	-	-
8	Sheep-specific	-	-

Table 1. Summary of numerical cases with stent deployment and blood vessel tapering ratios

5.3.2 Finite Element Analysis (FEA) and Computational Fluid Dynamics (CFD) simulations

The structural mechanics module of COMSOL Multiphysics® (v. 5.6, Stockholm, Sweden) was used to simulate stent deployment in the venous sinus wall. A non-linear contact problem was solved between the self-expanding neurovascular stent-based neural interface and the venous sinus wall (Figure 5.2a), where the expansion of the stent was defined by a prescribed radial displacement on the stent strut. The stent diameter increased evenly over time along the length of the stent in the mechanical simulation. Both the inlet and outlet of the blood vessel were stationary during stent expansion. Friction and stent movements in the longitudinal direction were ignored. Material properties of venous sinus and nitinol stent were from the literature (Table 2) (Delye et al., 2006; MatWeb, 2020). Mechanical simulations were run on the Spartan supercomputer facility at the University of Melbourne. The deformed geometries (Figure 5.2b) were generated from the displacement results and exported for blood flow simulation (Figure 5.2c) at different deployment ratios (a = 1.0, 1.05, and 1.1), which was the ratio between lumen diameter after stenting to healthy lumen diameter. All stent-to-vein ratios were within the range in the literature (LaDisa et al., 2005; Martin, Murphy, & Boyle, 2014). Symmetry was used to reduce the computational cost and results were verified with a full model.

Name	Elastic modulus	Poisson's ratio	Shear modulus	Mass density	Tensile strength	Yield strength
Sinus wall	30.69E6 [Pa]	0.49	4.66E5 [Pa]	1102 [kg/m^3]	4.9E6 [Pa]	4.13E6 [Pa]
Nitinol	8E10 [Pa]	0.33	1.08E10 [Pa]	6450 [kg/m^3]	9E8 [Pa]	1E8 [Pa]

Table 2. Material properties of the venous sinus wall and nitinol stent for the mechanical simulation.

The deformed geometries (Figure 5.2d) were processed with Boolean subtraction to generate the flow domain for the stented blood vessel (Figure 5.2e), which was subsequently meshed with tetrahedral elements with a minimum element size of 0.01 mm and with four boundary layers. Using the CFD module in COMSOL Multiphysics®, a laminar flow was applied for the venous flow. The blood had a density of 1,060 kg/m^3 and shear-thinning viscosity using the non-Newtonian Carreau model (μ_0 = 0.056 Pa·s, μ_∞ = 0.0035 Pa·s, λ = 3.313 s, n = 0.3568) (Shibeshi & Collins, 2005). A fully developed flow profile was applied at the inlet of the blood vessel with a flow rate of 285 ml/min (Jordan, Pelc, & Enzmann, 1994). For the sheep blood vessel models, a different flow rate of 53 ml/min was applied based on the ultrasonic doppler method (Upton, Grant, & Ludbrook, 1994). Mesh convergence verified that the simulated WSS results did not vary with the mesh size of the model. The tangential WSS was computed using

$$\tau_w = \boldsymbol{\tau_t} - (\boldsymbol{\tau_t} \cdot \boldsymbol{n})\boldsymbol{n}, \quad (1)$$

where $\boldsymbol{\tau_t}$ is the wall traction vector calculated from the stress tensor and $\boldsymbol{n}$ is the surface normal. WSS (τ_w) below 0.5 Pa was defined as low WSS (Beier et al., 2016; LaDisa et al., 2005).
The Wall Shear Stress Gradient (WSSG) is the magnitude of the spatially varying wall shear stress and was defined as

$$WSSG = \sqrt{\left(\frac{\partial \tau_w}{\partial x}\right)^2 + \left(\frac{\partial \tau_w}{\partial y}\right)^2 + \left(\frac{\partial \tau_w}{\partial z}\right)^2}. \quad (2)$$

The WSSG measured the spatial change of WSS along the blood vessel, where a high WSSG indicated a rapid change of the WSS. WSSG > 200 Pa/m was defined as high WSSG (Beier et al., 2016; LaDisa et al., 2004). In the model, the gradient in the *x* direction (major blood flow direction) contributed the most to the WSSG.

5.3.3 Data analysis

Tissue growth data were obtained from a previous animal study using high-resolution micro-CT imaging (Opie et al., 2017), where animals were implanted with the stent-electrode interface (Figure 5.2f). Stent-associated tissue thickness was measured from CT and histological slices (Figure 5.2g). Tissue thickness was averaged over the circumference of the blood vessel and computed along the length of the blood vessel. In the CFD model, the WSS results were exported to MATLAB to compute the circumferential averages and compare them with the average tissue growth.

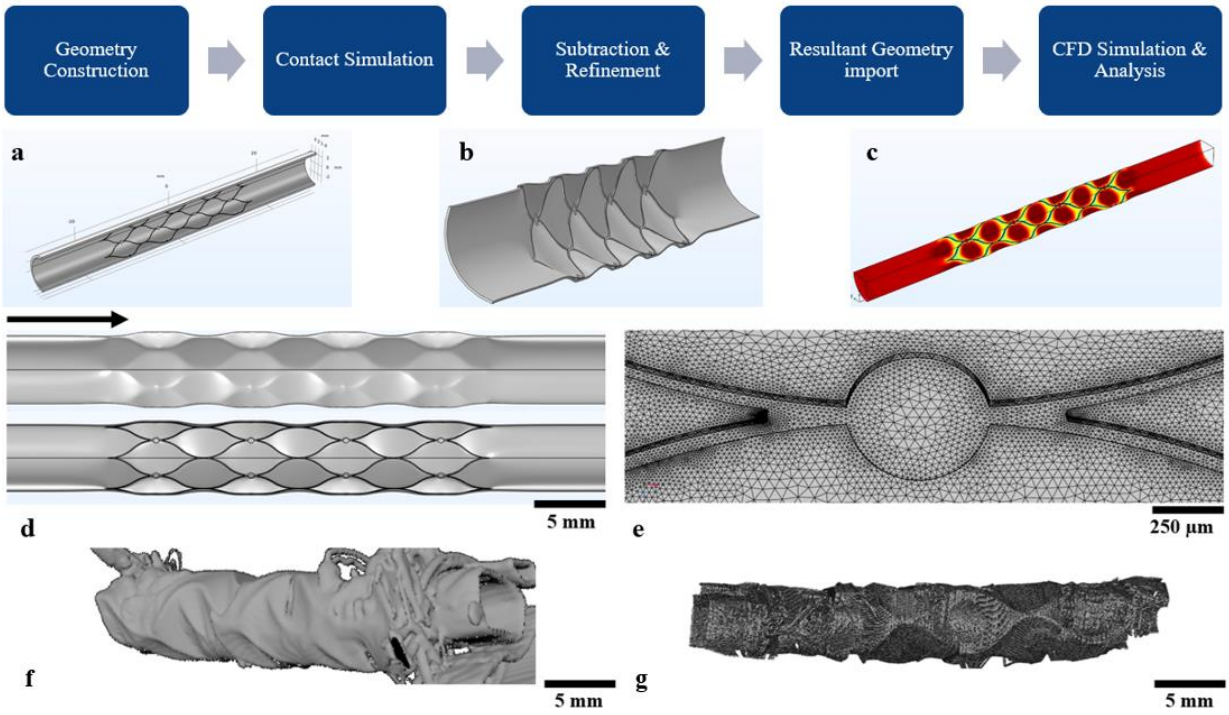

Figure 5.2 The workflow for deformed blood vessel wall model generation and CFD analysis. (a) A generalised blood vessel model with a stent-like neural interface. (b) The blood vessel was deformed by the expansion of the stent struts after the mechanical simulation. (c) Blood flow was simulated on the new deformed geometry to produce WSS results for the deformed model. (d) The deformed geometry is viewed from the outside and inside. (e) Tetrahedral mesh of the stent and blood vessel wall. (f) Blood vessel 3D segmentation from Micro-CT slices for sheep 2. (g) Blood vessel 3D coordinates extracted from Micro-CT slices for sheep 2. Stent artefacts were present, which made the reconstruction non-ideal for simulation.

5.4 Results

5.4.1 Wall Shear Stress (WSS)

Figure 5.3 showed the WSS distribution of the stented venous wall. In Case 1 (no deformation), the WSS was reduced in regions immediately surrounding the edges of the stent strut and the electrodes. The area of low WSS was 11% of the total stented area (Figure 5.3c). In Cases 2 (deformation ratio 1.05) and 3 (deformation ratio 1.1), the reduction of WSS became increasingly prominent with the increase in deployment ratio. A wider spread could be observed in both cases. The area subject to a low WSS rose to 12% and 26% (Figure 5.3c). In Cases 4 (deformation ratio 1.1, taper ratio 1.1) and 5 (deformation ratio 1.1, taper ratio 1.2), the tapering feature of the blood vessel caused a gradual decrease of WSS along the vessel length. In Case 4, the low WSS region around the stent was more obvious at the proximal (tapered) end of the stent than at the distal end. The area of low WSS caused by the stent was 19%. In Case 5, there was an abrupt decrease of the WSS at the distal end due to poor contact between the stent and the blood vessel wall. The area of low WSS for Case 5 increased to 26% (Figure 5.3c). In addition, the WSS was plotted along the axial line of the blood vessels. Cases 3 (with deformation) and 5 (with deformation and tapering) resulted in a more variable WSS along the length of venous sinuses compared to Case 1.

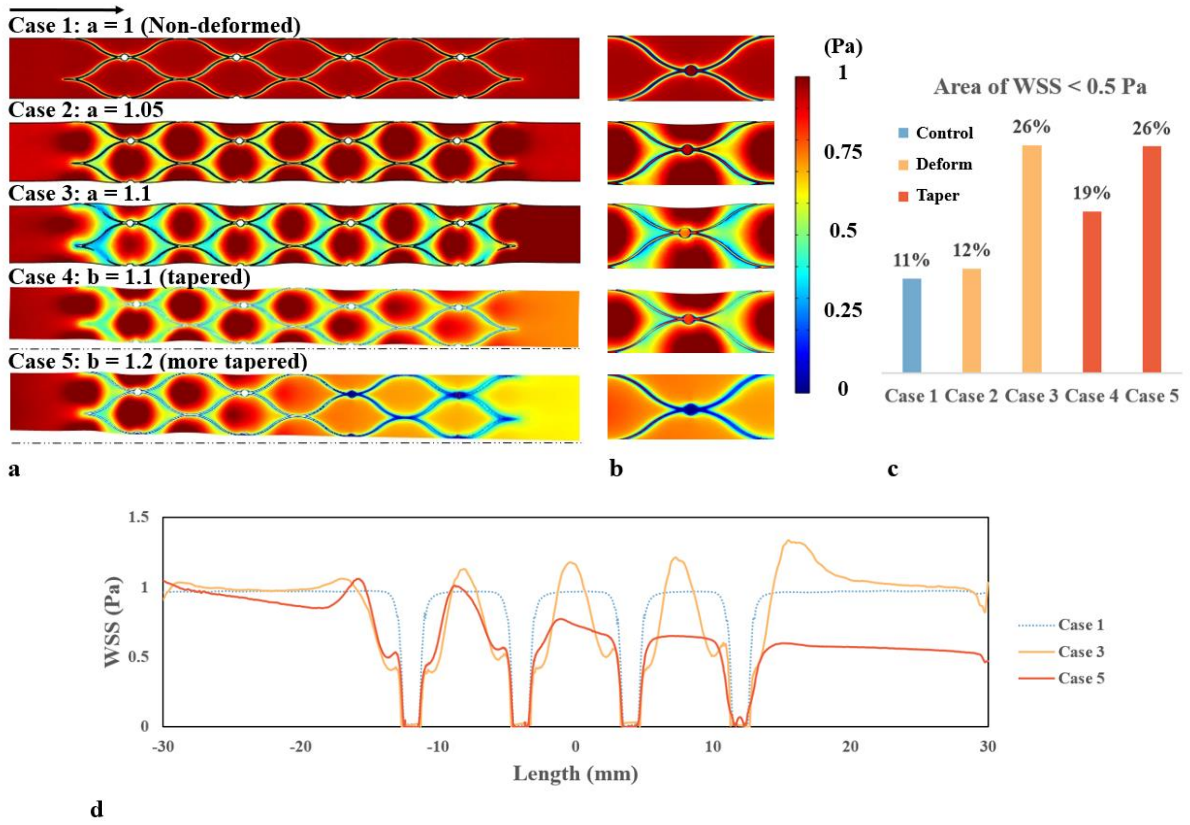

Figure 5.3 CFD Results for Wall Shear Stress (WSS). (a) WSS contour of the blood vessel wall (the black arrow indicates the blood flow direction). (b) A magnified view of the WSS pattern around the stent and electrode. (c) Histogram showing the area of WSS < 0.5 Pa with various stent-to-vein ratios. The area of the stent is not included in the area percentage. (d) Axial WSS distribution along the length of the blood vessels.

5.4.2 Wall Shear Stress Gradient (WSSG)

Figure 5.4 depicts the WSSG and the area subject to a high WSSG (> 200 Pa/m). In Case 1 (no taper non-deformed), a high WSSG was observed around the stent struts and electrodes (Figure 5.4b), indicating that the WSS varied rapidly (with an order of 1000 Pa/m) along the blood flow direction. The area of high WSSG contributed to 34% of the total area of the stented vessel (Figure 5.4c). In Case 2 (deformation ratio 1.05) and Case 3 (deformation ratio 1.1), a WSSG between 500 and 1000 Pa/m was observed in the deformed venous wall region (Figure 5.4a). The area of high WSSG histogram shows that deformation (Cases 2 and 3) increased the area of high WSSG by nearly 50% compared to the non-deformed idealised model (Case 1). In Cases 4 (taper ratio 1.1) and 5 (taper ratio 1.2), the proximal end of the stented region had a similar WSSG pattern due to deformation. However, high WSSG was mainly found around the stent and the area reduced to 69% and 36% in Cases 4 and 5 respectively (Figure 5.4c).

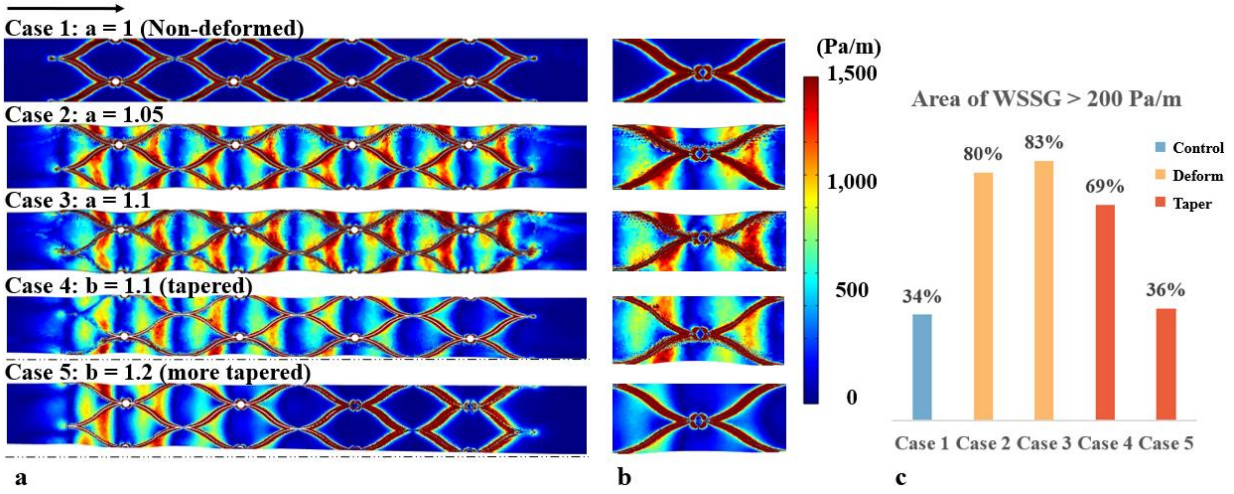

Figure 5.4 CFD results for Wall Shear Stress Gradient (WSSG). (a) WSSG contour of the venous wall (the black arrow indicates the blood flow direction). (b) A magnified view of the WSSG pattern around the stent and electrode. (c) Histogram showing Area of WSSG > 200 Pa/m with various stent-to-vein ratios. The area of the stent is not included in the area percentage.

5.4.3 Flow streamlines

Figure 5.5a illustrates the flow streamlines near the stent strut and electrode at the distal end of the stent. In Case 3 (deformation ratio 1.1), the stent was well apposed on the blood vessel wall, where a smoothed streamline was observed over the strut. In contrast, in Case 5 (taper ratio 1.2), flow disturbance characterised by twisted streamlines could be observed around the corners of the malposed struts. Secondary flow contours in Figures 5.5b and 5.5c implied that stent deployment altered the cross sections of the blood vessel lumen. In Case 2 (deformation ratio 1.05) and Case 3 (deformation ratio 1.1), deformation induced secondary flow (1-1.5 mm/s) from the straightened venous wall towards the centre. The magnitude increased dramatically with an increase in the deployment ratio. In Case 4 (taper ratio 1.1) and Case 5 (taper ratio 1.2), tapering caused a secondary flow pattern away from the centre. The magnitude increased slightly from 0.5 mm/s to 1 mm/s with an increase in the tapering ratio.

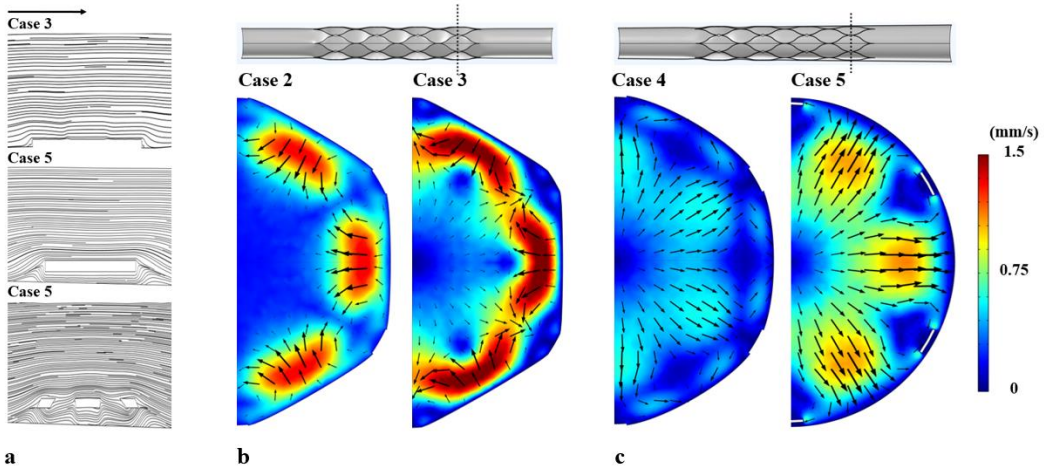

Figure 5.5 (a) Streamlines of blood flow over the stent struts and electrodes for Case 3 (deformation) and Case 5 (tapering). (b) Secondary flow magnitude at the blood vessel cross-section (dotted line) for Cases 2 and 3 without tapering. (c) Secondary flow magnitude at the blood vessel cross-section for Cases 4 and 5 with tapering.

5.4.4 Mean wall shear stress and tissue growth thickness.

Figure 5.6 shows the WSS contour and comparisons of mean WSS with the average tissue thickness in three implanted sheep (Cases 6-8). Regions subject to WSS less than 0.5 Pa were primarily found around stent struts for all cases and the flow downstream for Cases 6 and 8. Regions subject to WSS greater than 2 Pa were observed near the outer bend of Case 6 due to longer vessel curvature than Cases 7 and 8. The three mean WSS plots in Figure 5.6 (blue lines) show distinctive and non-uniform patterns in the stented region, varying between 0-3 Pa. In the sheep tissue thickness data (orange line), the tissue thickness at the proximal end was greater than the distal end for Cases 6 and 7. The peak of tissue thickness corresponded roughly to the regions with low WSS and vice versa. All the correlation plots showed moderate to strong levels of negative correlation between the mean WSS and tissue thickness, except for Case 6 with the length between 15 and 30 mm (Table 3).

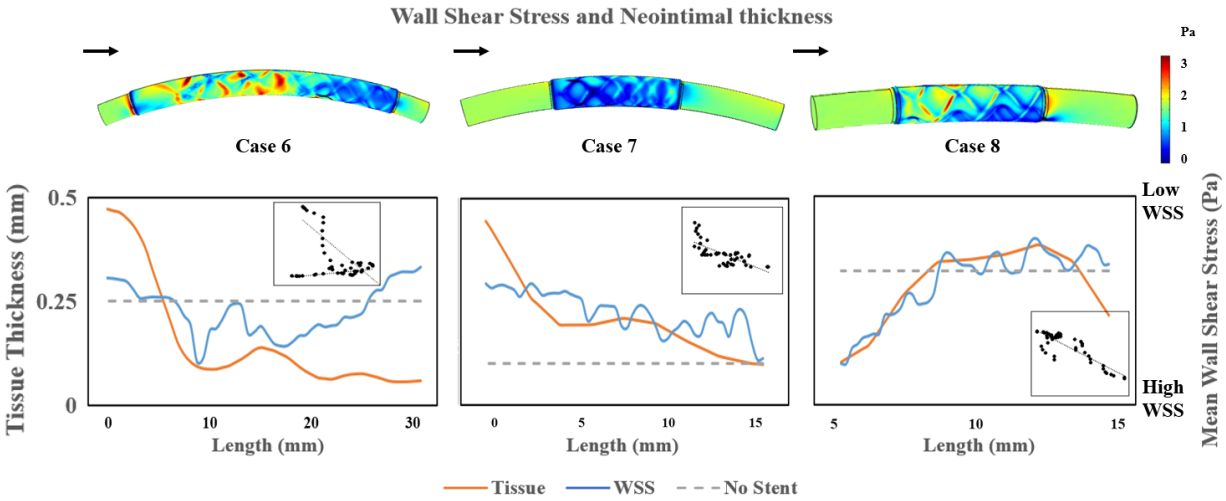

Figure 5.6 Comparison to Experimental Results. Top – WSS contour of the stented sheep blood vessel. Bottom – Blue: Circumferential average WSS along the length of the simulated blood vessel, computed from the WSS contour above; the WSS axis was flipped to compare trends between WSS and tissue thickness. Orange: Stent-associated tissue thickness in three sheep measured using Micro-CT imaging. Dashed line: Mean WSS value in the sheep blood vessels without a stent inside. Inset: Correlation between WSS and tissue thickness.

Case No.	Pearson's correlation coefficient (r)	p-value
6 (0~15mm)	-0.80	<0.001
6 (15~30mm)	0.73	<0.001
7	-0.72	<0.001
8	-0.86	<0.001

Table 3. Correlation coefficient and p-values for Cases 6-8.

5.5 Discussion

The thesis is the first to evaluate the haemodynamics in a cerebral blood vessel stented with an endovascular neural interface in idealised human and sheep Superior Sagittal Sinus models. The venous stenting literature lacks computational simulations that address venous blood flow and venous neointimal tissue growth in venous sinus stents. The interaction between venous stents and the venous blood vessel wall, as well as the factors influencing venous haemodynamics, remains unclear. Veins differ from arteries in terms of anatomical structures, blood flow characteristics, and

optimal stent designs. The study suggests that venous wall deformation may be a major contributor to changes in venous blood flow. This highlights the importance of considering venous deformation in mechanical simulations, which can provide more accurate estimates than computational fluid dynamics (CFD) analyses of rigid cylindrical blood vessels. As expected, the blood flow simulation revealed that stent implantation modified the haemodynamics by altering the shape of the blood vessel lumen, which decreased the Wall Shear Stress (WSS) and increased the Wall Shear Stress Gradient (WSSG) along the venous wall. Blood vessel shape (tapering and degree of deformation) also influenced how the haemodynamics in the stented blood vessel was impacted. In addition, the retrospective analysis on sheep blood vessels indicated that tissue thickness in the venous sinus could be correlated with the mean WSS patterns.

5.5.1 Haemodynamic impact determines venous neointimal growth.

The sheep model suggested that stent-based neural interfaces may have altered the mechanical environment of the blood vessel wall, promoting tissue growth over months of stent implantation. Data analysis showed a negative correlation between the shear stress and associated tissue thickness. This suggests that venous tissue growth may be determined by reduced shear stress and agrees with findings in coronary stenting that link low shear stress to neointimal overgrowth (Zun et al., 2019). Intimal growth has been observed in 14% of venous sinus stents (n = 473). The mechanism was uncertain but speculated to result from high shear stress and turbulence (Levitt et al., 2016; Pereira et al., 2021; Xu et al., 2015). However, the study suggests that the superior sagittal sinus has a low-shear environment and is not tortuous enough to cause turbulence. Tissue growth in the superior sagittal sinus is more likely to be triggered by the reduction rather than elevation in shear stress. In addition, the work adds to the recent work of Opie et al. (2017) and John et al. (2022), who provided preliminary examinations of tissue growth patterns in sheep venous sinuses. A clearer understanding is needed of the complex pattern of tissue growth. The computational models serve as additional case studies, leveraging existing data to explain these complex patterns using blood flow patterns. This approach addresses a key gap in previous studies and offers valuable insights for future stent-electrode design considerations.

With specific sheep CFD models, it was showed that the tissue thickness patterns were related to the shear stress pattern after stent implantation. By visualising the shear stress pattern, the CFD model has the potential to evaluate potential tissue growth in early-stage stent design testing and surgery planning for future stent-based neural interfaces. The novelty of the study lies in the complex tissue growth patterns observed, which are distinct from those seen in diseased arteries affected by atherosclerosis. Much of the results in the literature that rely on data from diseased arteries that are prone to plaque, thrombosis, and prolonged healing may not provide insights into normal tissue response in a healthy vein. The study closely examined the tissue response from a healthy venous vessel to better understand the tissue growth patterns in the targeted veins.

The study aimed to provide valuable insights, guidance, and simulation tools for future research in evaluating stent-electrode designs under normal venous flow conditions in healthy veins. To date, there are no studies showing tissue growth patterns and CFD of healthy veins. Unlike arterial walls, which often develop plaques consisting of fats, cholesterol, and aggregated platelets, the venous sinus walls do not have any pre-existing lesions or abnormal growth. The tissue growth patterns in venous sinuses are more varied and complex compared to the focal narrowing typically seen in arteries affected by atherosclerosis. Another key differences between work done previously on coronary arteries and the work in cerebral veins include the location and positions which also result in different boundary conditions. While CFD patterns may be somewhat similar due to the presence

of stent struts, the ranges of Wall Shear Stress and Wall Shear Stress gradient on the venous wall were lower due to over-expansion and slow non-pulsatile blood flow conditions.

The retrospective data of the sheep model was prone to artefacts. Only three out of twelve sheep imaging datasets contained intact tissue thickness measurements. The streaking artefact from the metal electrodes mounted on the stent strut made there appear to be sudden changes in WSS and tissue thickness data. In future studies, better imaging techniques or image processing algorithms are needed.

In addition, the current CFD model only simulated haemodynamics right after implantation. Vascular remodelling is a complex and time-evolving process. An interplay could exist between haemodynamics and tissue growth. After reendothelialization occurs, the neointimal tissue will merge over the stent surface. Haemodynamics could be further influenced by this growth, which would influence the subsequent tissue growth (Tahir et al., 2013). Intermittent measurement would be necessary to better understand the impact of stent haemodynamics over time. More work is required to validate the model and adapt it to human cerebral blood vessels which can provide significant benefit to clinicians and manufacturers in improving the design of the devices to suit patients.

5.5.2 An oversized stent has more impact on venous haemodynamics.

In previous works, most of the modelling studies use an idealised model without considering tapering or deformation due to the high computational cost (Chen et al., 2017; Jiang et al., 2019). Instead, a non-deformed model is commonly applied to study the haemodynamics of various stent designs and stented blood vessels with complex geometries (Gundert et al., 2012; Hsiao et al., 2012; Katritsis et al., 2012). While results from the non-deformed model provided some explanation of what is happening in the blood vessel, it grossly underestimated the haemodynamic impact of the intervention due to the inaccurate boundary conditions (i.e., blood vessel shape). The results show that the inclusion of venous wall deformation resulted in a substantial difference in WSS and WSSG patterns, increasing the area subject to low WSS and high WSSG by 15% and 46%, respectively (Figures 5.3 and 5.4).

The simulation results agreed with coronary artery stenting CFD studies, which showed deformation strongly affects the haemodynamics of various stent designs (Frank, Walsh, & Moore, 2002; Williamson et al., 2022). However, there was greater and more non-uniform deformation along the venous sinus wall, which has not been quantitatively analysed in the literature. It was found that a larger deformation caused a much greater elevation in the area subject to low WSS (Cases 2 and 3). The findings highlight key differences between arteries and veins. On one hand, arteries, due to their greater stiffness, experience minimal lumen deformation and are highly influenced by the presence of stent struts (Frank, Walsh, & Moore, 2002). On the other hand, veins, being more compliant, undergo significant lumen deformation and are less impacted by the presence of the thin stent struts of the venous sinus stent.

The findings are crucial for stent size selection (Bernini et al., 2022; Kitahara et al., 2017) as suboptimal stent expansion leads to adverse clinical events (Kitahara et al., 2017). In the literature, oversized stents with a ratio from 1.1 to 1.2 are commonly used to fully expand the diseased blood vessel without incomplete stent apposition and device migration (Bernini et al., 2022). However, the simulations suggest that using an oversized venous stent on a healthy venous sinus will substantially deform the venous wall unevenly and modify the blood flow patterns, promoting

complex tissue growth patterns in the venous sinus. Considering the relationship between the area of low WSS and stent-to-vein ratio, further study will be required to determine the optimal oversizing parameter for the venous sinus stent. The deformed model will be the essential tool to determine the optimal venous stent designs, such as a tapered or a personalised stent that fits better in the venous sinus to mitigate the risks of venous tissue overgrowth. The presented venous model provides a better estimation of the haemodynamic effect and wall deformation in the venous sinus than previous models, thereby improving the testing of future venous implant designs and evaluation of venous neointimal growth.

5.5.3 Blood vessel tapering challenges the optimal stent design.

The findings indicate that the commonly used oversizing stent may lead to increased tissue growth, particularly in tapered blood vessels. It was observed that a larger deployment ratio at the narrower end of the original blood vessel stimulated more tissue growth. Future research should focus on developing tapered or customized stents that can reduce deformation while preventing migration. This study area can drive advancements in stent design, enhancing their effectiveness in clinical applications. Blood vessel tapering could make the selection of appropriate stent size more difficult by adding complexity to the blood flow pattern. Tapering is a common feature in the human venous sinus. For example, the human central sulcal vein has a mean distal (blood flow inlet) diameter of 2.3 mm and a mean proximal (outlet) diameter of 4.9 mm (tapering ratio b > 2) along 100 mm length (Oxley et al., 2016). The superior sagittal sinus naturally tapers along its entire length, with a ratio greater than 2 along 100 mm. In the stented region, the inlet is approximately 10-20% narrower than the outlet, resulting in a tapering ratio of 1.1-1.2 (Oxley et al., 2016). Post-stent implantation, the blood vessel wall was stretched by the self-expanded oversized stent to almost the same diameter as the stent itself (Figure 5.2f), causing more pronounced deformation at the inlet and slight deformation at the outlet. This is reflected in Case 4.

However, in Case 5, a larger tapering ratio led to suboptimal stent expansion at the distal end, resulting in a large area of low WSS region at the distal end (Figure 5.3). At the proximal end of the stented region, the narrowed inlet will suffer from a larger blood vessel wall deformation. At the distal end, the wider outlet may be prone to stent struts overhangs (malapposition). Poor stent apposition to the blood vessel wall is common and has been extensively studied due to its strong association with delayed stent incorporation and late thrombosis (Foin et al., 2014). Previous CFD models have focused on malapposition in curvature (Chen et al., 2017) and elliptical lumen shape (Jiang et al., 2019). Malapposition in tapered arteries has gained interest only in recent years (Liu et al., 2022). The simulation considered tapering in a deformed blood vessel model, which has not been studied before. The results suggest that tapering needs to be considered when choosing the stent design, especially for venous sinus stents. It is essential to implant the stent with an appropriate expansion ratio that matches the blood vessel tapering ratio or even consider a customised stent with a tapered design that may fit better for an individual patient to mitigate the risks of adverse events. The presented CFD model would be a reliable platform to help determine stent designs for patients with tapered blood vessels.

5.6 Limitations and future works

The CFD model had several assumptions. First, the mechanical simulations assumed that the venous wall was isotropic and elastic instead of anisotropic and hyper-elastic or viscoelastic. This is because relevant material data is unavailable in the literature. However, the mechanical model was used to generate a reasonable estimation of the blood vessel shape similar to the geometry from the reconstructed micro-CT images (Figure 5.4). Mechanical simulation created the geometric details of

how the stent was embedded in the venous wall, which could be used for flow simulation. It is necessary to note that solving the contact problem between the stent and vessel wall is computationally expensive (Chua, Mac Donald, & Hashmi, 2002). A deformed model with more realistic material properties is recommended to yield a more realistic haemodynamic simulation. Given that the previous experiment had been completed, gathering additional animal-specific boundary conditions and material properties was not feasible. More accurate animal-specific or patient-specific input information is currently lacking in the literature. Obtaining accurate measurement will allow achieving a more accurate and quantitative understanding of the events in the venous sinuses and determine optimal design parameters for future venous implants. In future work, it is required to validate the blood flow pattern and the material deformation of venous sinus wall in the models using animal experiments. The model will hold promise into efficient testing of optimal stent designs that minimize such deformation.

Second, the CFD boundary condition was taken from the average venous sinus blood flow in the literature. Assuming a constant flow rate may lose information relevant to neointimal tissue growth, such as instantaneous wall shear stress and its oscillatory behaviour within one cardiac cycle (Cunningham & Gotlieb, 2005; Friedman et al., 1987). However, venous flow is relatively slower and less pulsatile than arterial flow. Implementing average blood flow to study venous haemodynamics is justified in the literature (Xu et al., 2015). Future work will require a time-dependent velocity waveform if it is a patient-specific CFD model.

5.7 A new frontier in endovascular neural interfaces

Currently, stent technology has been utilized beyond its traditional purposes, such as the SMART stent (stent with flow or pressure sensors) (Chen et al., 2018; Islam et al., 2020) and stents with recording electrodes (Opie et al., 2018). By adding sensors and electrodes, stents are empowered with more functions to serve as potential new or better treatment options for intractable diseases. Specifically, the endovascular neural interface has adapted to stent technology well, making high-fidelity brain signal recording minimally invasive (Opie et al., 2017; Oxley et al., 2016). Despite tissue proliferation in the blood vessel, the endovascular approach has great potential to improve outcomes for patients since it possesses a much lower risk of complication compared to conventional cortical electrodes (John, Grayden, & Yanagisawa, 2019). The use of neurovascular stents and endovascular neural interfaces will continue to sprout over the next decade. Hence, it remains essential that the risks of stent complications are mitigated. There is a need to better characterize their impact on blood flow dynamics. This is especially important in blood vessels with complex geometry due to curvature and tapering, which increases the risk of stent size mismatch. CFD modelling enables a cost-efficient approach to examining the impact of different stent designs on blood vessels; it will provide critical insights that will enable the ongoing development, testing, and regulation of neurovascular stents and endovascular neural interfaces. CFD should be extensively used to evaluate the suitability of any new stent designs that are intended for patient use.

The use of neurovascular stents and endovascular neural interfaces will continue to increase over the next decade and there is a need to better characterise their impacts on blood flow dynamics. While previous research has provided some insight into tissue response, researchers are yet to determine the major driving force of tissue response to shed light upon future stent-electrode design. More importantly, ethical approvals for stent-electrode devices heavily rely on animal data, particularly from studies involving sheep, to facilitate the transition to human trials. The sheep models serve as additional case studies, leveraging existing data to explain these complex patterns using blood flow patterns and offers valuable insights for future stent-electrode design

considerations. The biomechanical environments of human and sheep venous sinuses are similar, characterized by slow, non-pulsatile blood flow and compliant venous wall material properties. The large deformation simulated by the human model aligned with observations in sheep. Specifically, greater deformation at the inlet, caused by stent over-expansion, resulted in lower Wall Shear Stress, potentially explaining the tissue growth patterns observed in sheep. Despite the anatomical difference between sheep and human venous sinus, which may result in tissue response, the similarity in blood flow patterns and material interactions between the metallic stent and venous wall suggests that the results can be extrapolated. The results provide the first examination of haemodynamic changes and their correlation with neointimal thickness in endovascular neural interfaces after implantation. Studying blood flow is especially important when the stented blood vessel becomes complex due to blood vessel deformation and tapering. These results provide critical insights that will enable the ongoing development, testing, and regulation of neurovascular stents and endovascular neural interfaces.

5.8 Chapter summary

This chapter uses a more realistic blood vessel model to study blood flow in veins implanted with endovascular neural interfaces. Blood flow (haemodynamics) was identified as a crucial predictor of neointimal growth in stented blood vessels. This chapter also highlighted that the vascular wall deformation dramatically influences the biomechanics inside the blood vessel, which can exacerbate vascular remodelling and complication risks after device implantation. While there is an increasing application of endovascular neural interfaces in veins in the brain, it becomes critical to decipher how the device can impact blood flow and subsequent vascular remodelling in veins. This study investigated the haemodynamics of a stent-electrode array in a venous blood vessel computational model. Simulation results suggest that venous wall deformation caused an increase in regions subject to low WSS and high WSSG, which may accelerate tissue growth in the blood vessel. The observed neointimal proliferation in sheep was negatively correlated with the mean WSS pattern. Future work will aim to validate the computational model and understand the correlation between blood flow and endothelial growth in the vein, which may change in the long term. Based on simulation results, it is vital to include venous deformation in future CFD studies and to place a stent with an optimal oversizing ratio to minimize the haemodynamic impact of a stent.

Chapter 6 – Haemodynamics of Stent-Mounted Neural Interfaces in Sheep Venous Blood Vessels for prediction of Venous neointimal growth

6.1 Aims of study and novelty.

The aims of this study are twofold. First, it seeks to develop a realistic computational model using experimentally gathered pre- and post-implantation blood vessel geometry and blood flow data. Second, the study aims to investigate the relationship between neointimal tissue growth and blood flow conditions over time following implantation. Previous research has shown that stent implantation alters blood vessel lumen geometry, potentially affecting blood flow and promoting further growth that could impede venous drainage. However, due to limited experimental data, there is a critical need to establish a time-dependent correlation between blood flow and tissue growth, which is lacking in the literature on venous stents. This chapter aims to address this gap by recording changes in blood flow and tissue growth patterns in cerebral blood vessels up to 28 days post-implantation. The discovery of a power law correlation between Wall Shear Stress and venous tissue growth is a significant contribution to the literature, specifically concerning venous neointimal hyperplasia. These findings provide specific experimental data supporting the evaluation of hemodynamic impact and tissue growth for future endovascular neural interfaces in a reliable and efficient manner.

This chapter has broader implications, offering a baseline not only for understanding the response of stent-electrode arrays but also for other venous implants in the venous sinuses. It indicates the expected level of tissue growth for venous devices, highlighting the limitation of relying on data from diseased arteries and veins, which may not accurately reflect normal tissue response in a healthy vein. The power law correlation identified in this chapter lays a foundation for research and in-silico testing related to tissue response and the long-term stability of stent-electrode devices in venous systems in the brain and neck. Additionally, with more patient data, there is potential to create patient-specific models using the presented method, further developed for surgical planning and early intervention decisions. Researchers are exploring novel designs to enhance device safety and performance, with evaluation of haemodynamics being crucial, as the mechanical environment influences tissue response. The computational models developed in this study pave the way for future research in device evaluation.

6.2 Introduction

Venous stenting is performed on patients with intracranial hypertension to support collapsed venous sinus in the brain (Daggubati & Liu, 2019). With the recent advances in stent-electrode technology, venous stenting has now been used in healthy blood vessels as smart devices to record (endovascular encephalography) (Oxley et al., 2016) and stimulate the brain (endovascular neuromodulation) (Opie et al., 2018) through surrounding blood vessels. Owing to its minimal invasiveness, the endovascular approach has sparked research utilizing electrode-mounting venous stents to record brain activity (Forsyth et al., 2019), treat neurological disorders (Rajah et al., 2018), and develop neural prosthesis for paralysed patients seeking to restore volitional movements (Oxley et al., 2020). With the growing interest in repurposing venous stents for neuromodulation, a deeper understanding of venous stent-related complications, especially neointimal hyperplasia, is needed.

Venous neointimal hyperplasia is characterized by excessive endothelial growth post-intervention, affecting 5-10% of stent recipients globally (Collins et al., 2012). Tissue overgrowth can cause severe narrowing (greater than 50%) of the vessel lumen over time, elevating the risks of vessel occlusion in the long term. The underlying mechanism of hyperplasia, as suggested by arterial stent studies, is the reduction of Wall Shear Stress (force generated by blood flow onto the blood vessel wall) after stent placement (Roux et al., 2020; Wang et al., 2018). A low shear environment (WSS < 0.5 Pa) can induce cell proliferation in arteries (Bartlett et al., 2024). However, venous neointimal hyperplasia remains less reported. Blood flow has been speculated as a potential factor affecting hyperplasia in central venous catheters, pacemaker leads, and haemodialysis catheters, but supporting data are limited and unvalidated (Lonyai, Dubin, Feinstein, et al., 2010; Peng et al., 2017). Furthermore, the tissue growth patterns in venous sinuses are more varied and complex compared to the focal narrowing typically seen in atherosclerosis and venous stenosis (Ballout et al., 2024). Unlike arterial walls, which often develop plaques consisting of fats, cholesterol, and aggregated platelets (Baaten et al., 2024), the veins that the stent-electrode devices target do not have any pre-existing lesion or abnormal growth as they are intended for other applications. In this case, insights from arterial stents may not fully explain the factors inducing complex tissue growth patterns in the venous sinus. To better understand tissue growth in healthy venous sinuses for future development of stent-electrode devices, and to address the research gap for venous neointimal hyperplasia, the thesis investigated tissue growth in veins with stents.

This research aims to bridge the gap between tissue response and venous implants and investigate the impact of venous stenting on blood flow and tissue growth patterns. Using Computational Fluid Dynamics validated by animal experiments, the thesis explores blood flow and tissue responses shedding light on critical hemodynamic metric for venous stents. This research contributes valuable insights into the hemodynamic impact of venous stenting, offering crucial considerations for the design and application of the next generation of venous implants.

6.3 Methodology

6.3.1 Animal experiment and follow-ups

Experiments were conducted with approval from the animal ethical committee at The Florey Institute of Neuroscience and Mental Health following the NHMRC Principles of Laboratory Animal Care, Prevention of Cruelty to Animals Act, Australia, 2004, and Australian Code of Practice for the Care and Use of Animals for Scientific Purpose (8th edition, 2013). One cohort (n = 8) of adult Merino was used. For each sheep, the left jugular vein was implanted with Cordis SMART Control Biliary Stent for 4 weeks (28 days) while the right jugular vein (the other side) was included in the control group for comparison.

Before and after stent implantation, Doppler Ultrasound (GE Logiqe) was used to measure the mean blood flow velocity in the sheep jugular vein. During stent implantation, the sheep was anesthetized before stent implantation surgery was performed. The venous stent was inserted via a cut-down and cannulation of the jugular vein. The procedure was then followed by catheter venography of the jugular vein with the Ziehm Vision FD C-arm X-ray. Venography was repeated at different angles from 30 to 135 degrees (the limits of the C-arm system) with a step size of 15 degrees to capture the circumferential venous lumen boundary. A bolus of heparin (150 units per kg) was injected during stent implantation to prevent acute thrombosis. Follow-up venograms were conducted on

Days 7, 14, 21, and 28 after implantation to confirm vessel patency and monitor the lumen change in the jugular vein.

As shown in Figure 6.1, taking an X-ray image without injecting contrast agent allows measurement of stent size using the radio-opaque markers, which have known diameter of 8mm, as a reference. After injecting the contrast agent, the blood vessel lumen becomes visible under the X-ray. The image can then be processed to extract the blood vessel wall boundaries and centreline, enabling the determination of the lumen diameter.

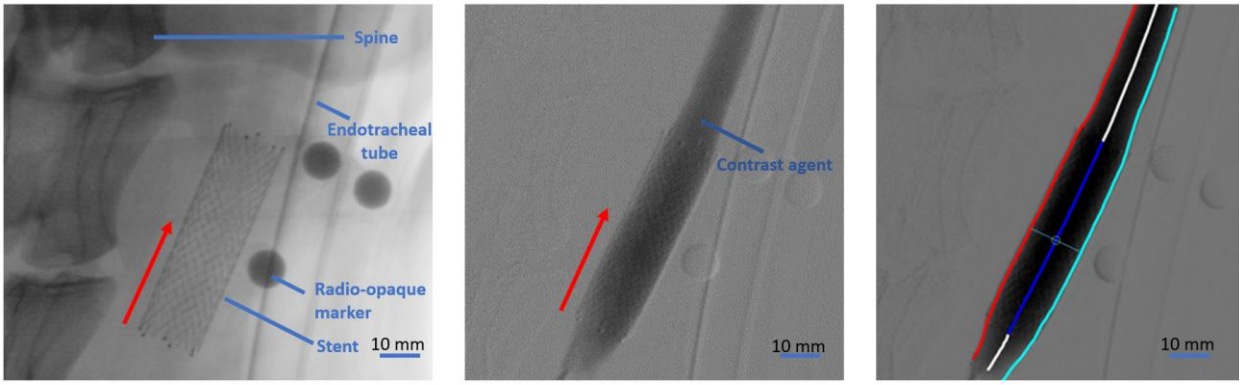

Figure 6.1 Venograms of stent and the jugular in sheep No.8. A: X-ray showing the sheep spine, stent, ventilation catheter, and three radio-opaque markers (d=8mm). Red arrow indicates the blood flow direction. B: Venogram showing the blood vessel lumen after contrast agent injection. C: Venogram showing the blood vessel boundary (red and cyan) and centreline (blue) from image processing and boundary extraction algorithms.

In addition, Doppler Ultrasound was performed to examine the change in blood flow rate. As shown in Figure 6.2, the venous flow velocity waveform was measured at the centre of the blood vessel lumen's cross-section. Measurements were taken at the inlet, mid-stent, and outlet locations. The

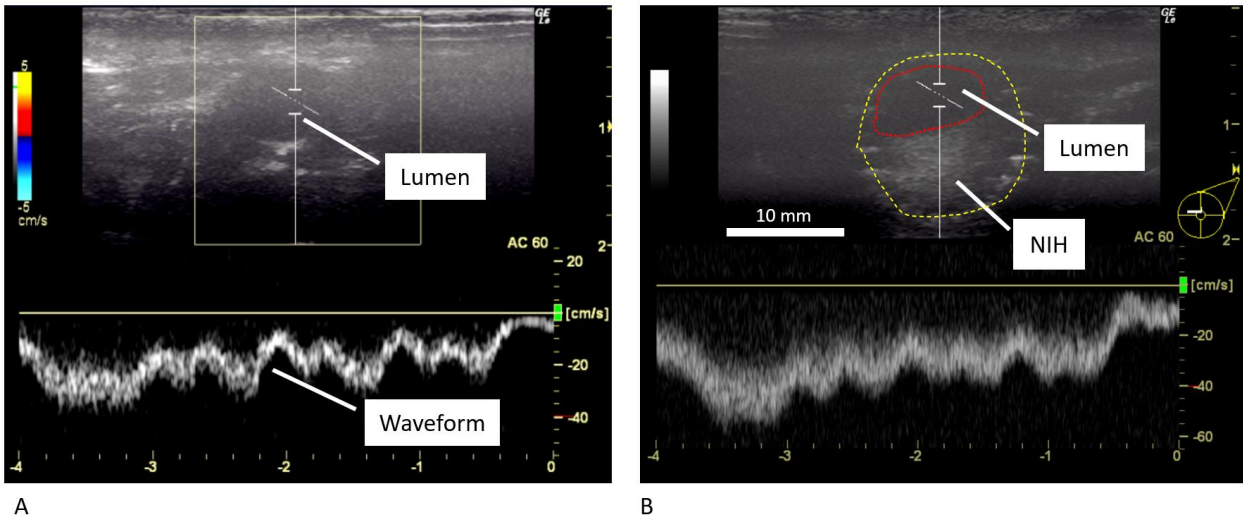

Figure 6.2 Doppler ultrasound showing blood vessel cross-section and blood flow velocity waveform with respect to time (x-axis). A: control blood vessel (no stent) B: with stent (brighter circular-shape region) and neointimal hyperplasia (NIH) region.

waveform, pulsating between 20 and 40 cm/s, was digitized before use as the velocity input for the computational model.

On Day 28, the sheep was euthanised and the stented portion of the jugular vein was extracted for a CT scan using the SCANCO µCT 50 to examine tissue growth inside the stent and the lumen area along the stented segment was measured.

6.3.2 Image processing and reconstruction

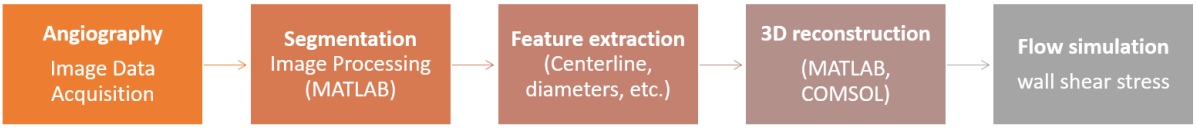

Figure 6.3 Geometry reconstruction workflow

The construction of sheep jugular CFD model required venography, image segmentation, blood vessel shape extraction, and geometry reconstruction (Figure 6.3). The reconstructed geometry was then used for blood flow simulation for Wall Shear Stress calculation. The following steps were taken.

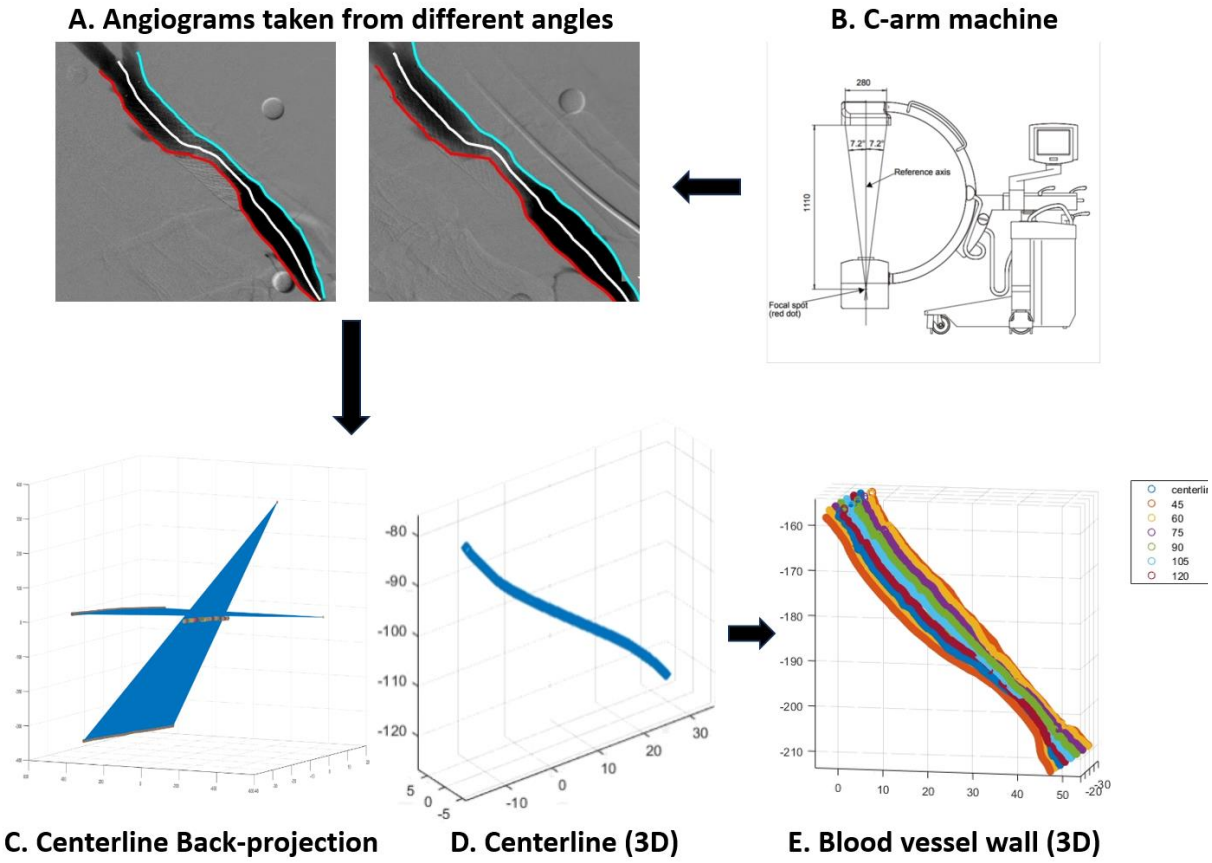

Figure 6.4 The workflow of venogram 3D reconstruction for Computational Fluid Dynamics modelling. The centrelines from the venograms with different angles (A) were extracted from the C-arm (B) and back-projected into 3D space (C, D). The wall boundaries were then mapped around the 3D centreline to form the 3D geometry of the blood vessel (E).

After obtaining the venograms from multiple angles, the author used image processing software ImageJ and MATLAB to extract the blood vessel boundaries and centrelines for each angle on different days. Examples are shown in Figure 6.4A. Image processing involved thresholding to isolate the contrast flow regions, filtering to remove any artefact from surroundings, and edge detection to locate the pixel location of the blood vessel wall. The same steps were performed for all the venograms with different angles on the same day. Next, the author used MATLAB to project the 2D images back to 3D space and map the 2D coordinates of the blood vessel wall to form the 3D cross sections of the blood vessel lumen, as shown in (Figure 6.4B). Using the measured distance from the sheep's neck to the X-ray detector, the 3D coordinates of the blood vessel wall boundaries and centrelines were generated via back-projection methods, as shown in Figure 6.4C. With the centreline defined in 3D space, the blood vessel wall boundaries were mapped around it (Figure 6.4D). A 3D representation of a blood vessel is depicted in Figure 6.4E. The reconstruction workflow was performed for all the sheep in the cohort for all the venograms from Days 0, 7, 14, 21, and 28.

6.3.3 Computational Fluid Dynamics

The 3D geometry of the blood vessels was generated by lofting, which applies algorithms to find a smooth 3D shape that fit the set of planar cross-sections of the jugular vein from MATLAB. The reconstructed geometries of one sheep on different days are demonstrated in Figure 6.5, which shows the blood vessel lumen narrowing due to accumulated tissue growth over 28 days. The blood vessel lumen diameter reduced gradually, and a greater amount of growth happened near the stent inlet and outlet regions.

Then, using COMSOL Multiphysics 5.6, the author applied a time-dependent user-defined function to represent the velocity waveform obtained from the Doppler ultrasound measurement (Figure 6.2) as the boundary condition. The flow at the inlet was set to be fully developed Womersley profile. The geometry was meshed using tetrahedral elements with four boundary layers. After simulation, results including blood flow velocity and time averaged WSS were computed for further analysis.

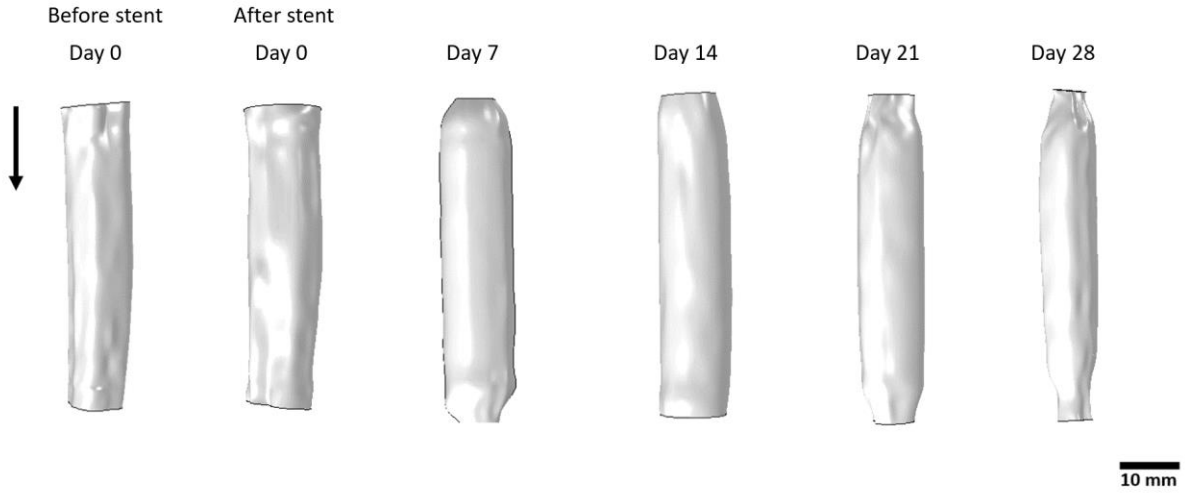

Figure 6.5 Blood vessel lumen 3D model reconstructed from venograms taken from different angles (left to right: Day 0 before implantation, Day 0 after implantation, Day 7 ,14, 21, and 28. Arrow indicates blood flow direction. Stents are excluded in the computational model due to complexity.

6.3.4 Model Validation

The thesis performed geometry validation of the CFD model using micro-CT scans. The lumen cross-sectional area along the blood vessel on Day 28 was compared between COMSOL and micro-CT scans, with an example shown in Figure 6.6A. The author took area measurements using MATLAB on 1600 slices with a step size of 40 slides. The scatter plot in Figure 6.6B shows that errors predominantly fell within 5%, implying that the geometries generated by COMSOL matched the actual size of the blood vessels.

In addition, the CFD results were validated by comparing the mean outlet velocity between the computational model and the Doppler Ultrasound measurements. A similar waveform was observed, as shown in Figure 6.6C, suggesting that the computational model provided close estimates of the actual blood flow in the blood vessel.

6.3.5 Postprocessing of simulation results

The results collected from COMSOL, such as the Wall Shear Stress, were exported as 3D coordinates of the blood vessel wall, containing diameter, location information on the blood vessel, and the WSS value at the corresponding location. The 3D coordinates cloud data were then unfolded and mapped to 2D space based on radial position and axial position along the blood vessel to aid the viewing of flows and tissue growth patterns.

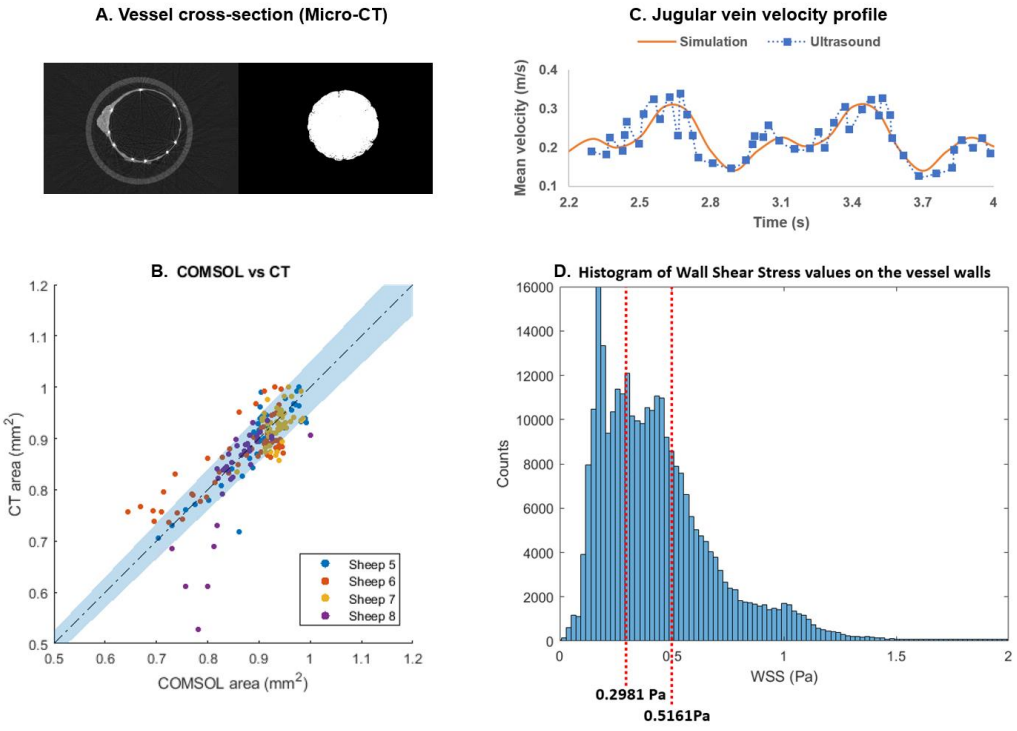

Figure 6.6 CFD model validation and Wall Shear Stress value collection. Micro-CT scans showing the blood vessel and stent cross-sectional structures (A. Left) and lumen area (A. Right). Comparison of area measurements between CT scans and COMSOL. 184 data points, evenly sampled from CT slices and COMSOL model (B). Blood flow validation for sheep No.02 at Day 7 – outlet velocity comparison between COMSOL and Ultrasound (C). WSS value distribution in all stented sheep blood vessels for statistically determining the WSS thresholds for low, mid, and high WSS (D).

6.3.6 Statistical Analysis

Based on the 2D contour map of tissue growth and Wall Shear Stress, Pearson's correlation was computed to quantify the relationship between the Wall Shear Stress pattern and the tissue thickness over 4 weeks (28 days) along the blood vessel wall. Pearson's correlation between 0.1 - 0.3, 0.31 - 0.6, and 0.61 - 1.0 represents low, moderate, and strong correlation, respectively. Apart from correlation analysis, statistical analysis was performed to calculate the mean contribution of Wall Shear Stress on tissue growth thickness, adapting from Hoogendoorn et al. (2020). In this analysis, the distribution of Wall Shear Stress was visualized in the sheep cohort (Figure 6.6D). Statistical analysis was performed using quantile function in MATLAB to categorize Wall Shear Stress values. The values of 0.2981 and 0.5161 divided the Wall Shear Stress probability distribution equally into low (<0.2981 Pa), mid (0.2981-0.5161Pa), and high (>0.5161 Pa) Wall Shear Stress. Then, masking was applied on the tissue growth pattern to separate regions promoted by low Wall Shear Stress from mid and high Wall Shear Stress. Finally, the average tissue growth thickness was calculated in each category of the Wall Shear Stress for comparison of which level of Wall Shear Stress contributes to the most tissue growth.

6.4 Results

6.4.1 Lumen size over 4 weeks (28 days)

Figure 6.7 shows the lumen size of the jugular vein in eight sheep over 4 weeks (28 days), separating values for the inlet, middle point, and outlet of each stent. Overall, lumen size shows a decreasing trend over the 4 weeks (28 days) of stenting. Comparing day 0 immediately before (D0) to after (D0s) stenting, the average ± standard deviation of lumen diameter increased from 12.9 ± 0.6 mm to 13.3 ± 1.6 mm. Between Day 0 after stenting and Day 7, a large decrease in diameter was observed to 11.0 ± 1.5 mm. From Day 7 to Day 28 after stenting, tissue growth followed a gradually

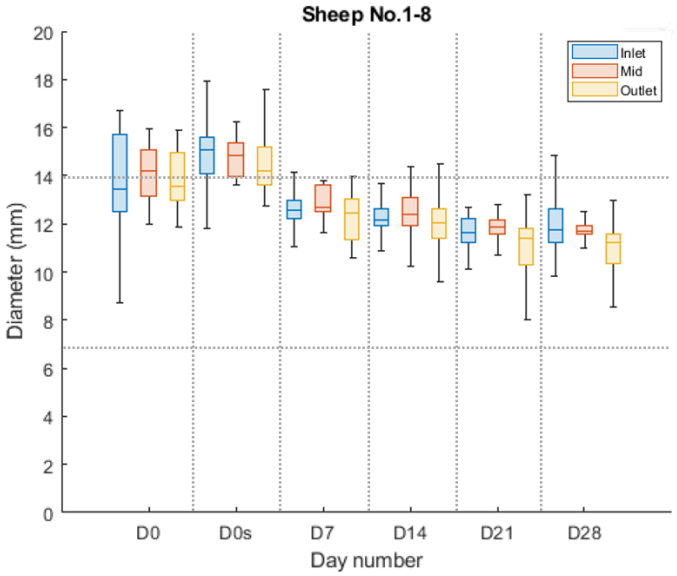

Figure 6.7 Box and whisker plot (with medians and IQRs) of sheep jugular vein lumen size over 4 weeks (28 days) across 8 sheep. The lumen size data was divided into inlet (blue bar), mid (red bar), and outlet (yellow bar) by the vertical dash lines. Each of the three regions takes up one third of the stented region in the sheep jugular vein. The lumen size dataset includes venographic measurements before stenting (D0), just after stenting (D0s), and four weeks of

decreasing trend, from 11.0 ± 1.5 mm (D14) to 10.8 ± 0.8 (D21) to 10.6 ± 1.1 mm (D28). On Days 7, 14, 21, and 28, the minimum lumen diameters were mostly found in the outlet region (minimums are 10.6, 9.6, 8.0, and 8.5 mm, respectively). The lumen diameter was above 50% of the original average size for all stents across all days.

6.4.2 Wall shear stress, tissue growth patterns, and their correlation

The thesis calculated the wall shear stress and associated tissue growth thickness for all sheep. Sheep 8 was used as an example due to its strong negative correlation between the Wall Shear Stress and tissue growth thickness. Data for other sheep, which mostly showed negative correlation, are included in the appendix. The WSS patterns (Figure 6.8A) over 4 weeks showed that the inlet region suffered from a low WSS compared to other regions, indicated by blue. The outlet experienced a high WSS, highlighted by yellow. The pattern matches the tissue growth pattern measured over 4 weeks (Figure 6.8B) with more tissue growth observed near the inlet than other regions while less changes were observed near the outlet.

The correlation plot of thickness vs. WSS (Figure 6.8C) was generated by comparing values from the same locations. 50 data points were evenly sampled from the 2D contour maps of both WSS and tissue growth. There was a strong negative correlation ($r = -0.65$, $p < 0.05$) between the WSS at the day of stenting and tissue growth thickness after 28 days. The histogram (Figure 6.8D) shows that tissue growth was primarily driven by low WSS. On average, regions with low WSS had about 1.9 mm of growth over 4 weeks; mid WSS regions had about 1.2 mm of growth on average, and high WSS regions had about 0.8 mm of growth.

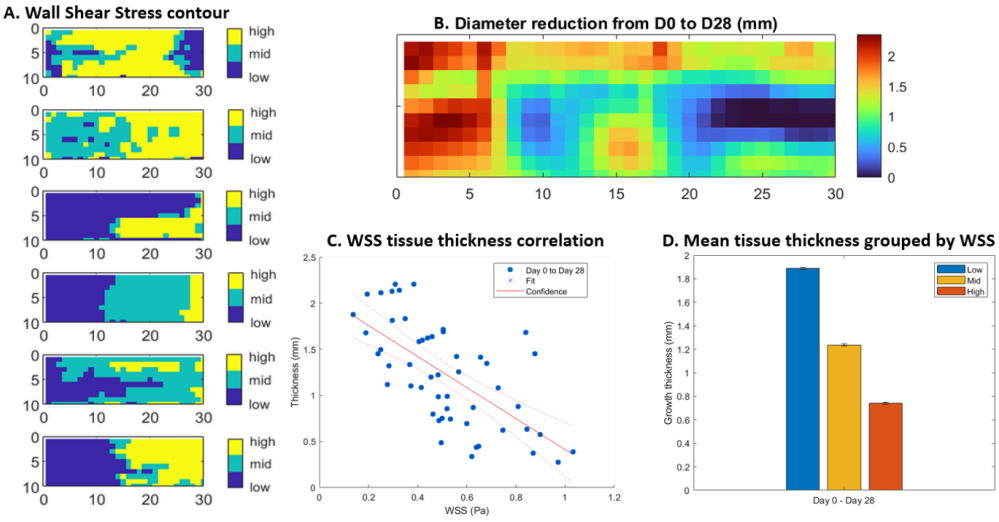

Figure 6.8 WSS and tissue growth for Sheep 8. WSS contour map, with regions divided into low, mid, and high WSS regions. Blood flow direction is from left to right (A). Diameter reduction along the stented region, showing more tissue growth at the inlet (B). Correlation between WSS and tissue thickness (R = -0.6544; P < 0.05) (C). Mean tissue growth contributed by the low, mid, and high WSS regions (D).

6.4.3 Correlation analysis between Wall Shear Stress and tissue growth thickness

A negative power law function, $y = 0.72 * x^{-0.87}$, was fit to the data. Figure 6.9 contains correlation data taken from Figure 6.8C and from all the other stented sheep. The R-squared value of 0.3293

indicated a moderate level of fit, where approximately one third of the variations in tissue growth thickness values could be explained by the WSS values. A Pearson correlation coefficient of -0.4889 indicated a moderate negative correlation between the WSS and the tissue growth thickness across all the sheep, with p-value less than 0.001.

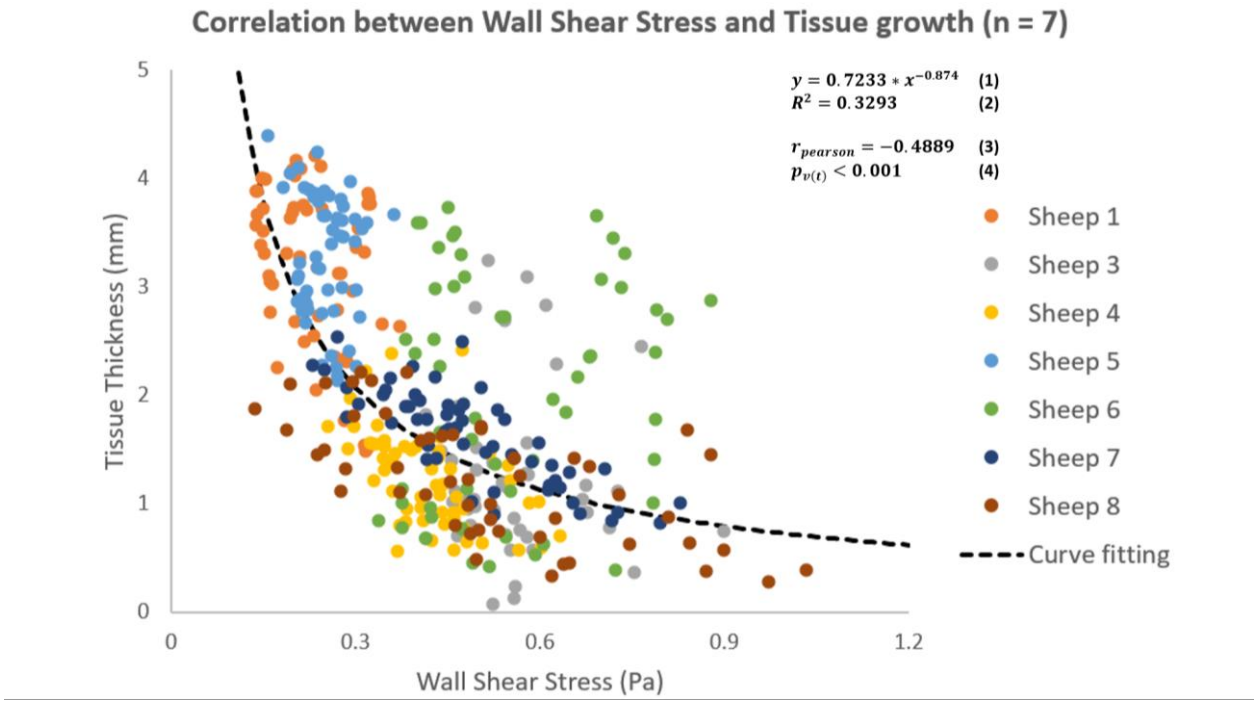

Figure 6.9 Correlation across all sheep excluding sheep No.2. A power-law curve was fitted through sheep data as shown in equation (1). R-square value in (2) indicated a moderate level of fit for the power law equation. A negative correlation was found as shown in (3) and (4).

6.5 Discussion

This is the first study to examine blood flow through a venous implant and define the correlation between venous haemodynamics and venous tissue growth pattern. One major contribution of the study is the power-law correlation between Wall Shear Stress and venous tissue growth. The correlation provides a baseline neointimal growth driven by blood flow for venous stents. The baseline allows comparison with future stent designs to optimize hemodynamic impact for endovascular implants in a venous environment. Furthermore, the thesis demonstrated a promising framework for anticipating tissue responses after venous implantation. The matching between Wall Shear Stress and tissue growth patterns opens an opportunity for efficient tissue growth forecasting, which has clinical relevance in hyperplasia monitoring and future venous implant evaluation.

6.5.1 The power law correlation is the building block for venous implants tissue response.

The power law correlation between Wall Shear Stress and venous tissue growth (Figure 6.9) has filled the missing literature gap in understanding venous neointimal hyperplasia. Currently, there has been little investigation of haemodynamics of venous stents. With rapidly growing interest in neurovascular stimulation through the cerebral and jugular venous blood vessels (Liu et al., 2023; Opie et al., 2019), understanding the impact of endovascular devices on venous structures is paramount. However, data regarding healthy venous sinuses are limited due to the infrequency of

surgical interventions in these regions. Relying on data from diseased arteries and veins that are prone to high blood pressure, thrombosis, and prolonged healing may not provide insight of normal tissue response in a healthy vein. Previously, tissue growth was observed in the superior sagittal sinus after the implantation of stent electrode arrays (John et al., 2022) in healthy sheep. The tissue growth patterns were non-uniform across the stented region and were geometrically different from focal arterial in-stent stenosis. Blood flow was first identified as an influential factor but due to limited experimental data, it has not been thoroughly investigated.

The study closely examined the tissue response from a healthy blood vessel to better understand the tissue growth patterns in the targeted veins. The presented study has linked venous tissue growth and blood flow, which has filled the research gap in venous tissue growth. The validated CFD model showed that the non-uniform tissue growth was correlated with the complex venous flow and WSS patterns. The WSS patterns were different to the patterns in plaque-induced stenosed arteries, where the WSS was always greater than 5 Pa. The thesis showed that, in healthy veins, there was no WSS higher than 1 Pa to induce plaque formation, and a low WSS less than 0.3 Pa could induce more tissue growth. The findings have provided supporting experimental data that is more specific to endovascular neural interfaces, enabling a reliable and efficient way to evaluate the hemodynamic impact and tissue growth for future endovascular neural interfaces. Since blood flow is a major factor affecting tissue growth patterns, WSS should be calculated when studying venous tissue growth patterns, especially for healthy blood vessels, which is the target of stent-based neural interfaces. Therefore, this power law correlation that the study found will lay a firm foundation for research and in-silico testing related to tissue response and long-term stability of stent-electrode devices in venous systems in the brain and around the neck.

In addition, by monitoring blood flow and WSS patterns and their changes over time, people can evaluate the impact of not only endovascular neural interfaces, but also other venous implants on promoting tissue growth. For example, for regions with a WSS less than approximately 0.3 Pa, the tissue growth could be more than double of the amount compared to middle and high WSS regions (Figure 6.9). This is slightly different to what has been observed in arteries, which is 0.5 Pa. The difference might be due to the difference in the flow condition. This insight will provide a baseline for what might happen for not only stent-electrode array but also other venous implants in the venous sinuses and the level of tissue growth expected for venous devices. In the past decade, venous neointimal hyperplasia has been reported in fragments but is gaining more interest recently, including neointimal hyperplasia in haemodialysis catheters, iliac stents, pacemaker leads, and vein grafts (Jia et al., 2015; Lonyai, Dubin, Feinstein, Taylor, & Shadden, 2010; Lucas et al., 2014; Saleem & Raju, 2022), Unfortunately, due to limited study size, lack of blood flow measurements, and difficulties in observing the in-vivo tissue response, there has been insufficient data to quantify the link between venous blood flow and venous tissue growth. As a result, researchers are still gaining insights from arteries even though the flow conditions and tissue growth response to WSS are different, leading to over or under-estimation of tissue growth for venous implants. The findings have provided the underlying negative relationship specifically between venous blood flow and venous tissue response. The relationship can support analysis of blood flow and tissue growth for other venous implants, enabling future research in veins.

6.5.2 Venous tissue growth forecasting with early haemodynamics patterns.

Comparisons between Wall Shear Stress patterns on Day 0 and the resultant tissue growth patterns on Day 28 (Figure 6.8A and 6.8B) showed similar patterns. It has also been found that the WSS on Day 0 was negatively correlated with the tissue growth over 4 weeks (Figure 6.9). The CFD results imply a potential to forecast neointimal overgrowth with WSS patterns. Prediction of neointimal hyperplasia at an early stage can reduce stent complications and improve treatment outcomes (Alraies et al., 2017). In the literature, CFD has been used extensively in arterial blood vessels to visualize complex blood flow patterns to assess the risks of blood vessel diseases (Murphy & Boyle, 2010). However, there is limited literature in forecasting tissue growth patterns using CFD results due to the complex biological process involved in blood vessel diseases. This means that, although one can anticipate more tissue growth in some low WSS regions for venous implants, it is challenging to quantitatively evaluate the impact of venous implants to make any design suggestions and management strategies for stent-electrode devices and other venous implants.

The current method of analysis remains solely on linear regression of data points. In venous literature, people are gaining insights from arterial studies to assess the risks of thrombosis and stenosis (Chen et al., 2022; Hu et al., 2024; Raza et al., 2020), but there is a knowledge gap in how venous tissue growth can be predicted. No clinical or experimental data support the predictions. However, the thesis showed that the WSS patterns may aid prediction of hyperplasia. With patient blood vessel geometry and blood flow velocity, a computational model of the individual at the day of stenting can shed light upon the potential stenting outcome in the veins. The presented work provided an efficient framework to reconstruct individualized blood vessel model, calculating the WSS pattern, and categorizing them into low, mid, and high WSS regions for tissue growth prediction in the stented jugular vein. With patient data becoming available for venous stent, it is possible to generate patient models based on the presented method, which has the potential to be further developed and utilized for surgical planning and decision on early intervention.

6.5.3 Consequences of venous stenting for endovascular neural interfaces

Venous stenting holds promise as a platform for endovascular neural interfaces. The study investigated neointimal hyperplasia using venography and micro-CT scans. None of the cases showed severe stenosis (greater than 50% narrowing) or thrombosis (Figure 6.7). In addition, no device migration was observed after Day 7 of implantation, and vessel patency was confirmed on Day 28. However, one case (sheep No.2) exhibited focal narrowing with a 40% diameter reduction, which requires further investigation.

Overall, venous stents showed ease of implantation with a much lower risk of complications compared to the conventional craniotomy approach in neuromodulation. In fact, reported complication rates for venous stenting (6.7%) were much lower than those for cortical electrode arrays (12.7%) and open brain surgery (9.1%) (Oropallo & Andersen, 2023; Schmidt et al., 2016; Wong et al., 2009), making the venous approach safer for neuromodulation.

However, lead failure, lead-related neointimal hyperplasia and lead-related thrombosis should not be overlooked for the state-of-art stent-electrode array, which remains a crucial topic. There has been no clinical evidence for stent-electrode arrays regarding lead-related complications. In this case, computational fluid dynamics models could potentially be utilized for evaluating thrombogenicity and optimizing future designs.

Furthermore, the computational models established are powerful tools to quickly evaluate the impact of future novel stent-electrode arrays. Researchers are investigating novel designs to improve device safety and performance, such as wireless transmission coils for eliminating lead problems, alternative materials to reduce inflammatory response, and novel endovascular devices to target deeper brain regions (Aldaoud et al., 2018; Dilevicius et al., 2022; Llinás et al., 2005; Tai et al., 2023; Zhang et al., 2023). In the above topics, evaluating haemodynamics is fundamental since the mechanical environment affects the tissue response. The computational models established can pave the way for future research in device evaluation.

6.5.4 Limitations and future work

The current study has several assumptions. The presented study used a commercially available nitinol venous stent. No electrode or other augmented features or novel design parameters were included in the study due to the difficulties in obtaining or manufacturing those devices. However, the presented work still has value for future study on venous implants. Novel endovascular devices that target veins are mostly adapting existing commercially available venous stents, such as the Stentrode™ device (Raza et al., 2020). The correlation results established a baseline control standard blood flow and tissue growth patterns for traditional venous stents, and this could be used to compare with the performance of any developing novel venous devices in the future. In the future, it would be ideal to implant electrode-mounting venous stents in the jugular and superior sagittal sinus to look at the effect of adding those electrodes, wires and leads. In addition, the effect of different anatomical shapes of the venous sinuses on blood flow and subsequent tissue growth patterns can also be evaluated. The tissue growth patterns, where a narrower lumen was found near inlet and outlet, has important implication on stent design. Thus, it is beneficial to test design factors, such as open or close end stent design for the novel stent device and evaluate the impact of novel designs on the haemodynamics and subsequent tissue growth.

Ideally, a larger cohort size with a longer period of monitoring is needed to collect more data and gain insights into the long-term stability of venous stents. However, this will require much more time and resources. There is an existing study that looked at venous tissue growth patterns for a period of up to 6 months (Oxley, Opie, John, et al., 2016) but, unfortunately, blood flow data was missing in the study. The main purpose of this study was to visualize blood flow patterns and define its correlation with tissue thickness. In the future, it is crucial to keep a record of the blood flow changes and utilize blood flow as a critical indicator for measuring hemodynamic impact and neointimal growth.

CFD models will be the essential research tool to gain a better understanding of the correlation in the long term and explore potential ways to optimize venous implant designs for lower hemodynamic impact. In addition, with neural networks and artificial intelligence, the current method may be further developed to forecast tissue growth more efficiently and effectively. There could be a new opportunity to forecast neointimal growth using geometry and WSS as the input parameters. With more data from animal experiments and clinical trials, a new direction is foreseeable using blood flow and WSS to aid surgical planning and early intervention strategies for future venous implants.

Reconstructing complex stent geometry remains challenging due to noise and stent metal artifact. Thus, the details of stent geometry were not modelled. Instead, the stent on the blood vessel wall

was smoothed to estimate the actual geometry. Despite the challenge, the study validated the geometry by comparing the reconstruction from 2D venogram versus high resolution micro-CT imaging. The blood vessel took a circular shape after the stent had been incorporated by endothelialisation. The estimated area from COMSOL is within 5% deviation compared to the actual area captured by micro-CT. In addition, previous study found that due to the small strut size and slow blood flow rate, the stent struts only affect blood flow and WSS in regions immediately adjacent to the stent struts (Qi et al., 2023). This is different to arterial stents, which reopen the occluded blood vessels. Arterial stent struts have a more profound influence on the WSS patterns due to large strut size. Venous stents have a smaller strut size; with a low pulsatile, low flow rate environment, the effect of stent struts is negligible. Future works aim to utilize alternative techniques, such as contrast-enhanced CT venography, to reconstruct the 3D stent geometry.

The blood vessel wall was considered to be rigid for all the CFD simulations. This means that the blood vessel wall will not expand or shrink with periodic blood flow. This is a valid assumption for stented blood vessels across numerous studies (Assi et al., 2023; Botar et al., 2010; Chen et al., 2023) because the stented region is much stiffer. However, for the unstented region, this assumption will need further testing. To simulate vessel wall deformation during the cardiac cycle, a fluid-structure interaction technique will need to be used to couple the deformation of blood vessel wall caused by the blood pressure changes and the blood flow changes driven by blood vessel dilation or constriction. This will significantly increase the computational complexity, requiring accurate material information of the venous wall and validation for the blood vessel wall movement, which is currently lacking in literature for venous blood vessels. Future work can be done to better understand the effects of venous wall deformation on haemodynamics.

6.6 Chapter summary

There has been a growing interest in using venous stents as smart devices to record and stimulate the brain from healthy blood vessels. However, neointimal hyperplasia can affect the stenting outcome in the veins. Evidence from arterial stents showed that neointimal hyperplasia affects blood flow but arterial flow rates, blood vessels, biomechanical environments and associated boundary conditions vary and are not able to explain the complex tissue growth patterns in the venous sinus. The thesis studied the correlation between Wall Shear Stress patterns and subsequent tissue growth patterns over 4 weeks after venous stent implantation. A negative power law correlation was found where a low Wall Shear Stress promoted tissue growth in the stented veins. Blood flow was identified as a critical indicator for subsequent tissue growth and should be used to monitor the impact of venous stents and future venous implants. Results also showed that venous tissue growth can be forecasted with early hemodynamic patterns. The tissue growth patterns in veins were more varied than the focal narrowing observed in stented arteries, and the threshold of low Wall Shear Stress that accelerated tissue growth was smaller than what has been reported in arteries. Venous stenting holds promise as a platform for endovascular neural interfaces and the present study filled the missing literature gap in understanding the effects of venous stenting on neointimal hyperplasia in veins. The computational models this chapter established can pave the way for future research in venous endovascular neural implant evaluation.

Chapter 7 – Concluding Remarks

7.1 Contributions

This work has demonstrated for the first time the interaction between stent haemodynamics and cerebral blood vessel shape. As the literature suggests, there is a lack of modelling and experimental works to understand the impact of venous stenting. Furthermore, the critical design parameters that minimize the haemodynamic impact of stent-electrode arrays are unclear. Without knowing how venous stents change blood flow and promote tissue growth, it is challenging to develop the stent-electrode arrays and mitigate excessive tissue growth after device implantation. The thesis fills the literature gap in venous sinus stenting.

The thesis explores the influence of critical stent design parameters and blood vessel anatomical features on the haemodynamics of endovascular neural interfaces. The study reveals that stent haemodynamics is significantly affected by the shape of the blood vessel, suggesting a correlation between hemodynamic patterns and long-term vessel narrowing in sheep. These findings represent a foundational contribution, addressing a significant gap in the literature regarding blood flow through endovascular neural interfaces. Additionally, the study identifies locations prone to accelerated tissue growth, offering insights for the development of future interfaces. This chapter establishes a fundamental framework and workflow for a Computational Fluid Dynamics (CFD) model of the stent-mounted neural interface, with the potential for expansion to study other target blood vessels for neuromodulation efficiently.

The thesis has demonstrated the need to customize endovascular neural interfaces that match the blood vessel geometry and wall deformation patterns*.* Building upon the findings of Chapter 4, Chapter 5 incorporates material properties into the computational model to assess blood vessel wall and stent deformation under different oversizing parameters. The results indicate that blood vessel wall deformation leads to lower-than-expected wall shear stress, and blood vessel tapering can result in variable blood flow patterns, influencing tissue growth. These insights are crucial for selecting the appropriate stent size for vein implantation, given the unique characteristics of veins compared to arteries. Moreover, Chapter 5 develops a powerful and comprehensive computational model for veins, considering the mechanical properties of the blood vessel wall, a novel approach in CFD modelling of veins. This model provides a reliable platform for studying the mechanical interaction between stent struts and the blood vessel wall, offering valuable insights into the condition and performance of the venous blood vessel wall, as well as the design requirements of the stent-electrode array, such as mechanical strength and fatigue.

The thesis has provided valuable experimental data for venous stents haemodynamics and tissue remodelling*.* Chapter 6 applies the insights gained from the study of blood flow impact by constructing animal-specific models validated by experiments. This chapter contributes valuable experimental data that establishes a negative power law correlation between blood flow and tissue growth, filling a gap in the literature on venous neointimal growth. It establishes a baseline for future comparisons with venous stent and endovascular neural interface designs, facilitating the evaluation of implant impacts. Furthermore, Chapter 6 indicates the potential to predict venous tissue growth using the established computational model, which could aid in surgical planning and early intervention to minimize tissue growth and the risk of severe narrowing.

In summary, this thesis has established numerous models that provide valuable insights into the hemodynamic impact and understanding of tissue growth patterns of venous stents and endovascular neural interfaces. The contribution is substantial, particularly as more implants utilize traditional stent technology for various purposes. In-silico testing of venous implants can expedite the design process and reduce prototyping costs, with testing results from computer simulations now recognized by government bodies such as the Food and Drug Administration (FDA). The models established in this thesis offer a credible and cost-efficient platform for testing and evaluating the designs of future venous implants, as well as testing devices in different blood vessels at various locations in the human body.

7.2 Future directions

The thesis provides a comprehensive study of blood flow in endovascular neural interfaces. While the device has some impact on blood flow and tissue growth, it offers a safer alternative to conventional cortical electrodes, which require open brain surgery and direct contact with brain tissue. Venous stents and stent-electrode arrays demonstrate ease of implantation with a significantly lower risk of complications compared to the conventional craniotomy approach in neuromodulation. However, future research should focus on studying the safety of stent-electrode arrays, such as lead (wire) related tissue growth and thrombosis. This thesis has shown that there was space for improving the endovascular stent-electrode array for a better treatment outcome. The thesis has demonstrated and validated that blood flow was closely related to vascular health post-implantation. This suggests that by reducing the blood flow impact of stent-electrode, risks of complications could be reduced. The computational model, as well as the experimental methodology, lays the foundation for future endovascular neural interfaces and safety testing of new stent prototypes. The computational and experimental methods capture the entire process of endovascular stent implantation, from stent deployment to tissue remodelling during post-stenting patient recovery. This can be used for testing and evaluating new stent designs with high efficiency and accuracy.

The future direction of endovascular neural interfaces involves improving device design to minimize changes in blood flow and tissue growth. Computational models established in this thesis, along with experimental results, evaluate the blood flow impact of endovascular neural interfaces and explain complex tissue growth patterns. Future research should aim to reduce the blood flow impact and potential tissue growth, thereby minimizing the risk of severe narrowing in blood vessels. Pursuing new stent patterns that optimize wall shear stress or developing individualized stents that fit tortuous and tapering blood vessels better could be promising directions. While the thesis did not develop novel stent patterns, future research could focus on generating new stent design patterns and features to improve outcomes and reduce the rate of venous neointimal hyperplasia.

Another research direction involves forecasting and predicting tissue growth in blood vessels. The thesis demonstrates that blood flow is a major contributor to accelerated tissue growth, suggesting the potential use of blood flow results to predict tissue growth patterns. Tissue growth is a complex biological process involving various stages of cell metabolism and biochemical interactions, making it challenging to predict. However, with the ability to predict tissue growth shown in this work, it is possible to evaluate the long-term performance of venous implants. This may also aid in surgical planning and early intervention using a digital twin, which offers virtual implantation of venous implants and simulation of tissue growth based on patient data. Advancements in digital twins and

artificial neural networks may enable the prediction of complex tissue growth patterns. Future research could focus on improving the accuracy of predicting tissue growth in stented veins, allowing for more precise evaluation of device risk and better surgical plans for individual patients.

Bibliography

Acuna, A., Berman, A. G., Damen, F. W., Meyers, B. A., Adelsperger, A. R., Bayer, K. C., Brindise, M. C., Bungart, B., Kiel, A. M., Morrison, R. A., Muskat, J. C., Wasilczuk, K. M., Wen, Y., Zhang, J., Zito, P., & Goergen, C. J. (2018). Computational Fluid Dynamics of Vascular Disease in Animal Models. *Journal of Biomechanical Engineering*, *140*(8), 0808011–08080114. PubMed. https://doi.org/10.1115/1.4039678

Adderley, N. J., Subramanian, A., Nirantharakumar, K., Yiangou, A., Gokhale, K. M., Mollan, S. P., & Sinclair, A. J. (2019). Association Between Idiopathic Intracranial Hypertension and Risk of Cardiovascular Diseases in Women in the United Kingdom. *JAMA Neurology*, *76*(9), 1088–1098. PubMed. https://doi.org/10.1001/jamaneurol.2019.1812

Aldaoud, A., Redoute, J.-M., Ganesan, K., Rind, G. S., John, S. E., Ronayne, S. M., Opie, N. L., Garrett, D. J., & Prawer, S. (2018). Near-Field Wireless Power Transfer to Stent-Based Biomedical Implants. *IEEE Journal of Electromagnetics, RF and Microwaves in Medicine and Biology*, *2*(3), 193–200. https://doi.org/10.1109/jerm.2018.2833386

Alraies, M. C., Darmoch, F., Tummala, R., & Waksman, R. (2017). Diagnosis and management challenges of in-stent restenosis in coronary arteries. *World Journal of Cardiology*, *9*(8), 640–651. PubMed. https://doi.org/10.4330/wjc.v9.i8.640

Antoniadis, A. P., Mortier, P., Kassab, G., Dubini, G., Foin, N., Murasato, Y., Giannopoulos, A. A., Tu, S., Iwasaki, K., Hikichi, Y., Migliavacca, F., Chiastra, C., Wentzel, J. J., Gijsen, F., Reiber, J. H. C., Barlis, P., Serruys, P. W., Bhatt, D. L., Stankovic, G., … Chatzizisis, Y. S. (2015). Biomechanical Modeling to Improve Coronary Artery Bifurcation Stenting. *JACC: Cardiovascular Interventions*, *8*(10), 1281–1296. https://doi.org/10.1016/j.jcin.2015.06.015

Assi, I. Z., Lynch, S. R., Samulak, K., Williams, D. M., Wakefield, T. W., Obi, A. T., & Figueroa, C. A. (2023). An ultrasound imaging and computational fluid dynamics protocol to assess hemodynamics in iliac vein compression syndrome. *Journal of Vascular Surgery: Venous and Lymphatic Disorders*, *11*(5), 1023-1033.e5. https://doi.org/10.1016/j.jvsv.2023.05.017

Baaten, C. C. F. M. J., Nagy, M., Bergmeier, W., Spronk, H. M. H., & van der Meijden, P. E. J. (2024). Platelet biology and function: Plaque erosion vs. Rupture. *European Heart Journal*, *45*(1), 18–31. PubMed. https://doi.org/10.1093/eurheartj/ehad720

Ballout, A. A., Prochilo, G., Kaneko, N., Li, C., Apfel, R., Hinman, J. D., & Liebeskind, D. S. (2024). Computational Fluid Dynamics in Intracranial Atherosclerotic Disease. *Stroke: Vascular and Interventional Neurology*, *4*(1). https://doi.org/10.1161/svin.122.000792

Bartlett, M., Bonfanti, M., Diaz-Zuccarini, V., & Tsui, J. (2024). Computationally Enhanced, Haemodynamic Case Study of Neointimal Hyperplasia Development in a Dialysis Access Fistula. *Reviews in Cardiovascular Medicine*, *25*(1), 35. https://doi.org/10.31083/j.rcm2501035

Bateman, A. R., Bateman, G. A., & Barber, T. (2021). The relationship between cerebral blood flow and venous sinus pressure: Can hyperemia induce idiopathic intracranial hypertension? *Fluids and Barriers of the CNS*, *18*(1), 5–5. PubMed. https://doi.org/10.1186/s12987-021-00239-2

Baytore, C., Palandoken, M., & Kaya, A. (2016, November). *Shape memory Alloy NiTi antenna with WiFi application: 2.4/5.8 GHz dual band, shape memory Alloy equatomic NiTi (Nitinol) planar metal plate antenna with a WiFi application in built-in oven with metal housing effect*. 2016

16th Mediterranean Microwave Symposium (MMS). https://doi.org/10.1109/mms.2016.7803859

Beer-Furlan, A., Munich, S. A., & Chen, M. (2020). Augmenting superior sagittal sinus functionality. Commentary: Motor neuroprosthesis implanted with neurointerventional surgery improves capacity for activities of daily living tasks in severe paralysis—First in human experience. *Journal of NeuroInterventional Surgery*, *13*(2), 100–101. https://doi.org/10.1136/neurintsurg-2020-017074

Beier, S., Ormiston, J., Webster, M., Cater, J., Norris, S., Medrano-Gracia, P., Young, A., & Cowan, B. (2016). Hemodynamics in Idealized Stented Coronary Arteries: Important Stent Design Considerations. *Annals of Biomedical Engineering*, *44*(2), 315–329. PubMed. https://doi.org/10.1007/s10439-015-1387-3

Bernard, S., Newell, K., & Tubbs, R. S. (2020). The Superior Sagittal Sinus. *Anatomy, Imaging and Surgery of the Intracranial Dural Venous Sinuses*, 9–27. https://doi.org/10.1016/b978-0-323-65377-0.00002-7

Bernini, M., Colombo, M., Dunlop, C., Hellmuth, R., Chiastra, C., Ronan, W., & Vaughan, T. J. (2022). Oversizing of self-expanding Nitinol vascular stents – A biomechanical investigation in the superficial femoral artery. *Journal of the Mechanical Behavior of Biomedical Materials*, *132*, 105259. https://doi.org/10.1016/j.jmbbm.2022.105259

Berry, J. L., Santamarina, A., Moore, Jr., James E., Roychowdhury, S., & Routh, W. D. (2000). Experimental and Computational Flow Evaluation of Coronary Stents. *Annals of Biomedical Engineering*, *28*(4), 386–398. https://doi.org/10.1114/1.276

Boddu, S. R., Gobin, P., Oliveira, C., Dinkin, M., & Patsalides, A. (2018). Anatomic measurements of cerebral venous sinuses in idiopathic intracranial hypertension patients. *PloS One*, *13*(6), e0196275–e0196275. PubMed. https://doi.org/10.1371/journal.pone.0196275

Boghosian, M. E., Hammes, M. S., Cassel, K. W., Akherat, S. M. J., & Coe, F. (2018). Restoration of wall shear stress in the cephalic vein during extreme hemodynamics. *Journal of Medical Engineering & Technology*, *42*(8), 617–627. PubMed. https://doi.org/10.1080/03091902.2019.1591534

Botar, C. C., Vasile, T., Sfrangeu, S., Clichici, S., Agachi, P. S., Badea, R., Mircea, P., & Cristea, M. V. (2010). Validation of CFD simulation results in case of portal vein blood flow. *Computer Aided Chemical Engineering*, 205–210. https://doi.org/10.1016/s1570-7946(10)28035-5

Bower, M. R., Stead, M., Van Gompel, J. J., Bower, R. S., Sulc, V., Asirvatham, S. J., & Worrell, G. A. (2013). Intravenous recording of intracranial, broadband EEG. *Journal of Neuroscience Methods*, *214*(1), 21–26. PubMed. https://doi.org/10.1016/j.jneumeth.2012.12.027

Brinjikji, W., Mark, I. T., Silvera, V. M., & Guerin, J. B. (2020). Cervicofacial Venous Malformations Are Associated with Intracranial Developmental Venous Anomalies and Dural Venous Sinus Abnormalities. *AJNR. American Journal of Neuroradiology*, *41*(7), 1209–1214. PubMed. https://doi.org/10.3174/ajnr.A6617

Buccheri, D., Piraino, D., Andolina, G., & Cortese, B. (2016). Understanding and managing in-stent restenosis: A review of clinical data, from pathogenesis to treatment. *Journal of Thoracic Disease*, *8*(10), E1150–E1162. PubMed. https://doi.org/10.21037/jtd.2016.10.93

Campolo, J., Vozzi, F., Penco, S., Cozzi, L., Caruso, R., Domenici, C., Ahluwalia, A., Rial, M., Marraccini, P., & Parodi, O. (2014). Vascular injury post stent implantation: Different gene

expression modulation in human umbilical vein endothelial cells (HUVECs) model. *PloS One*, *9*(2), e90213–e90213. PubMed. https://doi.org/10.1371/journal.pone.0090213

Casa, L. D. C., Deaton, D. H., & Ku, D. N. (2015). Role of high shear rate in thrombosis. *Journal of Vascular Surgery*, *61*(4), 1068–1080. https://doi.org/10.1016/j.jvs.2014.12.050

Chaabane, C., Otsuka, F., Virmani, R., & Bochaton-Piallat, M.-L. (2013). Biological responses in stented arteries. *Cardiovascular Research*, *99*(2), 353–363. https://doi.org/10.1093/cvr/cvt115

Chapter 5 COMSOL Multiphysics Models. (2020). *COMSOL Heat Transfer Models*, 89–126. https://doi.org/10.1515/9781683922698-007

Chen, B., Dai, H., Yang, J., Tang, K., Zhang, G., Xiang, X., Lin, R., & Huang, Y. (2022). Computational fluid dynamics simulation of hemodynamic changes in a hemodialysis patient with central venous stenosis treated with stent. *Seminars in Dialysis*, *35*(6), 528–533. https://doi.org/10.1111/sdi.13048

Chen, H.-W., Chen, C.-H., Fan, Y.-J., Lin, C.-Y., Hsu, W.-H., Su, I.-C., Lin, C.-L., Chiang, Y.-C., & Huang, H.-M. (2023). CFD Study of the Effect of the Angle Pattern on Iliac Vein Compression Syndrome. *Bioengineering (Basel, Switzerland)*, *10*(6), 688. PubMed. https://doi.org/10.3390/bioengineering10060688

Chen, W. X., Poon, E. K. W., Hutchins, N., Thondapu, V., Barlis, P., & Ooi, A. (2017). Computational fluid dynamics study of common stent models inside idealised curved coronary arteries. *Computer Methods in Biomechanics and Biomedical Engineering*, *20*(6), 671–681. https://doi.org/10.1080/10255842.2017.1289374

Chen, W. X., Poon, E. K. W., Thondapu, V., Hutchins, N., Barlis, P., & Ooi, A. (2017). Haemodynamic effects of incomplete stent apposition in curved coronary arteries. *Journal of Biomechanics*, *63*, 164–173. https://doi.org/10.1016/j.jbiomech.2017.09.016

Chen, X., Assadsangabi, B., Hsiang, Y., & Takahata, K. (2018). Medical Implants: Enabling Angioplasty-Ready "Smart" Stents to Detect In-Stent Restenosis and Occlusion (Adv. Sci. 5/2018). *Advanced Science*, *5*(5). https://doi.org/10.1002/advs.201870027

Chen, Z., Brodie, M. J., Ding, D., & Kwan, P. (2023). Editorial: Epidemiology of epilepsy and seizures. *Frontiers in epidemiology*, *3*, 1273163. https://doi.org/10.3389/fepid.2023.1273163

Chua, S. N. D., Mac Donald, B. J., & Hashmi, M. S. J. (2002). Finite-element simulation of stent expansion. *Journal of Materials Processing Technology*, *120*(1–3), 335–340. https://doi.org/10.1016/s0924-0136(01)01127-x

Collins, M. J., Li, X., Lv, W., Yang, C., Protack, C. D., Muto, A., Jadlowiec, C. C., Shu, C., & Dardik, A. (2012). Therapeutic strategies to combat neointimal hyperplasia in vascular grafts. *Expert Review of Cardiovascular Therapy*, *10*(5), 635–647. PubMed. https://doi.org/10.1586/erc.12.33

COMSOL Multiphysics® v. 5.5. www.comsol.com. COMSOL AB, Stockholm, Sweden.

Cunningham, K. S., & Gotlieb, A. I. (2005). The role of shear stress in the pathogenesis of atherosclerosis. *Laboratory Investigation*, *85*(1), 9–23. https://doi.org/10.1038/labinvest.3700215

Daggubati, L. C., & Liu, K. C. (2019). Intracranial Venous Sinus Stenting: A Review of Idiopathic Intracranial Hypertension and Expanding Indications. *Cureus*, *11*(2), e4008–e4008. PubMed. https://doi.org/10.7759/cureus.4008

Delye, H., Goffin, J., Verschueren, P., Sloten, J. V., Van der Perre, G., Alaerts, H., Verpoest, I., & Berckmans, D. (2006, November 6). *Biomechanical Properties of the Superior Sagittal Sinus-Bridging Vein Complex*. SAE Technical Paper Series. https://doi.org/10.4271/2006-22-0024

DePaola, N., Gimbrone, M. A., Davies, P. F., & Dewey, C. F. (1992). Vascular endothelium responds to fluid shear stress gradients. *Arteriosclerosis and Thrombosis: A Journal of Vascular Biology*, *12*(11), 1254–1257. https://doi.org/10.1161/01.atv.12.11.1254

Dilevicius, I., Serdijn, W. A., & Costa, T. L. (2022, July 11). *Stent with Piezoelectric Transducers for High Spatial Resolution Ultrasound Neuromodulation- a Finite Element Analysis*. 2022 44th Annual International Conference of the IEEE Engineering in Medicine & Biology Society (EMBC). https://doi.org/10.1109/embc48229.2022.9871956

Donadoni, F., Pichardo-Almarza, C., Bartlett, M., Dardik, A., Homer-Vanniasinkam, S., & Díaz-Zuccarini, V. (2017). Patient-Specific, Multi-Scale Modeling of Neointimal Hyperplasia in Vein Grafts. *Frontiers in Physiology*, *8*, 226–226. PubMed. https://doi.org/10.3389/fphys.2017.00226

Egemen, E., & Solaroglu, I. (2017). Anatomy of Cerebral Veins and Dural Sinuses. *Primer on Cerebrovascular Diseases*, 32–36. https://doi.org/10.1016/b978-0-12-803058-5.00005-9

Entezami, P., Gooch, M. R., & Dalfino, J. (2019). Endovascular stenting of the superior sagittal sinus to alleviate venous compression caused by a parasagittal meningioma. *BMJ Case Reports*, *12*(4), e227935. PubMed. https://doi.org/10.1136/bcr-2018-227935

Esmon, C. T. (2009). Basic mechanisms and pathogenesis of venous thrombosis. *Blood Reviews*, *23*(5), 225–229. PubMed. https://doi.org/10.1016/j.blre.2009.07.002

Fan, J. Z., Lopez-Rivera, V., & Sheth, S. A. (2020). Over the Horizon: The Present and Future of Endovascular Neural Recording and Stimulation. *Frontiers in Neuroscience*, *14*, 432–432. PubMed. https://doi.org/10.3389/fnins.2020.00432

Fedorov, A., Beichel, R., Kalpathy-Cramer, J., Finet, J., Fillion-Robin, J.-C., Pujol, S., Bauer, C., Jennings, D., Fennessy, F., Sonka, M., Buatti, J., Aylward, S., Miller, J. V., Pieper, S., & Kikinis, R. (2012). 3D Slicer as an image computing platform for the Quantitative Imaging Network. *Magnetic Resonance Imaging*, *30*(9), 1323–1341. PubMed. https://doi.org/10.1016/j.mri.2012.05.001

Fillingham, P., Rane Levendovszky, S., Andre, J., Bindschadler, M., Friedman, S., Kurt, M., Aliseda, A., & Levitt, M. R. (2023). Noninvasive, patient-specific computational fluid dynamics simulations of dural venous sinus pressures in idiopathic intracranial hypertension. *Brain Multiphysics, 5*, 100081. https://doi.org/10.1016/j.brain.2023.100081

Fluid–Structure Interaction with Ansys/Fluent. (2017). *Fluid-Structure Interactions and Uncertainties*, 35–57. https://doi.org/10.1002/9781119388937.ch2

Fluri, F., Bieber, M., Volkmann, J., & Kleinschnitz, C. (2015). Microelectrode Guided Implantation of Electrodes into the Subthalamic Nucleus of Rats for Long-term Deep Brain Stimulation. *Journal of Visualized Experiments : JoVE*, *104*, 53066. PubMed. https://doi.org/10.3791/53066

Foin, N., Gutiérrez-Chico, J. L., Nakatani, S., Torii, R., Bourantas, C. V., Sen, S., Nijjer, S., Petraco, R., Kousera, C., Ghione, M., Onuma, Y., Garcia-Garcia, H. M., Francis, D. P., Wong, P., Di Mario, C., Davies, J. E., & Serruys, P. W. (2014). Incomplete Stent Apposition Causes High Shear Flow Disturbances and Delay in Neointimal Coverage as a Function of Strut to Wall Detachment

Distance. *Circulation: Cardiovascular Interventions*, *7*(2), 180–189. https://doi.org/10.1161/circinterventions.113.000931

Forsyth, I. A., Dunston, M., Lombardi, G., Rind, G. S., Ronayne, S., Wong, Y. T., May, C. N., Grayden, D. B., Oxley, T., Opie, N., & John, S. E. (2019, March). *Evaluation of a minimally invasive endovascular neural interface for decoding motor activity*. 2019 9th International IEEE/EMBS Conference on Neural Engineering (NER). https://doi.org/10.1109/ner.2019.8717000

Frank, A. O., Walsh, P. W., & Moore, J. E. (2002). Computational Fluid Dynamics and Stent Design. *Artificial Organs*, *26*(7), 614–621. https://doi.org/10.1046/j.1525-1594.2002.07084.x

Friedman, M. H., Bargeron, C. B., Deters, O. J., Hutchins, G. M., & Mark, F. F. (1987). Correlation between wall shear and intimal thickness at a coronary artery branch. *Atherosclerosis*, *68*(1–2), 27–33. https://doi.org/10.1016/0021-9150(87)90090-6

Gijsen, F., Katagiri, Y., Barlis, P., Bourantas, C., Collet, C., Coskun, U., Daemen, J., Dijkstra, J., Edelman, E., Evans, P., van der Heiden, K., Hose, R., Koo, B.-K., Krams, R., Marsden, A., Migliavacca, F., Onuma, Y., Ooi, A., Poon, E., … Serruys, P. (2019). Expert recommendations on the assessment of wall shear stress in human coronary arteries: Existing methodologies, technical considerations, and clinical applications. *European Heart Journal*, *40*(41), 3421–3433. PubMed. https://doi.org/10.1093/eurheartj/ehz551

Göbl, R., Virga, S., Rackerseder, J., Frisch, B., Navab, N., & Hennersperger, C. (2017). Acoustic window planning for ultrasound acquisition. *International Journal of Computer Assisted Radiology and Surgery*, *12*(6), 993–1001. PubMed. https://doi.org/10.1007/s11548-017-1551-3

Gordon, D., Williams, D., & Nicklas, J. (2021). Human Vein In-Stent Restenosis: A Clinic-Pathologic Study. *Journal of Vascular Surgery: Venous and Lymphatic Disorders*, *9*(2), 547–548. https://doi.org/10.1016/j.jvsv.2020.12.034

Gundert, T. J., Marsden, A. L., Yang, W., & LaDisa, J. F. (2012). Optimization of Cardiovascular Stent Design Using Computational Fluid Dynamics. *Journal of Biomechanical Engineering*, *134*(1). https://doi.org/10.1115/1.4005542

Gundert, T. J., Shadden, S. C., Williams, A. R., Koo, B.-K., Feinstein, J. A., & LaDisa, J. F. (2011). A Rapid and Computationally Inexpensive Method to Virtually Implant Current and Next-Generation Stents into Subject-Specific Computational Fluid Dynamics Models. *Annals of Biomedical Engineering*, *39*(5), 1423–1437. https://doi.org/10.1007/s10439-010-0238-5

Hajati, Z., Sadegh Moghanlou, F., Vajdi, M., Razavi, S. E., & Matin, S. (2020). Fluid-structure interaction of blood flow around a vein valve. *BioImpacts : BI*, *10*(3), 169–175. PubMed. https://doi.org/10.34172/bi.2020.21

He, R., Zhao, L., Silberschmidt, V. V., & Liu, Y. (2020). Mechanistic evaluation of long-term in-stent restenosis based on models of tissue damage and growth. *Biomechanics and Modeling in Mechanobiology*, *19*(5), 1425–1446. PubMed. https://doi.org/10.1007/s10237-019-01279-2

He, S., Liu, W., Qu, K., Yin, T., Qiu, J., Li, Y., Yuan, K., Zhang, H., & Wang, G. (2020). Effects of different positions of intravascular stent implantation in stenosed vessels on in-stent restenosis: An experimental and numerical simulation study. *Journal of Biomechanics*, *113*, 110089. https://doi.org/10.1016/j.jbiomech.2020.110089

Hingorani, A., Marks, N. and Ascher, E. (2018) 'Etiology of iliac vein stent thrombosis', *Journal of Vascular Surgery: Venous and Lymphatic Disorders*, 6(2), pp. 284–285. https://doi.org/10.1016/j.jvsv.2017.12.018

Holme, P. A., Ørvim, U., Hamers, M. J. A. G., Solum, N. O., Brosstad, F. R., Barstad, R. M., & Sakariassen, K. S. (1997). Shear-Induced Platelet Activation and Platelet Microparticle Formation at Blood Flow Conditions as in Arteries With a Severe Stenosis. *Arteriosclerosis, Thrombosis, and Vascular Biology*, *17*(4), 646–653. https://doi.org/10.1161/01.atv.17.4.646

Holmes, D. R., Kereiakes, D. J., Garg, S., Serruys, P. W., Dehmer, G. J., Ellis, S. G., Williams, D. O., Kimura, T., & Moliterno, D. J. (2010). Stent Thrombosis. *Journal of the American College of Cardiology*, *56*(17), 1357–1365. https://doi.org/10.1016/j.jacc.2010.07.016

Hoogendoorn, A., Kok, A. M., Hartman, E. M. J., de Nisco, G., Casadonte, L., Chiastra, C., Coenen, A., Korteland, S.-A., Van der Heiden, K., Gijsen, F. J. H., Duncker, D. J., van der Steen, A. F. W., & Wentzel, J. J. (2020). Multidirectional wall shear stress promotes advanced coronary plaque development: Comparing five shear stress metrics. *Cardiovascular Research*, *116*(6), 1136–1146. PubMed. https://doi.org/10.1093/cvr/cvz212

Hsiao, H.-M., Lee, K.-H., Liao, Y.-C., & Cheng, Y.-C. (2012). Cardiovascular stent design and wall shear stress distribution in coronary stented arteries. *Micro & Nano Letters*, *7*(5), 430. https://doi.org/10.1049/mnl.2011.0590

Hu, J., Feng, H., Zheng, Y., Wang, K., Wang, X., & Su, J. (2024). Mechanism of effect of stenting on hemodynamics at iliac vein bifurcation. *Computers in Biology and Medicine*, *170*, 107968. https://doi.org/10.1016/j.compbiomed.2024.107968

Islam, S., Song, X., Choi, E. T., Kim, J., Liu, H., & Kim, A. (2020). In Vitro Study on Smart Stent for Autonomous Post-Endovascular Aneurysm Repair Surveillance. *IEEE Access*, *8*, 96340–96346. https://doi.org/10.1109/access.2020.2996506

Jerjes-Sánchez, C. (2015). Mechanisms of Thrombosis. *Thrombolysis in Pulmonary Embolism*, 1–17. https://doi.org/10.1007/978-3-319-19707-4_1

Jia, L., Wang, L., Wei, F., Yu, H., Dong, H., Wang, B., Lu, Z., Sun, G., Chen, H., Meng, J., Li, B., Zhang, R., Bi, X., Wang, Z., Pang, H., & Jiang, A. (2015). Effects of wall shear stress in venous neointimal hyperplasia of arteriovenous fistulae. *Nephrology*, *20*(5), 335–342. https://doi.org/10.1111/nep.12394

Jiang, B., Thondapu, V., Poon, E. K. W., Barlis, P., & Ooi, A. S. H. (2019). Numerical Study of Incomplete Stent Apposition Caused by Deploying Undersized Stent in Arteries With Elliptical Cross Sections. *Journal of Biomechanical Engineering*, *141*(5). https://doi.org/10.1115/1.4042899

Jiménez, J. M., & Davies, P. F. (2009). Hemodynamically driven stent strut design. *Annals of Biomedical Engineering*, *37*(8), 1483–1494. PubMed. https://doi.org/10.1007/s10439-009-9719-9

John, S. E., Donegan, S., Scordas, T. C., Qi, W., Sharma, P., Liyanage, K., Wilson, S., Birchall, I., Ooi, A., Oxley, T. J., May, C. N., Grayden, D. B., & Opie, N. L. (2022). Vascular remodeling in sheep implanted with endovascular neural interface. *Journal of Neural Engineering*, *19*(5), 056043. https://doi.org/10.1088/1741-2552/ac9a77

John, S. E., Grayden, D. B., & Yanagisawa, T. (2019). The future potential of the Stentrode. *Expert Review of Medical Devices*, *16*(10), 841–843. https://doi.org/10.1080/17434440.2019.1674139

Jordan, J. E., Pelc, N. J., & Enzmann, D. R. (1994). Velocity and flow quantitation in the superior sagittal sinus with ungated and cine (gated) phase-contrast MR imaging. *Journal of Magnetic Resonance Imaging*, *4*(1), 25–28. https://doi.org/10.1002/jmri.1880040108

Katritsis, D. G., Theodorakakos, A., Pantos, I., Gavaises, M., Karcanias, N., & Efstathopoulos, E. P. (2012). Flow Patterns at Stented Coronary Bifurcations. Circulation: Cardiovascular Interventions, 5(4), 530–539. https://doi.org/10.1161/circinterventions.112.968347

Kitahara, H., Okada, K., Kimura, T., Yock, P. G., Lansky, A. J., Popma, J. J., Yeung, A. C., Fitzgerald, P. J., & Honda, Y. (2017). Impact of Stent Size Selection on Acute and Long-Term Outcomes After Drug-Eluting Stent Implantation in De Novo Coronary Lesions. *Circulation: Cardiovascular Interventions*, *10*(10). https://doi.org/10.1161/circinterventions.116.004795

Kolandaivelu, K., Swaminathan, R., Gibson, W. J., Kolachalama, V. B., Nguyen-Ehrenreich, K.-L., Giddings, V. L., Coleman, L., Wong, G. K., & Edelman, E. R. (2011). Stent thrombogenicity early in high-risk interventional settings is driven by stent design and deployment and protected by polymer-drug coatings. *Circulation*, *123*(13), 1400–1409. PubMed. https://doi.org/10.1161/CIRCULATIONAHA.110.003210

Kozai, T. D. Y., Jaquins-Gerstl, A. S., Vazquez, A. L., Michael, A. C., & Cui, X. T. (2015). Brain tissue responses to neural implants impact signal sensitivity and intervention strategies. *ACS Chemical Neuroscience*, *6*(1), 48–67. PubMed. https://doi.org/10.1021/cn500256e

Kumar, R., Varun, & Kumar, A. (2016). Thermal and fluid dynamic characteristics of flow through triangular cross-sectional duct: A review. *Renewable and Sustainable Energy Reviews*, *61*, 123–140. https://doi.org/10.1016/j.rser.2016.03.011

Kumpe, D. A., Bennett, J. L., Seinfeld, J., Pelak, V. S., Chawla, A., & Tierney, M. (2012). Dural sinus stent placement for idiopathic intracranial hypertension. *Journal of Neurosurgery*, *116*(3), 538–548. https://doi.org/10.3171/2011.10.jns101410

Kunieda, T., Ikeda, A., Mikuni, N., Ohara, S., Sadato, A., Taki, W., Hashimoto, N., & Shibasaki, H. (2000). Use of Cavernous Sinus EEG in the Detection of Seizure Onset and Spread in Mesial Temporal Lobe Epilepsy. *Epilepsia*, *41*(11), 1411–1419. https://doi.org/10.1111/j.1528-1157.2000.tb00116.x

Kwak, B. R., Bäck, M., Bochaton-Piallat, M.-L., Caligiuri, G., Daemen, M. J. A. P., Davies, P. F., Hoefer, I. E., Holvoet, P., Jo, H., Krams, R., Lehoux, S., Monaco, C., Steffens, S., Virmani, R., Weber, C., Wentzel, J. J., & Evans, P. C. (2014). Biomechanical factors in atherosclerosis: Mechanisms and clinical implications. *European Heart Journal*, *35*(43), 3013–3020d. PubMed. https://doi.org/10.1093/eurheartj/ehu353

LaDisa, J. F., Jr, Olson, L. E., Hettrick, D. A., Warltier, D. C., Kersten, J. R., & Pagel, P. S. (2005). Axial stent strut angle influences wall shear stress after stent implantation: Analysis using 3D computational fluid dynamics models of stent foreshortening. *Biomedical Engineering Online*, *4*, 59–59. PubMed. https://doi.org/10.1186/1475-925X-4-59

LaDisa, J. F., Olson, L. E., Guler, I., Hettrick, D. A., Audi, S. H., Kersten, J. R., Warltier, D. C., & Pagel, P. S. (2004). Stent design properties and deployment ratio influence indexes of wall shear stress: A three-dimensional computational fluid dynamics investigation within a normal

artery. *Journal of Applied Physiology*, *97*(1), 424–430. https://doi.org/10.1152/japplphysiol.01329.2003

LaDisa, J. F., Olson, L. E., Guler, I., Hettrick, D. A., Kersten, J. R., Warltier, D. C., & Pagel, P. S. (2005). Circumferential vascular deformation after stent implantation alters wall shear stress evaluated with time-dependent 3D computational fluid dynamics models. *Journal of Applied Physiology*, *98*(3), 947–957. https://doi.org/10.1152/japplphysiol.00872.2004

LaDisa, J. F., Olson, Lars. E., Molthen, R. C., Hettrick, D. A., Pratt, P. F., Hardel, M. D., Kersten, J. R., Warltier, D. C., & Pagel, P. S. (2005). Alterations in wall shear stress predict sites of neointimal hyperplasia after stent implantation in rabbit iliac arteries. *American Journal of Physiology-Heart and Circulatory Physiology*, *288*(5), H2465–H2475. https://doi.org/10.1152/ajpheart.01107.2004

LaDisa, Jr., John F., Guler, I., Olson, L. E., Hettrick, D. A., Kersten, J. R., Warltier, D. C., & Pagel, P. S. (2003). Three-Dimensional Computational Fluid Dynamics Modeling of Alterations in Coronary Wall Shear Stress Produced by Stent Implantation. *Annals of Biomedical Engineering*, *31*(8), 972–980. https://doi.org/10.1114/1.1588654

Larson, A. S., Lanzino, G., & Brinjikji, W. (2020). Variations of Intracranial Dural Venous Sinus Diameters from Birth to 20 Years of Age: An MRV-Based Study. *AJNR. American Journal of Neuroradiology*, *41*(12), 2351–2357. PubMed. https://doi.org/10.3174/ajnr.A6816

Lee, S.-Y., & Hong, M.-K. (2016). Mechanisms of stent thrombosis: Insights from optical coherence tomography. *Journal of Thoracic Disease*, *8*(6), E460–E462. PubMed. https://doi.org/10.21037/jtd.2016.04.31

Leong, S., & Lee, T. (2020). The Internet in Singapore: From 'Intelligent Island' to 'Smart Nation.' *Global Internet Governance*, 31–49. https://doi.org/10.1007/978-981-15-9924-8_3

Levitt, M. R., McGah, P. M., Moon, K., Albuquerque, F. C., McDougall, C. G., Kalani, M. Y. S., Kim, L. J., & Aliseda, A. (2016). Computational Modeling of Venous Sinus Stenosis in Idiopathic Intracranial Hypertension. *AJNR. American Journal of Neuroradiology*, *37*(10), 1876–1882. PubMed. https://doi.org/10.3174/ajnr.A4826

Liu, J. Y., Grayden, D. B., Keast, J. R., & John, S. E. (2023). Computational modeling of endovascular peripheral nerve stimulation using a stent-mounted electrode array. *Journal of Neural Engineering*, *20*(3), 036013. https://doi.org/10.1088/1741-2552/aca69e

Liu, X., Du, Z., Han, T., Ghista, D. N., Lin, S., Wang, V., Wang, J., Zhang, H., & Pan, Z. (2019). Quantitative Analysis of Blood Flow in Cerebral Venous Sinus With Stenosis by Patient-Specific CFD Modeling. *IEEE Access*, *7*, 3848–3854. https://doi.org/10.1109/access.2018.2888490

Liu, X., Zhang, W., Ye, P., Luo, Q., & Chang, Z. (2022). Mechanical and hydrodynamic effects of stent expansion in tapered coronary vessels. *Biomechanics and Modeling in Mechanobiology*, *21*(5), 1549–1560. PubMed. https://doi.org/10.1007/s10237-022-01605-1

Llinás, R. R., Walton, K. D., Nakao, M., Hunter, I., & Anquetil, P. A. (2005). Neuro-vascular central nervous recording/stimulating system: Using nanotechnology probes. *Journal of Nanoparticle Research*, *7*(2–3), 111–127. https://doi.org/10.1007/s11051-005-3134-4

Lonyai, A., Dubin, A. M., Feinstein, J. A., Taylor, C. A., & Shadden, S. C. (2010). New Insights into Pacemaker Lead-Induced Venous Occlusion: Simulation-Based Investigation of Alterations in

Venous Biomechanics. *Cardiovascular Engineering*, *10*(2), 84–90. https://doi.org/10.1007/s10558-010-9096-x

Lorenzini, G., & Casalena, E. (2008). CFD analysis of pulsatile blood flow in an atherosclerotic human artery with eccentric plaques. *Journal of Biomechanics*, *41*(9), 1862–1870. https://doi.org/10.1016/j.jbiomech.2008.04.009

Lucas, T. C., Tessarolo, F., Jakitsch, V., Caola, I., Brunori, G., Nollo, G., & Huebner, R. (2013). Blood Flow in Hemodialysis Catheters: A Numerical Simulation and Microscopic Analysis of In Vivo-Formed Fibrin. *Artificial Organs*, *38*(7), 556–565. https://doi.org/10.1111/aor.12243

Mackman, N. (2012). New insights into the mechanisms of venous thrombosis. *The Journal of Clinical Investigation*, *122*(7), 2331–2336. PubMed. https://doi.org/10.1172/JCI60229

Martin, D. M., Murphy, E. A., & Boyle, F. J. (2014). Computational fluid dynamics analysis of balloon-expandable coronary stents: Influence of stent and vessel deformation. *Medical Engineering & Physics*, *36*(8), 1047–1056. https://doi.org/10.1016/j.medengphy.2014.05.011

Matsuda, A., Yamada, N., Ogihara, Y., Tsuji, A., Ota, S., Ishikura, K., Nakamura, M., & Ito, M. (2014). Early and Long-Term Outcomes of Venous Stent Implantation for Iliac Venous Stenosis After Catheter-Directed Thrombolysis for Acute Deep Vein Thrombosis. *Circulation Journal*, *78*(5), 1234–1239. https://doi.org/10.1253/circj.cj-13-1247

Mitchell, P., Lee, S. C. M., Yoo, P. E., Morokoff, A., Sharma, R. P., Williams, D. L., MacIsaac, C., Howard, M. E., Irving, L., Vrljic, I., Williams, C., Bush, S., Balabanski, A. H., Drummond, K. J., Desmond, P., Weber, D., Denison, T., Mathers, S., O'Brien, T. J., … Campbell, B. C. V. (2023). Assessment of Safety of a Fully Implanted Endovascular Brain-Computer Interface for Severe Paralysis in 4 Patients: The Stentrode With Thought-Controlled Digital Switch (SWITCH) Study. *JAMA Neurology*, *80*(3), 270–278. PubMed. https://doi.org/10.1001/jamaneurol.2022.4847

Mohammadzadeh, P., & Nazarbaghi, S. (2022). The prevalence of drug-resistant epilepsy and its associated factors in patients with epilepsy. *Clinical Neurology and Neurosurgery, 213*, 107086. https://doi.org/10.1016/j.clineuro.2021.107086

Moon, J. Y., Suh, D. C., Lee, Y. S., Kim, Y. W., & Lee, J. S. (2014). Considerations of blood properties, outlet boundary conditions and energy loss approaches in computational fluid dynamics modeling. *Neurointervention*, *9*(1), 1–8. PubMed. https://doi.org/10.5469/neuroint.2014.9.1.1

Morris, P. D., Narracott, A., von Tengg-Kobligk, H., Silva Soto, D. A., Hsiao, S., Lungu, A., Evans, P., Bressloff, N. W., Lawford, P. V., Hose, D. R., & Gunn, J. P. (2016). Computational fluid dynamics modelling in cardiovascular medicine. *Heart (British Cardiac Society)*, *102*(1), 18–28. PubMed. https://doi.org/10.1136/heartjnl-2015-308044

Morris, P. P., Black, D. F., Port, J., & Campeau, N. (2017). Transverse Sinus Stenosis Is the Most Sensitive MR Imaging Correlate of Idiopathic Intracranial Hypertension. *AJNR. American Journal of Neuroradiology*, *38*(3), 471–477. PubMed. https://doi.org/10.3174/ajnr.A5055

Murphy, J., & Boyle, F. (2010). Predicting neointimal hyperplasia in stented arteries using time-dependant computational fluid dynamics: A review. *Computers in Biology and Medicine*, *40*(4), 408–418. https://doi.org/10.1016/j.compbiomed.2010.02.005

NER 2019 Sponsors. (2019, March). 2019 9th International IEEE/EMBS Conference on Neural Engineering (NER). https://doi.org/10.1109/ner.2019.8717103

Neudorfer, C., Bhatia, K., Boutet, A., Germann, J., Elias, G. JB., Loh, A., Paff, M., Krings, T., & Lozano, A. M. (2020). Endovascular deep brain stimulation: Investigating the relationship between vascular structures and deep brain stimulation targets. *Brain Stimulation*, *13*(6), 1668–1677. https://doi.org/10.1016/j.brs.2020.09.016

Ng, J., Bourantas, C. V., Torii, R., Ang, H. Y., Tenekecioglu, E., Serruys, P. W., & Foin, N. (2017). Local Hemodynamic Forces After Stenting. *Arteriosclerosis, Thrombosis, and Vascular Biology*, *37*(12), 2231–2242. https://doi.org/10.1161/atvbaha.117.309728

Ochieng, A., Onyango, & Kiriamiti, K. (2010). Experimental measurement and computational fluid dynamics simulation of mixing in a stirred tank: A review. *South African Journal of Science*, *105*(11/12). https://doi.org/10.4102/sajs.v105i11/12.139

Opie, N. L., John, S. E., Rind, G. S., Ronayne, S. M., Wong, Y. T., Gerboni, G., Yoo, P. E., Lovell, T. J. H., Scordas, T. C. M., Wilson, S. L., Dornom, A., Vale, T., O'Brien, T. J., Grayden, D. B., May, C. N., & Oxley, T. J. (2018). Focal stimulation of the sheep motor cortex with a chronically implanted minimally invasive electrode array mounted on an endovascular stent. *Nature Biomedical Engineering*, *2*(12), 907–914. https://doi.org/10.1038/s41551-018-0321-z

Opie, N. L., van der Nagel, N. R., John, S. E., Vessey, K., Rind, G. S., Ronayne, S. M., Fletcher, E. L., May, C. N., O'Brien, T. J., & Oxley, T. J. (2017). Micro-CT and Histological Evaluation of an Neural Interface Implanted Within a Blood Vessel. *IEEE Transactions on Biomedical Engineering*, *64*(4), 928–934. https://doi.org/10.1109/tbme.2016.2552226

Oxley, T. J., Opie, N. L., John, S. E., Rind, G. S., Ronayne, S. M., Burkitt, A. N., Grayden, D. B., May, C. N., & O'Brien, T. J. (2017). A Minimally Invasive Endovascular Stent-Electrode Array for Chronic Recordings of Cortical Neural Activity. *SpringerBriefs in Electrical and Computer Engineering*, 55–63. https://doi.org/10.1007/978-3-319-64373-1_6

Oxley, T. J., Opie, N. L., John, S. E., Rind, G. S., Ronayne, S. M., Wheeler, T. L., Judy, J. W., McDonald, A. J., Dornom, A., Lovell, T. J. H., Steward, C., Garrett, D. J., Moffat, B. A., Lui, E. H., Yassi, N., Campbell, B. C. V., Wong, Y. T., Fox, K. E., Nurse, E. S., … O'Brien, T. J. (2016). Minimally invasive endovascular stent-electrode array for high-fidelity, chronic recordings of cortical neural activity. *Nature Biotechnology*, *34*(3), 320–327. https://doi.org/10.1038/nbt.3428

Oxley, T. J., Opie, N. L., Rind, G. S., Liyanage, K., John, S. E., Ronayne, S., McDonald, A. J., Dornom, A., Lovell, T. J. H., Mitchell, P. J., Bennett, I., Bauquier, S., Warne, L. N., Steward, C., Grayden, D. B., Desmond, P., Davis, S. M., O'Brien, T. J., & May, C. N. (2018). An ovine model of cerebral catheter venography for implantation of an endovascular neural interface. *Journal of Neurosurgery*, *128*(4), 1020–1027. https://doi.org/10.3171/2016.11.jns161754

Oxley, T. J., Yoo, P. E., Rind, G. S., Ronayne, S. M., Lee, C. M. S., Bird, C., Hampshire, V., Sharma, R. P., Morokoff, A., Williams, D. L., MacIsaac, C., Howard, M. E., Irving, L., Vrljic, I., Williams, C., John, S. E., Weissenborn, F., Dazenko, M., Balabanski, A. H., … Opie, N. L. (2021). Motor neuroprosthesis implanted with neurointerventional surgery improves capacity for activities of daily living tasks in severe paralysis: First in-human experience. *Journal of Neurointerventional Surgery*, *13*(2), 102–108. PubMed. https://doi.org/10.1136/neurintsurg-2020-016862

Passerini, A. G., Milsted, A., & Rittgers, S. E. (2003). Shear stress magnitude and directionality modulate growth factor gene expression in preconditioned vascular endothelial cells. *Journal of Vascular Surgery*, *37*(1), 182–190. https://doi.org/10.1067/mva.2003.66

Peng, L., Qiu, Y., Huang, Z., Xia, C., Dai, C., Zheng, T., & Li, Z. (2017). Numerical Simulation of Hemodynamic Changes in Central Veins after Tunneled Cuffed Central Venous Catheter Placement in Patients under Hemodialysis. *Scientific Reports*, *7*(1), 15955–15955. PubMed. https://doi.org/10.1038/s41598-017-12456-7

Penn, R. D., Hilal, S. K., Michelsen, W. J., Goldensohn, E. S., & Driller, J. (1973). Intravascular intracranial EEG recording. *Journal of Neurosurgery*, *38*(2), 239–243. https://doi.org/10.3171/jns.1973.38.2.0239

Pereira, V. M., Cancelliere, N. M., Najafi, M., MacDonald, D., Natarajan, T., Radovanovic, I., Krings, T., Rutka, J., Nicholson, P., & Steinman, D. A. (2021). Torrents of torment: Turbulence as a mechanism of pulsatile tinnitus secondary to venous stenosis revealed by high-fidelity computational fluid dynamics. *Journal of Neurointerventional Surgery*, *13*(8), 732–737. PubMed. https://doi.org/10.1136/neurintsurg-2020-016636

Phelps, J. E., & DePaola, N. (2000). Spatial variations in endothelial barrier function in disturbed flows in vitro. *American Journal of Physiology-Heart and Circulatory Physiology*, *278*(2), H469–H476. https://doi.org/10.1152/ajpheart.2000.278.2.h469

Prochazka, A., Mushahwar, V. K., & McCreery, D. B. (2001). Neural prostheses. *The Journal of Physiology*, *533*(Pt 1), 99–109. PubMed. https://doi.org/10.1111/j.1469-7793.2001.0099b.x

Puffer, R. C., Mustafa, W., & Lanzino, G. (2012). Venous sinus stenting for idiopathic intracranial hypertension: A review of the literature: Table 1. *Journal of NeuroInterventional Surgery*, *5*(5), 483–486. https://doi.org/10.1136/neurintsurg-2012-010468

Qi, W., Ooi, A., Grayden, D. B., & John, S. E. (2023, July 24). *Computational Fluid Dynamics of Stent-Mounted Neural Interfaces in an Idealized Cerebral Venous Sinus **. 2023 45th Annual International Conference of the IEEE Engineering in Medicine & Biology Society (EMBC). https://doi.org/10.1109/embc40787.2023.10341099

Rajah, G., Saber, H., Singh, R., & Rangel-Castilla, L. (2018). Endovascular delivery of leads and stentrodes and their applications to deep brain stimulation and neuromodulation: A review. *Neurosurgical Focus*, *45*(2), E19. https://doi.org/10.3171/2018.4.focus18130

Rajendran, P., Rengarajan, T., Thangavel, J., Nishigaki, Y., Sakthisekaran, D., Sethi, G., & Nishigaki, I. (2013). The vascular endothelium and human diseases. *International Journal of Biological Sciences*, *9*(10), 1057–1069. PubMed. https://doi.org/10.7150/ijbs.7502

Raper, D., Buell, T. J., Ding, D., Chen, C.-J., Starke, R. M., & Liu, K. C. (2017). Pattern of pressure gradient alterations after venous sinus stenting for idiopathic intracranial hypertension predicts stent-adjacent stenosis: A proposed classification system. *Journal of NeuroInterventional Surgery*, *10*(4), 391–395. https://doi.org/10.1136/neurintsurg-2017-013135

Raza, S. A., Opie, N. L., Morokoff, A., Sharma, R. P., Mitchell, P. J., & Oxley, T. J. (2020). Endovascular Neuromodulation: Safety Profile and Future Directions. *Frontiers in Neurology*, *11*, 351–351. PubMed. https://doi.org/10.3389/fneur.2020.00351

Reza, M. M. S., & Arzani, A. (2019). A critical comparison of different residence time measures in aneurysms. *Journal of Biomechanics*, *88*, 122–129. https://doi.org/10.1016/j.jbiomech.2019.03.028

Rivera-Rivera, L. A., Schubert, T., Turski, P., Johnson, K. M., Berman, S. E., Rowley, H. A., Carlsson, C. M., Johnson, S. C., & Wieben, O. (2017). Changes in intracranial venous blood flow and pulsatility in Alzheimer's disease: A 4D flow MRI study. *Journal of Cerebral Blood Flow and Metabolism : Official Journal of the International Society of Cerebral Blood Flow and Metabolism*, *37*(6), 2149–2158. PubMed. https://doi.org/10.1177/0271678X16661340

Roux, E., Bougaran, P., Dufourcq, P., & Couffinhal, T. (2020). Fluid Shear Stress Sensing by the Endothelial Layer. *Frontiers in Physiology*, *11*, 861–861. PubMed. https://doi.org/10.3389/fphys.2020.00861

Saber, H., Lewis, W., Sadeghi, M., Rajah, G., & Narayanan, S. (2018). Stent Survival and Stent-Adjacent Stenosis Rates following Venous Sinus Stenting for Idiopathic Intracranial Hypertension: A Systematic Review and Meta-Analysis. *Interventional Neurology*, *7*(6), 490–500. PubMed. https://doi.org/10.1159/000490578

Saleem, T., & Raju, S. (2022). An overview of in-stent restenosis in iliofemoral venous stents. *Journal of Vascular Surgery: Venous and Lymphatic Disorders*, *10*(2), 492-503.e2. https://doi.org/10.1016/j.jvsv.2021.10.011

Saleem, T., & Raju, S. (2023). Iliac vein stenting in chronic venous leg ulcers. *Venous Ulcers*, 433–471. https://doi.org/10.1016/b978-0-323-90610-4.00011-2

Schmidt, R. F., Wu, C., Lang, M. J., Soni, P., Williams, K. A., Boorman, D. W., Evans, J. J., Sperling, M. R., & Sharan, A. D. (2016). Complications of subdural and depth electrodes in 269 patients undergoing 317 procedures for invasive monitoring in epilepsy. *Epilepsia*, *57*(10), 1697–1708. https://doi.org/10.1111/epi.13503

Sharifi, M., & Mehdipour, M. (2010). Percutaneous therapy of acute on chronic lower extremity venous occlusive disease. *Catheterization and Cardiovascular Interventions*, *75*(5), 685–689. https://doi.org/10.1002/ccd.22377

Shen, X., Jiang, J., Zhu, H., Lu, K., Dong, P., & Gu, L. (2020). Comparative study of tapered versus conventional cylindrical balloon for stent implantation in stenotic tapered artery. *Artificial Organs*, *44*(7), 727–735. PubMed. https://doi.org/10.1111/aor.13661

Shibeshi, S. S., & Collins, W. E. (2005). The Rheology of Blood Flow in a Branched Arterial System. *Applied Rheology*, *15*(6), 398–405. https://doi.org/10.1515/arh-2005-0020

Shields, L. B. E., Shields, C. B., Yao, T. L., Plato, B. M., Zhang, Y. P., & Dashti, S. R. (2019). Endovascular Treatment for Venous Sinus Stenosis in Idiopathic Intracranial Hypertension: An Observational Study of Clinical Indications, Surgical Technique, and Long-Term Outcomes. *World Neurosurgery*, *121*, e165–e171. https://doi.org/10.1016/j.wneu.2018.09.070

Shih, J. J., Krusienski, D. J., & Wolpaw, J. R. (2012). Brain-computer interfaces in medicine. *Mayo Clinic Proceedings*, *87*(3), 268–279. PubMed. https://doi.org/10.1016/j.mayocp.2011.12.008

Shlofmitz, E., Iantorno, M., & Waksman, R. (2019). Restenosis of Drug-Eluting Stents. *Circulation: Cardiovascular Interventions*, *12*(8). https://doi.org/10.1161/circinterventions.118.007023

Sindeev, S., Arnold, P. G., Frolov, S., Prothmann, S., Liepsch, D., Balasso, A., Berg, P., Kaczmarz, S., & Kirschke, J. S. (2018). Phase-contrast MRI versus numerical simulation to quantify

hemodynamical changes in cerebral aneurysms after flow diverter treatment. *PloS One*, *13*(1), e0190696–e0190696. PubMed. https://doi.org/10.1371/journal.pone.0190696

Soulis, J. V., Lampri, O. P., Fytanidis, D. K., & Giannoglou, G. D. (2011, October). *Relative residence time and oscillatory shear index of non-Newtonian flow models in aorta*. 2011 10th International Workshop on Biomedical Engineering. https://doi.org/10.1109/iwbe.2011.6079011

Stent Thrombosis. (2020). In *Definitions*. Qeios. https://doi.org/10.32388/v29tay

Strijkers, R. H. W., de Wolf, M. A. F., Arnoldussen, C. W. K. P., Timbergen, M. J. M., de Graaf, R., Ten Cate-Hoek, A. J., & Wittens, C. H. A. (2015). Venous In-stent Thrombosis Treated by Ultrasound Accelerated Catheter Directed Thrombolysis. *European Journal of Vascular and Endovascular Surgery*, *49*(4), 440–447. https://doi.org/10.1016/j.ejvs.2015.01.006

Tabakova, S., Nikolova, E., & Radev, St. (2014). *Carreau model for oscillatory blood flow in a tube*. AIP Conference Proceedings. https://doi.org/10.1063/1.4902290

Tahir, H., Bona-Casas, C., & Hoekstra, A. G. (2013). Modelling the effect of a functional endothelium on the development of in-stent restenosis. *PloS One*, *8*(6), e66138–e66138. PubMed. https://doi.org/10.1371/journal.pone.0066138

Tai, Y.-D., Widdicombe, B., Unnithan, R. R., Grayden, D. B., & John, S. E. (2023, July 24). *Wearable Transmitter Coil Design for Inductive Wireless Power Transfer to Implantable Devices*. 2023 45th Annual International Conference of the IEEE Engineering in Medicine & Biology Society (EMBC). https://doi.org/10.1109/embc40787.2023.10340600

Tardy, Y., Resnick, N., Nagel, T., Gimbrone, M. A., & Dewey, C. F. (1997). Shear Stress Gradients Remodel Endothelial Monolayers in Vitro via a Cell Proliferation-Migration-Loss Cycle. *Arteriosclerosis, Thrombosis, and Vascular Biology*, *17*(11), 3102–3106. https://doi.org/10.1161/01.atv.17.11.3102

Tomaszewski, M., Sybilski, K., Baranowski, P., & Małachowski, J. (2020). Experimental and numerical flow analysis through arteries with stent using particle image velocimetry and computational fluid dynamics method. *Biocybernetics and Biomedical Engineering*, *40*(2), 740–751. https://doi.org/10.1016/j.bbe.2020.02.010

Upton, R., Grant, C., & Ludbrook, G. (1994). An Ultrasonic Doppler Venous Outflow Method for the Continuous Measurement of Cerebral Blood Flow in Conscious Sheep. *Journal of Cerebral Blood Flow & Metabolism*, *14*(4), 680–688. https://doi.org/10.1038/jcbfm.1994.85

van Ooij, P., Guédon, A., Poelma, C., Schneiders, J., Rutten, M. C. M., Marquering, H. A., Majoie, C. B., vanBavel, E., & Nederveen, A. J. (2011). Complex flow patterns in a real-size intracranial aneurysm phantom: Phase contrast MRI compared with particle image velocimetry and computational fluid dynamics. *NMR in Biomedicine*, *25*(1), 14–26. https://doi.org/10.1002/nbm.1706

Wall, M. (2010). Idiopathic intracranial hypertension. *Neurologic Clinics*, *28*(3), 593–617. PubMed. https://doi.org/10.1016/j.ncl.2010.03.003

Wang, J., Jin, X., Huang, Y., Ran, X., Luo, D., Yang, D., Jia, D., Zhang, K., Tong, J., Deng, X., & Wang, G. (2018). Endovascular stent-induced alterations in host artery mechanical environments and their roles in stent restenosis and late thrombosis. *Regenerative Biomaterials*, *5*(3), 177–187. PubMed. https://doi.org/10.1093/rb/rby006

Watts, T. E., Chatterjee, A., & Leesar, M. A. (2018). Stent Thrombosis. *Cardiovascular Thrombus*, 217–224. https://doi.org/10.1016/b978-0-12-812615-8.00015-6

Williamson, P. N., Docherty, P. D., Yazdi, S. G., Khanafer, A., Kabaliuk, N., Jermy, M., & Geoghegan, P. H. (2021). Review of the Development of Hemodynamic Modeling Techniques to Capture Flow Behavior in Arteries Affected by Aneurysm, Atherosclerosis, and Stenting. *Journal of Biomechanical Engineering*, *144*(4). https://doi.org/10.1115/1.4053082

Wodlinger, B., Degenhart, A. D., Collinger, J. L., Tyler-Kabara, E. C., & Wei Wang. (2011, August). *The impact of electrode characteristics on electrocorticography (ECoG)*. 2011 Annual International Conference of the IEEE Engineering in Medicine and Biology Society. https://doi.org/10.1109/iembs.2011.6090842

Wong, C. H., Birkett, J., Byth, K., Dexter, M., Somerville, E., Gill, D., Chaseling, R., Fearnside, M., & Bleasel, A. (2009). Risk factors for complications during intracranial electrode recording in presurgical evaluation of drug resistant partial epilepsy. *Acta Neurochirurgica*, *151*(1), 37–50. https://doi.org/10.1007/s00701-008-0171-7

Xu, K., Yu, T., Yuan, Y., & Yu, J. (2015). Current Status of the Application of Intracranial Venous Sinus Stenting. *International Journal of Medical Sciences*, *12*(10), 780–789. PubMed. https://doi.org/10.7150/ijms.12604

Yamaguchi, M., Sugimoto, K., Zamora, C. A., Takahashi, T., Hayashi, Y., & Sugimura, K. (2006). Placement of Self-expanding Stents with Different Diameters in the Porcine Venous System: An Experimental Study. *Journal of Vascular and Interventional Radiology*, *17*(1), 113–119. https://doi.org/10.1097/01.rvi.0000186951.22050.3d

Yang, W., Gong, Y., & Li, W. (2021). A Review: Electrode and Packaging Materials for Neurophysiology Recording Implants. *Frontiers in Bioengineering and Biotechnology*, *8*, 622923–622923. PubMed. https://doi.org/10.3389/fbioe.2020.622923

Ying, W., Feng, H., Li, X., Wang, X., Cao, P., & Wang, Y. (2020). Effect of Iliac Vein Stent with Crown on Flow Field of Bifurcation. *International Journal of Fluid Machinery and Systems*, *13*(2), 517–525. https://doi.org/10.5293/ijfms.2020.13.2.517

Zarins, C. K., Giddens, D. P., Bharadvaj, B. K., Sottiurai, V. S., Mabon, R. F., & Glagov, S. (1983). Carotid bifurcation atherosclerosis. Quantitative correlation of plaque localization with flow velocity profiles and wall shear stress. *Circulation Research*, *53*(4), 502–514. https://doi.org/10.1161/01.res.53.4.502

Zhang, C., Pan, C., Chan, K. F., Gao, J., Yang, Z., Leung, K. K. C., Jin, D., Wang, Y., Xia, N., Ning, Z., Wang, X., Jiang, S., Zhang, Z., Wang, Q., Hao, B., Chiu, P. W. Y., & Zhang, L. (2023). Wirelessly powered deformable electronic stent for noninvasive electrical stimulation of lower esophageal sphincter. *Science Advances*, *9*(10), eade8622–eade8622. PubMed. https://doi.org/10.1126/sciadv.ade8622

Zhang, X., Li, L., & Deng, Z. (2023). Liquid Metal-Based Flexible Bioelectrodes for Management of In-Stent-Restenosis: Potential Application. *Biosensors*, *13*(8), 795. PubMed. https://doi.org/10.3390/bios13080795

Zhao, H. Q., Nikanorov, A., Virmani, R., Jones, R., Pacheco, E., & Schwartz, L. B. (2009). Late Stent Expansion and Neointimal Proliferation of Oversized Nitinol Stents in Peripheral Arteries. *CardioVascular and Interventional Radiology*, *32*(4), 720–726. https://doi.org/10.1007/s00270-009-9601-z

Zun, P. S., Narracott, A. J., Chiastra, C., Gunn, J., & Hoekstra, A. G. (2019). Location-Specific Comparison Between a 3D In-Stent Restenosis Model and Micro-CT and Histology Data from Porcine In Vivo Experiments. *Cardiovascular Engineering and Technology*, *10*(4), 568–582. PubMed. https://doi.org/10.1007/s13239-019-00431-4

Appendices

Supplementary materials

Chapter 3 Appendix

Coefficient of Fourier series used in the inlet waveform Equation (10) for **Boundary Conditions** in *Physical Models*

Coefficients (with 95% confidence bounds):

a0 =	245.4	(244.2, 246.6)
a1 =	-37.85	(-40.32, -35.38)
b1 =	3.251	(-3.304, 9.805)
a2 =	16.39	(15.07, 17.71)
b2 =	-3.724	(-9.294, 1.845)
a3 =	1.665	(0.41, 2.92)
b3 =	3.248	(2.304, 4.192)
w =	6.085	(5.74, 6.43)

Tabulated data for **Numeric Errors** in ***Verification***

Table S1. Fluxes report for single and double precision

Precision	Inlet (kg/s)	Outlet (kg/s)	Net result (kg/s)
Single	0.001991202589124441	-0.001991210505366325	-8e-9
Double	0.001991217347721465	-0.001991221371953932	-4e-9

Tabulated data for **Mesh dependence study** in ***Verification***

Table S2. Quality report for the constructed mesh

Quality measure	Project Model	Recommendation
Minimum Orthogonal quality	0.15	>0.1
Maximum surface Skewness	0.84	<0.7
Maximum Aspect Ratio	13.6	<50
Expansion Ratio	1.5	~1

Chapter 4 Appendix

Table S3. Pearson's correlation coefficient of tissue thickness and hemodynamic variables

Variable name	Pearson's correlation coefficient
CM*-WSS	-0.6326
CM-WSSG	0.7730

*CM stands for circumferential mean

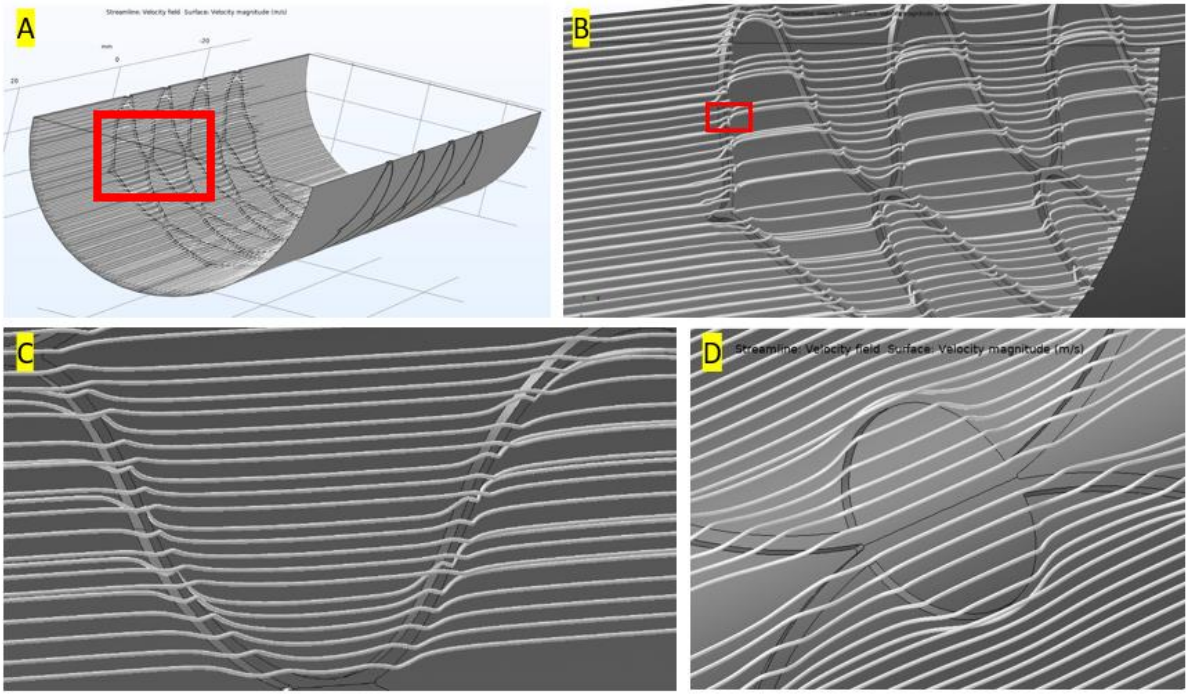

Figure S1. Surface streamlines near the blood vessel wall implanted with a 50 μm thick stent strut. A: The blood vessel wall is sliced in half to better visualize the streamlines near the vessel wall and stent. B: A zoomed-in view of the red frame in panel A, highlighting the disruption of blood flow direction by the stent struts. C: A further zoom-in on the blood flow streamlines near the stent strut, revealing a helical flow structure. D: Streamlines near the stent strut and an electrode with a diameter of 1 mm.

Chapter 6 Appendix

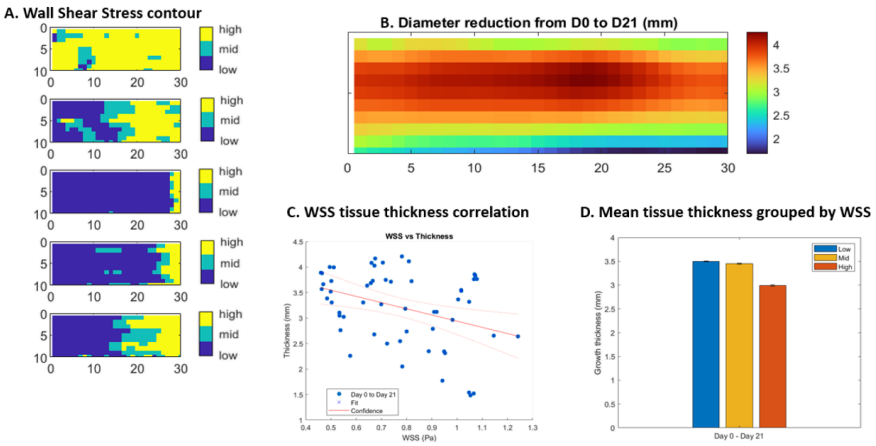

FIGURE S2. Wall Shear Stress and tissue growth thickness in Sheep No. 1. A: WSS contour map, with regions divided into low, mid, and high WSS regions. B: diameter reduction along the stented region, showing more tissue growth at the inlet. C: correlation between WSS and tissue thickness ($R = -0.37$; $P < 0.05$). D: mean tissue growth contributed by the low, mid, and high WSS regions. Arrows indicates blood flow direction.

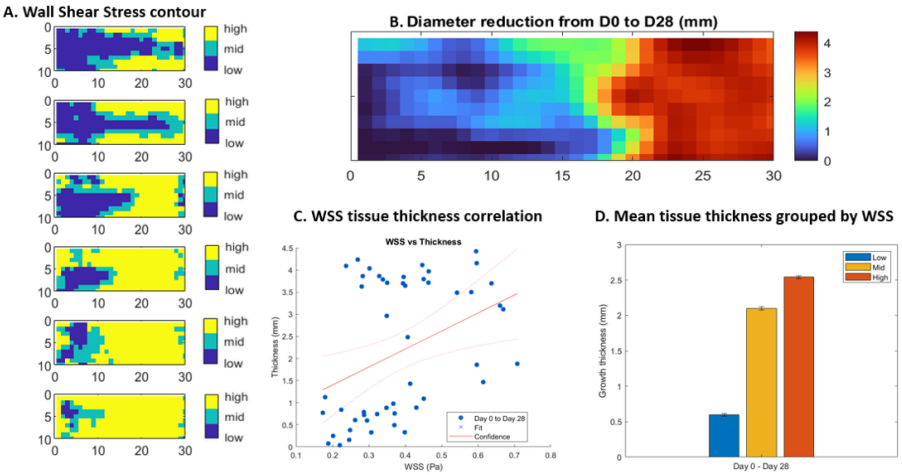

FIGURE S3. Wall Shear Stress and tissue growth thickness in Sheep No. 2. A: WSS contour map, with regions divided into low, mid, and high WSS regions. B: diameter reduction along the stented region, showing more tissue growth at the inlet. C: correlation between WSS and tissue thickness ($R = 0.37$; $P < 0.05$). D: mean tissue growth contributed by the low, mid, and high WSS regions. Arrows indicates blood flow direction.

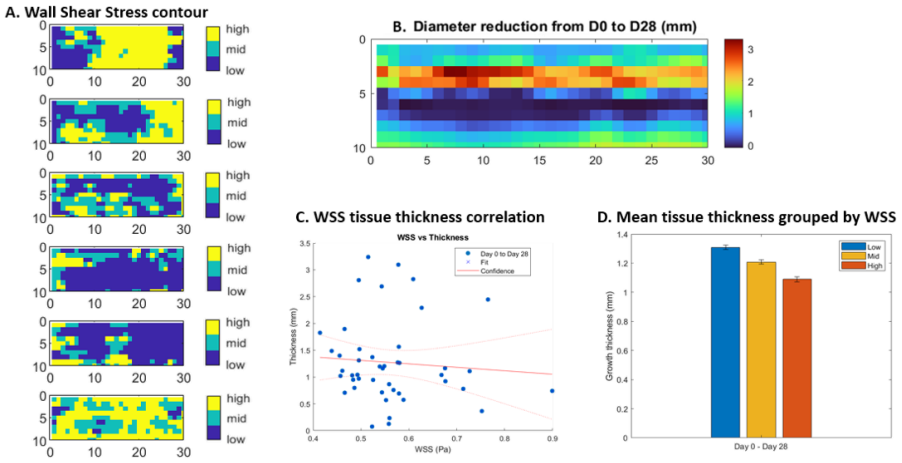

FIGURE S4. Wall Shear Stress and tissue growth thickness in Sheep No. 3. A: WSS contour map, with regions divided into low, mid, and high WSS regions. B: diameter reduction along the stented region, showing more tissue growth at the inlet. C: correlation between WSS and tissue thickness ($R = -0.083$; $P = 0.59$). D: mean tissue growth contributed by the low, mid, and high WSS regions. Arrows indicates blood flow direction.

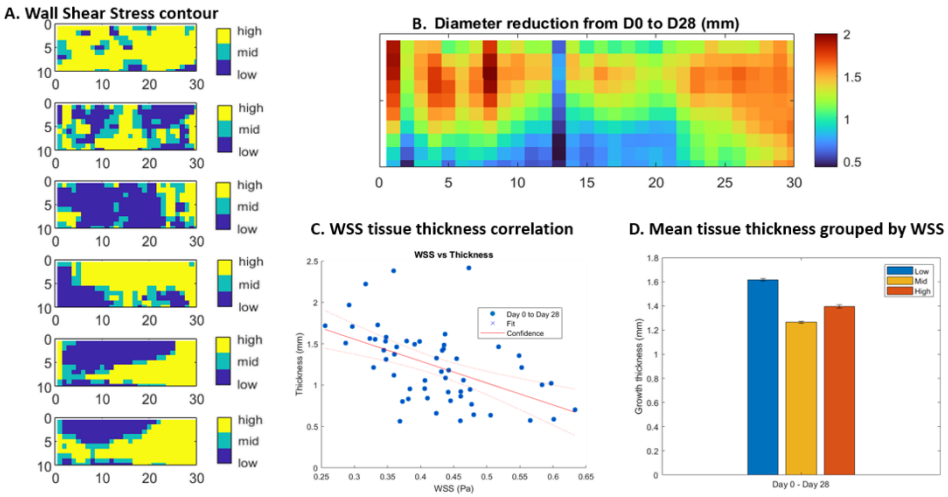

FIGURE S5. Wall Shear Stress and tissue growth thickness in Sheep No. 4. A: WSS contour map, with regions divided into low, mid, and high WSS regions. B: diameter reduction along the stented region, showing more tissue growth at the inlet. C: correlation between WSS and tissue thickness (R = -0.51; P < 0.05). D: mean tissue growth contributed by the low, mid, and high WSS regions. Arrows indicates blood flow direction.

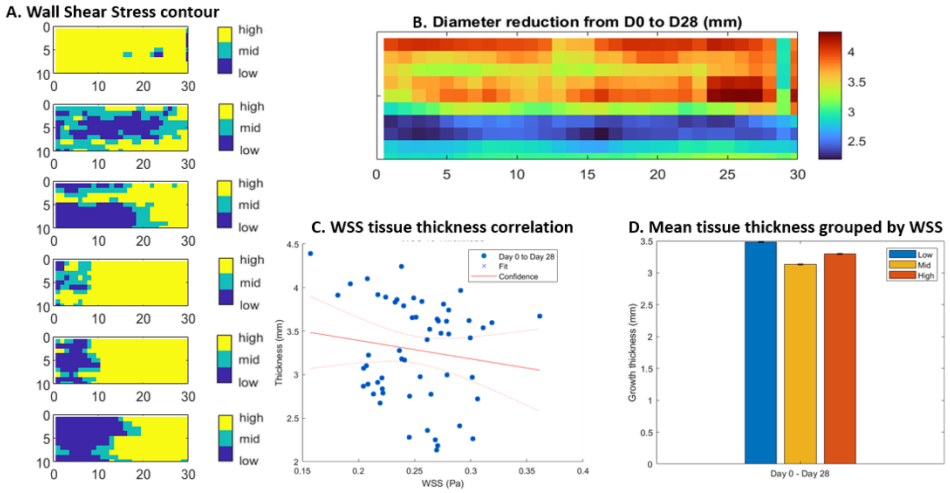

FIGURE S6. Wall Shear Stress and tissue growth thickness in Sheep No. 5. A: WSS contour map, with regions divided into low, mid, and high WSS regions. B: diameter reduction along the stented region, showing more tissue growth at the inlet. C: correlation between WSS and tissue thickness (R = -0.14; P = 0.30). D: mean tissue growth contributed by the low, mid, and high WSS regions. Arrows indicates blood flow direction.

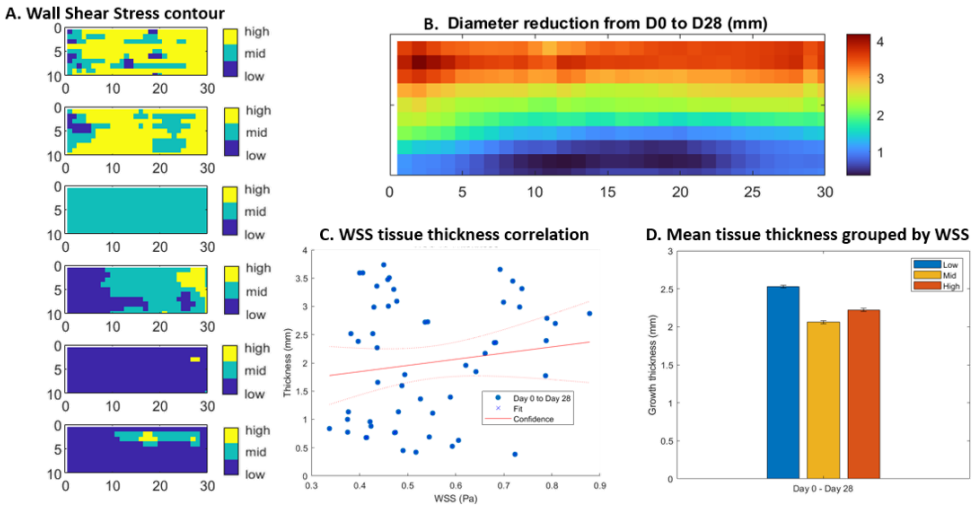

FIGURE S7. Wall Shear Stress and tissue growth thickness in Sheep No. 6. A: WSS contour map, with regions divided into low, mid, and high WSS regions. B: diameter reduction along the stented region, showing more tissue growth at the inlet. C: correlation between WSS and tissue thickness (R = 0.15; P = 0.28). D: mean tissue growth contributed by the low, mid, and high WSS regions. Arrows indicates blood flow direction.

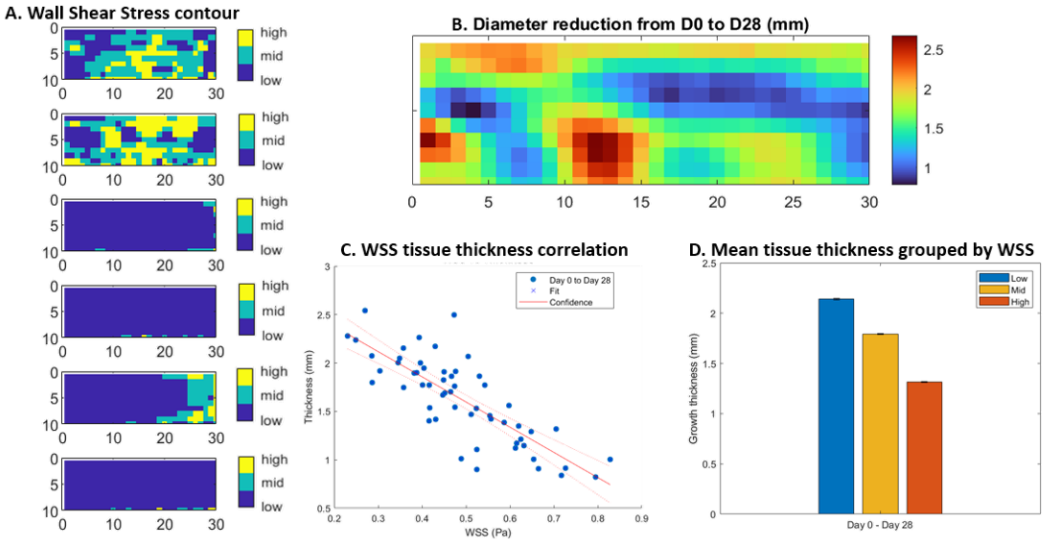

FIGURE S8. Wall Shear Stress and tissue growth thickness in Sheep No. 7. A: WSS contour map, with regions divided into low, mid, and high WSS regions. B: diameter reduction along the stented region, showing more tissue growth at the inlet. C: correlation between WSS and tissue thickness (R = -0.81; P < 0.05). D: mean tissue growth contributed by the low, mid, and high WSS regions. Arrows indicates blood flow direction.

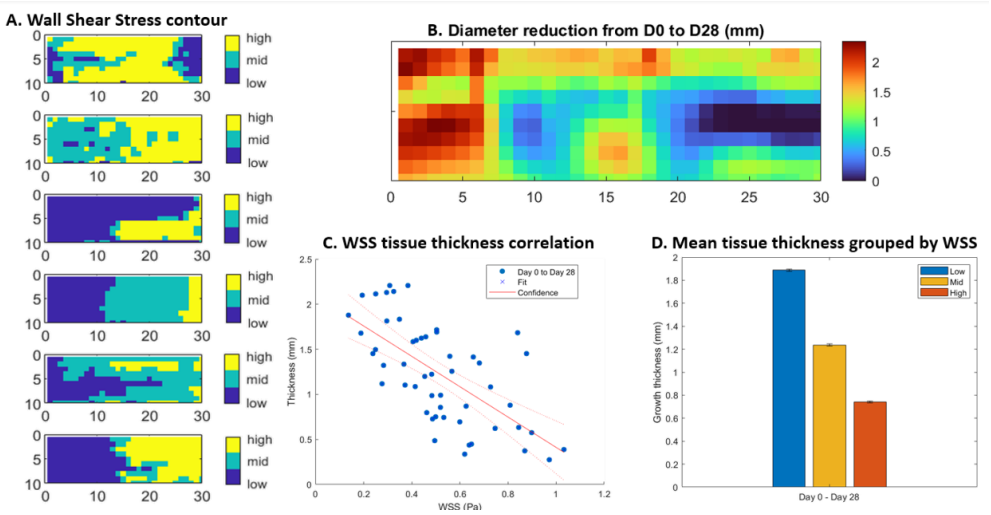

FIGURE S9. Wall Shear Stress and tissue growth thickness in Sheep No. 8. A: WSS contour map, with regions divided into low, mid, and high WSS regions. B: diameter reduction along the stented region, showing more tissue growth at the inlet. C: correlation between WSS and tissue thickness ($R = -0.65$; $P < 0.05$). D: mean tissue growth contributed by the low, mid, and high WSS regions. Arrows indicates blood flow direction.